UNIVERSITY OF OKLAHOMA

GRADUATE COLLEGE

SYNTHESIS AND CHARACTERIZATIONS OF LIGHTWEIGHT, HIGHLY FLEXIBLE POROUS POLYDIMETHYLSILOXANE (PDMS) STRUCTURES WITH PIEZORESISTIVE STRAIN SENSING CAPABILITIES USING SOLVENT EVAPORATION TECHNIQUE

A DISSERTATION

SUBMITTED TO THE GRADUATE FACULTY

in partial fulfillment of the requirements for the

Degree of

DOCTOR OF PHILOSOPHY

By

MOHAMMAD ABSHIRINI
Norman, Oklahoma
2022

SYNTHESIS AND CHARACTERIZATIONS OF LIGHTWEIGHT, HIGHLY FLEXIBLE POROUS POLYDIMETHYLSILOXANE (PDMS) STRUCTURES WITH PIEZORESISTIVE STRAIN SENSING CAPABILITIES USING SOLVENT EVAPORATION TECHNIQUE

A DISSERTATION APPROVED FOR THE
SCHOOL OF AEROSPACE AND MECHANICAL ENGINEERING

BY THE COMMITTEE CONSISTING OF

Dr. Mrinal C. Saha, Chair

Dr. M. Cengiz Altan, Co-Chair

Dr. Yingtao Liu

Dr. Chung-Hao Lee

Dr. Binbin Weng

Dedication

I dedicate this dissertation to my family, my beloved wife Parisa, my mother Maryam, my father Hassan, and my sisters Elham and Elaheh, my mother-in-law Simin, my father-in-law Mohammadreza, and my sister-in-law Ladan.

Acknowledgements

First, I would like to give my gratitude to Dr. Mrinal C. Saha for providing this opportunity for me to work in his research group at the University of Oklahoma. The support and guidance that I have received from him helped me toward a successful Ph.D. completion. I would also like to thank my co-advisor, Dr. M. Cengiz Altan, for his expert knowledge and valuable feedback. I also would like to give my gratitude to Dr. Yingtao Liu for his collaboration in my research In addition. I would like to thank my graduate committee members.

This accomplishment would not have been possible without the cooperation and help of my lab mates. I would also like to express my thanks and appreciation to Anirban Mondal, Emmanuel Hakizimana, Iain Kennedy, and Dr. Kuntal Maity. I also thank my former lab mates Mohammad Charara, Wenyuan Luo, and Musa Sukati for their collaboration. I would like to give my special thanks to Dr. Preston Larson, who helped me take the SEM images and Dr. Michael Detamore for allowing me to use the rheometer in his lab. I would also like to thank all the current and former AME staff and professors for making such a great environment for research and collaboration.

I am grateful for the financial support that was kindly provided by Dr. Mrinal Saha's research assistantship, AME department teaching assistantship, Dolese Teaching fellowship, Gallogly College of Engineering fellowship, Farzaneh Family

scholarships, Jim and Bee Close scholarship, Frank Chuck Mechanical Engineering scholarship, Gallogly College of Engineering Dissertation Excellence Award, and Graduate OU Alumni fellowship.

Also, I would like to thank my mother, Maryam, father Hassan, sisters Elham and Elaheh, mother-in-law Simin, father-in-law Mohammadreza, and sister-in-law Ladan for all the unconditional love and support they have given me. Above all, I would like to express my deepest gratitude to my beloved wife and my best friend, Parisa, who has stood by me through all my difficulties and my absences. She gave me true love and constant support, discussed ideas, and prevented several wrong turns. I have been so lucky to have her accompany me through this journey.

Table of Contents

Acknowledgements v

Table of Contents vii

Abstract xiii

List of Publications xv

List of Figures xvii

List of Tables xxvi

Chapter 1: Introduction 1

1.1. Conductive Polymer Nanocomposites 1

1.2. Piezoresistive Strain Sensor 2

1.2.1. Application of CPNC in Piezoresistive Strain Sensing 3

1.3. Porous Polymers 4

1.4. Different Porous Polymer Fabrication Methods 5

1.4.1. Direct Templating Technique 6

1.4.2. Emulsion Templating Technique 7

1.4.3. Phase Separation Technique 10

1.5. Porous CPNC for Sensing Applications 12

1.6. Additive Manufacturing of CPNC 13

1.7. Scope of Work 14

1.8. Objective 16

Chapter 2: Ternary Polymer Solution and Ternary Phase Diagram 17

2.1. Introduction 17

2.2. Ternary Phase Diagram 18

2.2.1. Binodal Curve 20

2.2.2. Spinodal Curve 21

2.2.3. Interaction Parameters 22

2.3. Phase Diagram Results 23

2.4. Chapter Conclusion 26

Chapter 3: Fabrication of Porous PDMS Structures with Tunable Properties Induced by Phase Separation Technique 27

3.1. Introduction 27

3.2. Experimental 29

3.1.1. Materials 29

3.1.2. Polymer Solution Preparation 29

3.1.2 Porous PDMS Plate Formation 31

3.2. Characterization 32

3.2.1. Pore Size Characterization 33

3.2.2. Mechanical Properties 33

3.2.3. Porosity Measurements 34

3.3. Results 35

3.3.1. Pore Size Distribution 36
3.3.2. Mechanical Behavior 41
3.3.3. Porosity Measurements 45
3.4. Chapter Conclusion 46
Chapter 4: Introducing Two-Step Phase Separation Method to Synthesis Hierarchical Porous PDMS Structure with Adjustable Properties 49
4.1. Introduction 49
4.2. Experimental Section 50
4.2.1. Materials 50
4.2.2. Polymer Solution Preparation 51
4.2.3. Fabrication of Porous PDMS Sheets 52
4.3. Characterization 53
4.3.1. Pore Size Analysis 53
4.3.2. Porosity 53
4.3.3. Mechanical Properties 53
4.4. Results and Discussions 54
4.4.1. Pore Morphology and Distribution 55
4.4.2. Porosity 61
4.4.3. Mechanical Properties 62
4.4.4. Rate Dependency Analysis 65

4.4.5. Hysteresis 66

4.7. Empirical Model 68

4.8. Chapter Conclusion 69

Chapter 5: Additive Manufacturing of Porous Conductive Polymer Nanocomposites Developed Using Phase Separation Technique 71

5.1. Introduction 71

5.2. Experimental Section 74

5.2.1. Materials 74

5.2.2. CPNC Solution Preparation 74

5.2.3. DIW of Porous CPNC 75

5.3. Characterization 77

5.3.1. Rheology Experiment 77

5.3.2. Microstructure and Porosity Characterization 78

5.3.3. Mechanical Properties 78

5.3.4. Conductivity and Piezoresistive Behavior 78

5.3.5. Sensing Applications 80

5.4. Results and Discussion 80

5.4.1. Rheological Properties 80

5.4.2. Microstructure and Porosity 82

5.4.3. Mechanical Properties 85

5.4.4. Electrical and Piezoresistive Properties 87

5.4.5. Sensing Application 94

5.5. Chapter Conclusion 97

Chapter 6: 3D Printed Highly Porous and Flexible Conductive Polymer Nanocomposites with Dual-Scale Porosity and Piezoresistive Sensing Functions 99

6.1. Introduction 99

6.2. Experimental Methods 101

6.2.1. Materials 101

6.2.2. Ink Preparation 102

6.2.3. DIW of Dual-Scale Porous Structure 102

6.3. Characterization 106

6.3.1. Rheology Analysis 106

6.3.2. Porosity and Pore Size Distribution 106

6.3.3. Mechanical Properties 107

6.3.4. Piezoresistive Response 107

6.4. Results and Discussion 108

6.4.1. Rheological Properties 108

6.4.2. Pore Morphology and Porosity 110

6.4.3. Mechanical Properties 117

6.4.5. Finite Element Analysis 122

6.4.5. Piezoresistive Response 127

6.5. Chapter Conclusion 133

Chapter 7: Conclusion and Future Work 135

7.1. Conclusion 135

7.2. Recommendations for Future Work 139

References 141

Abstract

Considering their specific structure, porous polymers have high adsorptive capacity, high flexibility, and high surface area compared to solid material. Highly flexible, deformable, and ultralightweight structures are required for advanced sensing applications such as wearable electronics and robotics. Hence, porous conductive polymer nanocomposites (CPNCs) have attracted significant attention for developing flexible piezoresistive sensors. In the first part of this dissertation, the application of solvent evaporation-induced phase separation (EIPS) as a promising technique to create porous polymer structures is investigated. The ternary polymer solution consisting of polymer/solvent/nonsolvent is explored. The ternary phase diagram is constructed, showing the thermodynamic equilibrium state for polymeric solutions consisting of Polydimethylsiloxane (PDMS)/Water/Tetrahydrofuran (THF). The possible composition path during the heat treatment and phase separation procedure is obtained. Moreover, the fabrication and characterization of porous PDMS structures developed by the EIPS technique are explored. The porous PDMS structures are formed by phase separation induced by removing the solvent, leading to water enriched droplets formation and removal during the stepping heat treatment procedure. The results show that the isolated pores with the adjustable pore size ranging from 330 μm to 1900 μm are obtained by tuning the water to the THF ratio. A wide range of elastic modulus ranging between 0.49-1.05 MPa was achieved without affecting the density of the porous sample by adjusting the solvent and non-solvent content in the solution.

The second part of the dissertation proposes a two-step phase separation synthesis protocol based on a ternary polymer solution. THF and Toluene with various mixing ratios are utilized as the solvent phase. Two distinct pore size distributions were observed in the cast PDMS sheets. The

large pores with an average of 509 μm are formed during the first step of the phase separation after THF is evaporated. The second phase separation occurs later at higher temperatures by the evaporation of Toluene, resulting in much smaller pores with an average size of 28 μm. The experiments reveal that raising the THF/solvent ratio increases the large pore concentration, and the small pore density is reduced. The elastic modulus is varied between 0.64-0.95 MPa, indicating that the proposed method can create porous structures with a wide range of flexibility while keeping the density constant.

In the third part of the dissertation, a novel approach to synthesizing highly flexible and ultralightweight piezoresistive sensors is developed by combining the direct ink writing (DIW) and EIPS method. CPNC is prepared by dispersing carbon nanotubes (CNTs) at various concentrations in PDMS polymer, followed by mixing with solvent and nonsolvent phases to achieve a homogenous solution. Macroscale pores are established by designing structural printing patterns with adjustable infill densities, while the microscale pores are developed by EIPS of the deposited CPNC solution ink. Silica nanoparticles are utilized to modify the rheological properties of the DIW, evaluated by rheology experiments. A tunable porosity of up to 84% is achieved by controlling macroscale (infill density) and microscale porosity (polymer weight). The effect of macroscale/microscale porosity and printing nozzle sizes on the mechanical and piezoresistive behavior of the CPNC structures is explored. The electrical and mechanical testing demonstrate a durable, extremely deformable, and sensitive piezoresistive response without sacrificing mechanical performance. The flexibility and sensitivity of the CPNC structure are enhanced up to 900% and 67% with the development of dual-scale porosity. The application of the developed porous piezoresistive sensor for detecting human motion is also evaluated.

List of Publications

Journal Papers

1) M. Abshirini, M. C. Saha, M. C. Altan, Y. Liu, "3D Printed Flexible Micro-Scaled Porous Conductive Polymer Nanocomposites for Piezoresistive Sensing Applications." *Advanced Materials Technologies* (In Press).
2) M. Abshirini, M. C. Saha, M. C. Altan, Y. Liu, "Synthesis and characterization of hierarchical porous structure of polydimethylsiloxane (PDMS) sheets via two-step phase separation method." *Materials & Design.* 2021;212(15):110194.
3) M. Abshirini, M. C. Saha, M. C. Altan, Y. Liu, L. Cummings, T. Robison, "Investigation of porous polydimethylsiloxane structures with tunable properties induced by the phase separation technique." *Journal of Applied Polymer Science*. 2021;138(29):50688.
4) M. Abshirini, M. C. Saha, L. Cummings, T. Robison, "Synthesis and characterization of porous polydimethylsiloxane structures with adjustable porosity and pore morphology using emulsion templating technique." *Polymer Engineering & Science.* 2021;61(7):1943-1955.
5) M. Abshirini, M. Charara, P. Marashizadeh, M. C. Saha, M. C. Altan, Y. Liu, "Functional nanocomposites for 3D printing of stretchable and wearable sensors", *Applied Nanoscience*. 2019;9(8):2071-2083.
6) M. Charara, M. Abshirini, M. C. Saha, M. C. Altan, Y. Liu, "Highly sensitive compression sensors using three-dimensional printed polydimethylsiloxane/carbon nanotube nanocomposites." *Journal of Intelligent Material Systems and Structures.* 2019;30(8):1216-1224.

7) M. Abshirini, M. Charara, Y. Liu, M. C. Saha, M. C. Altan. “3D Printing of Highly Stretchable Strain Sensors Based on Carbon Nanotube Nanocomposites.” *Advanced Engineering Materials*. 2018;20(10):1800425.

Conference Papers

1) M. Abshirini, M. C. Altan, Y. Liu, M. C. Saha, “Investigation of Pore Size Distribution and Mechanical Properties of Porous Polydimethylsiloxane (PDMS) Structures Using Solvent Evaporation Technique.” ASME International Mechanical Engineering Congress and Exposition. Vol. 85574. *American Society of Mechanical Engineers*, 2021.

2) M. Abshirini, M. C. Altan, Y. Liu, M. C. Saha, L. Cummings, T. Robison, “Manufacturing of Porous Polydimethylsiloxane (PDMS) Plates Using Solvent Evaporation Induced Phase Separation Technique.” Technical Paper Publication, ASME International Mechanical Engineering Congress and Exposition. *American Society of Mechanical Engineers* , 2020.

3) M. Abshirini, M. Charara, M. C. Saha, M. C.Altan, Y. Liu, “Optimization of 3D Printed Elastomeric Nanocomposites for Flexible Strain Sensing Applications.” ASME International Mechanical Engineering Congress and Exposition. Vol. 59360. *American Society of Mechanical Engineers*, 2019.

4) M. Abshirini, M. Charara, Y. Liu, M. Saha, M. C. Altan, “Additive Manufacturing of Polymer Nanocomposites with In-Situ Strain Sensing Capability.” Technical Paper Publication, ASME 2018 International Mechanical Engineering Congress and Exposition. *American Society of Mechanical Engineers*, 2018.

List of Figures

Figure 1. 1. Experimental setup for measuring the piezoresistive response in a compressive load [25]. 3

Figure 1. 2. Porous framework with (a) interconnected pores and (b) isolated cellular pores fabricated with different methods [8]. 5

Figure 1. 3. Schematic of direct templating procedure to create a 3D porous structure [41]. 6

Figure 1. 4. (a) Photograph of a cube sugar template. (b) PDMS sponge after removing the templates. (c) optical microscope and (d) SEM image of the cross-sectional area of the sponge. (e) manual 50% strain compression and (f) recovery to the original shape. PDMS sponge wettability showing (g) high hydrophobicity and (h) strong oleophilicity of the surface [40]..... 7

Figure 1. 5. Schematic showing the emulsion mechanism in (a) oil in water concentrated emulsion (b) water in oil concentrated emulsion [46]. 9

Figure 1. 6. (a) SEM image of a typical polyHIPE porous polymer (V and W indicate void and window, and the scale bar is 20 μm. (b) open-cell structure of the HIPE pore [45]. 9

Figure 1. 7. Schematic showing the phase separation mechanism in LSR/LP/hexane solution [49]. 11

Figure 1. 8. SEM image showing the porous SR structure cured at different temperature levels (a) 30 ^{o}C, (b) 40 ^{o}C, (c) 50 ^{o}C [49]. 11

Figure 2. 1. Ternary phase diagram for the polymer/solvent/nonsolvent system [49]. 19

Figure 2. 2. Ternary phase diagram for PDMS/THF/Water system. 24

Figure 2. 3. Schematic showing the nucleation and growth, and spinodal decomposition mechanism of the pore formation [80]..... 25

Figure 3. 1. Schematic showing the preparation of polymer solution and molding. 30
Figure 3. 2. (a) Shape and dimensions of the dogbone sample (dimensions are in mm) and (b) the cutting die designed for the tensile test. 34
Figure 3. 3. Location of the failed formulation to create porous media on the ternary diagram. . 35
Figure 3. 4. Microscope images showing the pore distribution for the samples containing 40% PDMS with (a) α =8, (b) α =6, (c) α =4, (d) α =3, (e) α =2, and (f) α =1. 37
Figure 3. 5. Microscope images showing the pore distribution for the samples containing 60% PDMS with (a) α =8, (b) α =6, (c) α =4, (d) α =3, (e) α =2, and (f) α =1. 37
Figure 3. 6. The average pore size obtained for (a) 40% PDMS and (b) 60% PDMS with different Water/THF ratios (the points show the average values, errorbars show the standard deviation, and the lines show the second-order curve fit). 39
Figure 3. 7. The average pore size for the samples with α=2 and different PDMS concentrations (the errorbars show the standard deviation). 40
Figure 3. 8. The pore size distribution for samples with 40% PDMS containing (a) α=3 and (b) α=4. 41
Figure 3. 9. (a) The dogbone samples used for the tensile tests, and (b) failure mode of the tested samples. 42
Figure 3. 10. Sample with α=3 (a) at the strain of ε=0% (initial) and (b) at the strain of ε=60%. 42
Figure 3. 11. The stress-strain curves for the samples with different α contained (a) 40% and (b) 60% PDMS concentrations. 43

Figure 3. 12. (a) strain for the samples with 40% PDMS 0.18 MPa stress, (b) stress for the samples with 40% PDMS at 0.4 mm/mm strain, (c) strain for the samples with 60% PDMS at 0.18 MPa stress, and (d) stress for the samples with 40% PDMS at 0.4 mm/mm strain..... 44
Figure 3. 13. Stress-strain curve for the samples with α=2 and different PDMS concentrations, and (b) comparing the strains for the samples with different PDMS weights at the stress of 0.2 MPa. 45
Figure 3. 14. (a) the porosity of the samples with 40% and 60% PDMS and various α, and (b) comparing the porosity of the specimens with α=2 and different PDMS concentrations (the errorbars show the standard deviation). 46
Figure 4. 1. (a) Dimensions of the dog bone sample (dimensions are in mm); (b) nonporous PDMS sample, (c) porous PDMS sample with THF/solvent= 10:10; (d) THF/solvent= 5:10; and (e) THF/solvent= 2:10 for the mechanical testing. 55
Figure 4. 2. SEM images for the sample prepared with THF/solvent = 3:10 showing (a) combinations of small and large pores in the sample (bar is 300 μm), (b) small pores within the cell edges as well as cell faces of the large pore (bar is 30 μm), and (c) distribution of the small pores (bar is 15 μm). 56
Figure 4. 3. Pore size distribution for (a) large pores and (b) small pores within all the samples fabricated with different formulations. 57
Figure 4. 4. SEM images showing the porous microstructure in the samples with (a) THF/solvent=0:10, (b) THF/solvent=2:10, (c) THF/solvent=4:10, (d) THF/solvent=6:10, (e) THF/solvent=8:10, and (f) THF/solvent=10:10 (scale bar is 200 μm in all images). The arrows from “a” to “f” show the increase in the large pore density and decrease in small pore density as the THF in the solvent is increased. 58

Figure 4. 5. SEM images showing the large pore and windows in the samples with (a) THF/solvent=1:10, (b) THF/solvent=3:10, (c) THF/solvent=7:10, and (d) THF/solvent=9:10, (scale bar is 80 μm in all images). 60

Figure 4. 6. The variation of the relative area fraction of large pores, ρ_L, with an increasing THF/solvent ratio (points show the average value, errorbars show the standard deviation, and the line shows the second order curve fit) 61

Figure 4. 7. The porosity of the samples with different microstructures fabricated from various solvent formulations (errorbars show the standard deviation). 62

Figure 4. 8. (a, b) Stress-strain curve and their initial region for the porous samples with different microstructures of ρ_L=0% (THF/solvent=0:0), ρ_L=30% (THF/solvent=3:10), ρ_L=54% (THF/solvent=5:10), ρ_L=86% (THF/solvent=8:10), ρ_L=100% (THF/solvent=10:10), (c) the mechanical behavior of solid PDMS, and (d) variation of elastic modulus as a function of ρ_L (points show the average, errorbar show the standard deviation, and the line shows the fitted curve). 64

Figure 4. 9. (a) Strength and (b) failure strain of the porous PDMS with different microstructures ranging from ρ_L=0% (THF/solvent=0:0) to ρ_L=100% (THF/solvent=10:10) (errorbars show the standard deviation). 65

Figure 4. 10. The variation of modulus with changing the loading rate for different porous samples with ρ_L=0% (THF/solvent=0:0), ρ_L=30% (THF/solvent=2:10), ρ_L=46% (THF/solvent=4:10), ρ_L=54% (THF/solvent=5:10), ρ_L=68% (THF/solvent=6:10), ρ_L=86% (THF/solvent=8:10), ρ_L=100% (THF/solvent=10:10). 66

Figure 4. 11. (a) Representative stress-strain curve during the loading-unloading cycle, and (b) the rate-dependency of hysteresis for different samples. 67

Figure 5. 1. (a) Schematics showing different steps of the preparation, 3D printing, and curing of porous CPNC, (b) DIW of a disc-shaped sensor (with 0.5-inch diameter) and the cured sample, and (c) DIW of complex geometry with fine nozzle (27 gauge) and the cured sample. 77

Figure 5. 2. (a) Variation of viscosity as a function of shear rate and (b) viscosity at 1 s^{-1} shear rate for solutions with different CNT concentrations (the errorbars show the standard deviation). 81

Figure 5. 3. (a) Amplitude sweep test results and (b) yield stress for the mixtures with various CNT concentrations (the errorbars show the standard deviation). 82

Figure 5. 4. SEM images of the micro-scaled porosity in the CPNC sample with 1% CNT: (a) low magnification image showing no voids or air trapped in the structure during the DIW, (b) pore distribution in the internal face, (c) the joining area of three adjacent cells, and (d) SEM image of a cell wall where some CNTs stick out from the cell wall, and some lay down on the wall..... 83

Figure 5. 5. The pore size distribution for the porous structures with (a) 1% CNT and (b) 2% CNT; (c) average pore diameter vs. CNT concentration of the CPNC samples (the points show the average values and the errorbars show the standard deviation), and (d) the porosity in the 3D printed samples with different CNT loadings (the errorbars show the standard deviation). 85

Figure 5. 6. (a) stress-strain curve during the compression loading-unloading of porous samples, (b) stress-strain curve during the compression loading-unloading for 1% CNT solid sample, (c) comparison of stress at the 10% strain, and (d) comparison of strain at the 50 kPa stress for the samples with different CNT concentrations (the errorbars show the standard deviation)..... 86

Figure 5. 7. Effect of CNT on (a) conductivity (points show the average values and the errorbars show the standard deviation) and (b) piezoresistive response at different strains of the porous

CPNC (points show the average values, the errorbars show the standard deviation); (c) comparing GF at 10% strain for different CNT loadings (the errorbars show the standard deviation); and (d) representative signal response at multiple strains for the sample with 1% CNT..... 89

Figure 5. 8. The effect of strain rate on (a) mechanical and (b) piezoresistive response of the CPNC sample under compression load up to 15% strain (points show the average values, the errorbars show the standard deviation), and (c) the relative changes in the values of stress and GF at different strain rates compared to the values at 0.001 s^{-1} (points show the average values, the errorbars show the standard deviation). 92

Figure 5. 9. (a) relaxation behavior showing changes in the stress and resistance under 15% strain load for three hr.; and (b) piezoresistive response in the fatigue compression load up to 15% strain for 700 cycles and details of comparing five cycles at three different times in the test. 93

Figure 5. 10. Piezoresistive sensing response of the porous CPNC samples mounted on a cell phone to detect the human motion during (a) press-hold turn off/on button for 5 seconds, (b) press-hold volume up/down button for 3 seconds, and (c) press-release home button. 95

Figure 5. 11. (a) 3D printed CPNC attached on the throat to detect the muscle movement during speaking, (b) sensing response when “Hello” was pronounced, (c) sensing response when “Hi” was pronounced, and (d) sensing response when “Bye” was pronounced. 96

Figure 6. 1. (a) Schematic illustrates different material preparation steps, 3D printing, and phase separation. (b) pictures of a dual-scale porous sample during DIW and after the heat treatment, and (c) highly flexible porous CPNC can be squeezed and released to the original shape by a finger. 104

Figure 6. 2. (a) effect of shear rate on the viscosity and (b) comparison of the viscosity at 0.01 s^{-1} shear rate for the inks prepared using different silica loadings (the errorbars show the standard deviation). 109
Figure 6. 3. (a) The amplitude sweep test results and (b) the yield point for the inks prepared with various silica loadings (the errorbars show the standard deviation). 110
Figure 6. 4. SEM images of the samples with 40% infill and 40% PDMS: (a) Macroscale pores, (b) area between four adjacent macroscale cells, (c) microscale porous network, (d) CNTs are sticking out from a microscale cell wall. (e) Low and (f) high magnification SEM images of the samples with 100% infill and 40% PDMS. (g) Low and (h) high magnification SEM images of the samples with 40% infill and 100% PDMS..... 112
Figure 6. 5. The effect of infill density on (a) macroscale and (b) microscale pore size. The effect of PDMS weight on (c) macroscale and (d) microscale pore size (the errorbars show the standard deviation in all the curves). SEM images of samples made with (e) 30% and (f) 40% PDMS.. 114
Figure 6. 6. The effect of needle size on (a) macroscale pore and (b) microscale pore size (the points show the average values, and the errorbars show the standard deviation). The SEM images show the area between four adjacent macropores in the samples printed with (c) 0.21 mm and (d) 0.33 mm needle. 115
Figure 6. 7. Effect of (a) PDMS loading, (b) infill density, and (c) needle size on the porosity of the CPNC structures (the points show the average values, and the errorbars show the standard deviation in all the curves). 117
Figure 6. 8. (a) Stress-strain up to 70% strain load and (b) cyclic strain-strain up to 30% strain for the samples with different PDMS wights. (c) cyclic stress-strain curves for full solid and 100% PDMS samples. Comparison of (d) specific modulus (the errorbars show the standard deviation),

and (e) strain at 100 kPa for the samples with different PDMS loadings (the errorbars show the standard deviation). 119
Figure 6. 9. (a) Stress-strain up to 70% strain load and (b) cyclic strain-strain up to 30% strain for the samples with different infill densities. Comparison of (c) specific modulus (the errorbars show the standard deviation), and (d) strain at 100 kPa for the samples with different infill densities (the errorbars show the standard deviation). 121
Figure 6. 10. (a) Stress-strain up to 70% strain load and (b) cyclic strain-strain up to 30% strain for the samples with different needle sizes. Comparison of (c) specific modulus (the errorbars show the standard deviation) and (d) strain at 100 kPa for the samples 3D printed using different needle sizes (the errorbars show the standard deviation). 122
Figure 6. 11. Comparison of the experimental data and the 5-term Mooney-Rivlin hyperelastic model. 125
Figure 6. 12. Deformed FEA model with (a) 0.41 mm needle and (b) 0.21 mm needle size. Comparing experimental and FEA stress-strain curves for the samples with (c) 0.33 mm and 0.41 mm needle sizes, and (d) 0.26 mm and 0.21 mm needle sizes. 127
Figure 6. 13. (a) Electrical resistance changes in the five loading-unloading cycles with different maximum strains, (b) The GF at different strains for samples with various PDMS loadings, (c) The GF at different strains for samples with various infill densities, and (d) The GF at different strains for samples 3D printed with different needle sizes (the points show the average values, and the errorbars show the standard deviation). 129
Figure 6. 14. Comparing the durability of the piezoresistive response in the dual-scale porous and full solid sample, and (b) Comparison of the cyclic sensing response between the full solid and dual-scale porous sample. 131

Figure 6. 15. Detection of human body motion: (a) Piezoresistive response related to grabbing a mug filled at different levels. (b) sensing response caused by a thumb related to (b) continuous press/release and (c) press/hold/release. Detection of throat muscle movement during (d) drinking and (e) pronouncing the word “sensor”..... 132

List of Tables

Table 3. 1. Material formulations of the polymer solution prepared for the experiments. 31

Table 3. 2. Stepping heat treatment procedure for inducing phase separation. 32

Table 4. 1. Different ternary formulations are used for creating the ternary PDMS solution. 51

Table 4. 2. Hysteresis (%) in different samples at multiple strains. 68

Table 4. 3. Comparison of modulus and ρ_L calculated from experiments with the empirical model..... 69

Table 5. 1. Comparing the sensitivity (gauge factor) of the PDMS-based nanocomposites. 89

Table 6. 1. The information of different samples 3D printed in this study..... 105

Table 6. 2. The hyperelastic material constants calculated using the Mooney-Rivlin model. ... 124

Chapter 1: Introduction

1.1. Conductive Polymer Nanocomposites

Highly flexible electrically conductive materials have drawn significant attention due to their promising applications in many fields, including electronic skin [1], biomedical applications [2], health monitoring [3], and body movement detection [4]. Recently, conductive polymer nanocomposites (CPNC) have been implemented as flexible and stretchable/compressible strain sensors owing to the outstanding deformation capability compared with the conventional rigid strain sensors.

CPNCs mainly consist of two material groups. The first group is the flexible polymer matrix. Different polymers have been utilized as the matrix in the CPNC, such as thermoplastic polyurethane (TPU) [5], Ecoflex [6], and polydimethylsiloxane (PDMS) [7]. PDMS is a non-toxic, organic elastomer polymer that has received growing attention over the past few years. The great moldability, electrical, thermal, and mechanical properties of PDMS have made it suitable for feasible uses [8]. This material has been widely utilized in conductors, strain sensors, and biomedical applications due to its outstanding viscoelastic and biocompatible properties. Flexible conductors and strain sensors are the most important fields in which the mechanical or electrical properties of PDMS can be modified by providing a porous structure. Different porous structures can be produced using PDMS as a primary polymer based on the desired feature.

The second material in the CPNCs is conductive nanomaterials, including carbon nanotubes (CNTs) [9], metal nanowires and nanoparticles [10, 11], and carbon nanofibers [12]. Multiwalled

carbon nanotubes (MWNTs) are of particular interest due to their outstanding electrical, mechanical, and thermal properties. The high electrical conductivity of MWCNTs has been utilized in several innovative ways to enhance the conductivity of nanocomposites, resulting in new piezoresistance-based autonomous load-sensing capabilities [13]. The addition of conductive nanofillers to the flexible matrices endows the base material with electrical properties, which can be exploited to measure its deformation. Both capacitance-based and resistance-based strain sensing mechanisms have been reported in the literature, though the electrical resistance-based method is more commonly reported [13-15].

1.2. Piezoresistive Strain Sensor

Piezoresistive strain sensors work by converting and detecting a mechanical stimulus into an electrical response. The conductive materials can be placed between two electrodes connected to a resistance meter or multimeter device. The applied strains can be calculated by measuring electrical resistance change resulting from mechanical deformation in these materials. As an example, the experimental setup for measuring the piezoresistive response of a nanocomposite material under a compressive load is shown in Figure 1.1. The recent scientific progress in the use of electronic devices for strain sensing applications has attracted significant attention in the fields of soft robotics [16, 17], electronic skins [18-20], and wearable devices for human health monitoring [21-23]. These applications require flexible strain sensors with high sensitivity and durable performance. In general, the strain sensing range and sensitivity are two key parameters used to evaluate the quality of sensors. Particularly, the sensitivity, also known as the gauge factor (GF), is defined as the ratio of relative electrical resistance change to applied strain. Conventional metallic strain gauges offer a low GF (around 2) and a limited sensing range (less than 5% strain),

while semiconductor-based sensors offer high GFs but a limited detection range, making neither suitable for wearable sensing applications [24].

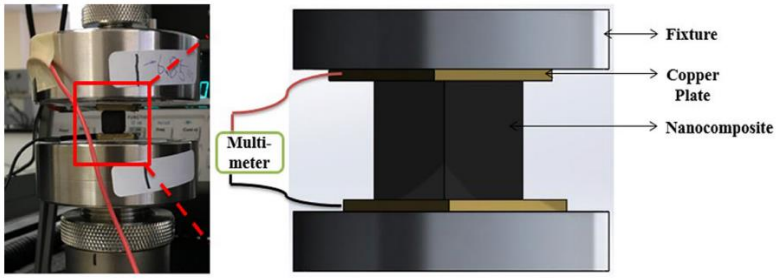

Figure 1. 1. Experimental setup for measuring the piezoresistive response in a compressive load [25].

1.2.1. Application of CPNC in Piezoresistive Strain Sensing

CPNC structures with high flexibility and sensitivity are the most popular advanced materials for novel sensing applications. The change in electrical resistance is believed to be induced by the reorganization of the electrically conductive network formed by nanofillers under mechanical stimulus (i.e., tension or compression). Among the conductive nanofiller mentioned, MWNTs have been widely used to improve the conductivity of these polymerm due to their excellent electrical characteristics at low concentrations [26-28]. The piezoresistive response in the nanocomposite materials has been previously observed [29].

Low sensitivity and limited strain range are two challenges in developing piezoresistive sensors to fulfill novel applications. For example, many developed strain sensors have high GF only at low strain ranges [30-32]. In addition, most elastomeric CPNC suffers from low compressibility due

to the poor compressive mechanical properties of the polymer [33]. Multiple methods have been introduced to increase the sensitivity of the sensors. Micro/nano cracks [34], fracture and bridging [35], and wrinkling of nanomaterial films [36] have been created to enhance the connect/disconnect in the conductive network, which improves the sensitivity. Porous CPNCs have also been shown to improve the sensitivity of the lightweight sensors by creating new conductive paths in the cells during loading-unloading [37]. In addition to increasing the sensitivity, porous networks enhance the flexibility and compressibility of the structures by providing superior surface areas [5].

1.3. Porous Polymers

Considering the specific structure of porous polymers, this composition has unique properties compared to the bulk material, such as high adsorptive capacity, high flexibility, upper surface area, and low gas resistance. These properties make porous media have great potential for different fields, including oil/water absorption, separation, energy storage, wearable electronics, biomedical, and many other applications. Therefore, significant interest has been devoted to designing and synthesizing porous structures for the desired applications recently. There are two primary purposes for manufacturing porous polymers. In the first goal, the porous structures, because of their nature, are essential for specific applications, such as membranes, oil/water separation or absorption, energy storage, biomedical scaffolds, etc. In the second goal, the general performance of polymers is modified by making them in porous form. Flexible conductors and strain sensors are among the most important fields in which mechanical or electrical properties of polymers can be modified by providing a porous structure. It has been reported that the porous PDMS has higher flexibility compared to the bulk, nonporous material [25]. In addition, it has been established that the porous PDMS-based nanocomposites used as strain sensors have higher

sensitivity compared to the solid ones [38]. Based on the desired features, structures with different bulk porosity, pore size, and pore morphology can be produced using PDMS as a primary polymer phase.

1.4. Different Porous Polymer Fabrication Methods

The methods for creating polymeric porous structures can be divided into different groups based on the fabrication process. The appropriate fabrication process should be selected based on the desired application considering the structure of the pores, such as pore size, porosity, pore geometry, and porous framework [8]. For example, Figure 1.2 describes the difference between the porous structure with interconnected pores (Figure 1.2a) and isolated cellular pores (Figure 1.2b), which can be produced by different fabrication methods. An overview of the conventional fabrication methods of the porous polymers is summarized.

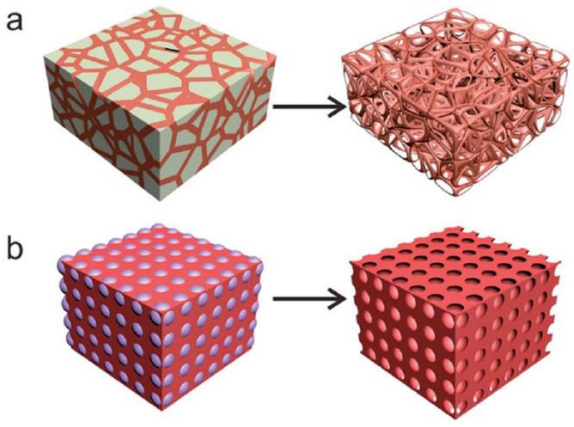

Figure 1. 2. Porous framework with (a) interconnected pores and (b) isolated cellular pores fabricated with different methods [8].

1.4.1. Direct Templating Technique

The direct templating method is one of the most popular techniques to create porous polymers. In this method, solid particles with stable morphologies are dispersed in the polymer substrate. The polymerization process is performed in the next step. Then, the particles are removed after the curing process leading to the cavities in the structure with different interconnections. The surface of the templates used in this technique should be compatible with the polymer substrate. In addition, the particles should be easily removed from the structure after finishing the templating process. For example, NaOH is used to dissolve silica, and water is used to extract sugar/salt particles [39]. The most popular particles used in this method are sugar cubes and salt crystals based on the non-toxicity and simplicity of these materials. Generally, the size of pores depends on the size of the template, and the porosity is related to the mixing ratio of the polymer to the solid particles [40]. The schematic of the direct templating method is shown in Figure 1.3, where salt crystals with two ranges of (48-65 µm and 150-297 µm) are used to create a porous framework [41]. The results revealed that the pore structure is square and very close to the temple size.

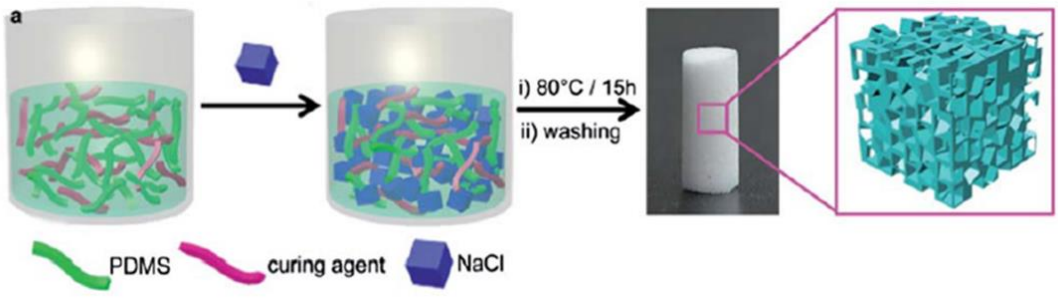

Figure 1. 3. Schematic of direct templating procedure to create a 3D porous structure [41].

Choi *et al*. [40] employed sugar templates for developing PDMS sponges with hydrophobic and oleophilic properties to absorb oil from water. The shape of the PDMS sponge and the hydrophobic/oleophilic behavior of the sponge is shown in Figure 1.4. The sponge's high elastic properties were observed by applying 50% strain and recovering the original shape.

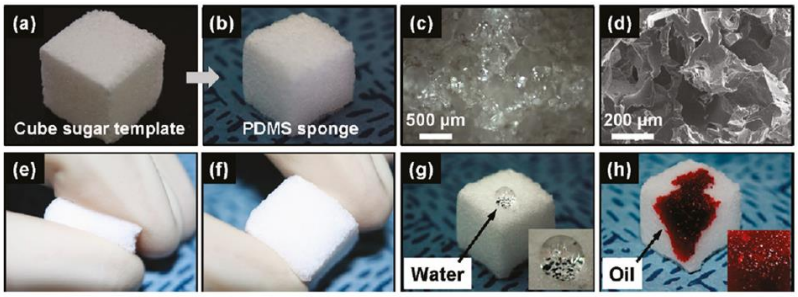

Figure 1. 4. (a) Photograph of a cube sugar template. (b) PDMS sponge after removing the templates. (c) optical microscope and (d) SEM image of the cross-sectional area of the sponge. (e) manual 50% strain compression and (f) recovery to the original shape. PDMS sponge wettability showing (g) high hydrophobicity and (h) strong oleophilicity of the surface [40].

Controlling the pore sizes is a challenge in this technique considering the limitation of the size and variation on sauger (400-1800 µm) or salt (50-297 µm [41]) temples. Although some studies have been performed using nanoparticles, including Zinc oxide powder and silica nanoparticles as templates [8], it is hard to incorporate these nanomaterials and remove them after curing.

1.4.2. Emulsion Templating Technique

In the emulsion templating technology, the emulsion droplets behave as a template, and the porous polymer structure is synthesized by polymerization of the continuous phase of an emulsion. The emulsion templates are categorized into three groups based on the internal phase volume ratio.

High internal phase emulsion (HIPE) has a volume higher than 70%, medium internal phase emulsion (MIPE) has a volume between 30-70%, and low internal phase emulsion (LIPE) has an internal volume below 30% [42]. After polymerization, the product is named polyHIPE, polyMIPE, and polyLIPE, respectively. Polymerization of the monomers dissolved in the continuous phase, and the subsequent removal of the droplet phase, resulting in the porous polymer in this technique. Both water-in-oil emulsion (W/O) and oil-in-water emulsion (O/W) are fabricated with this method, while W/O HIPEs are the most common structure [43]. In addition, both interconnected and separated pore distribution are reported in the literature [8]. It is shown that an internal phase concentration of less than 60% mostly results in close cell pores, while a highly interconnected pore structure can be achieved by HIPE [44]. The schematic of this mechanism is illustrated in Figure 1.5.

Microemulsion templates are formed in droplets suspended in another immiscible phase by utilizing the surfactants to thermodynamically stabilize the system. As shown in Figure 1.5, the surfactants' polar head and hydrophobic tail around the water (micelle) or oil (reverse micelle) droplets create a stable system with minimum interfacial energy. There are two types of cavities in the higher volume fraction. The polyHIPE beaded porous structure contains a large pore called void, and small pores in each void called a window, as shown in Figure 1.6 [45].

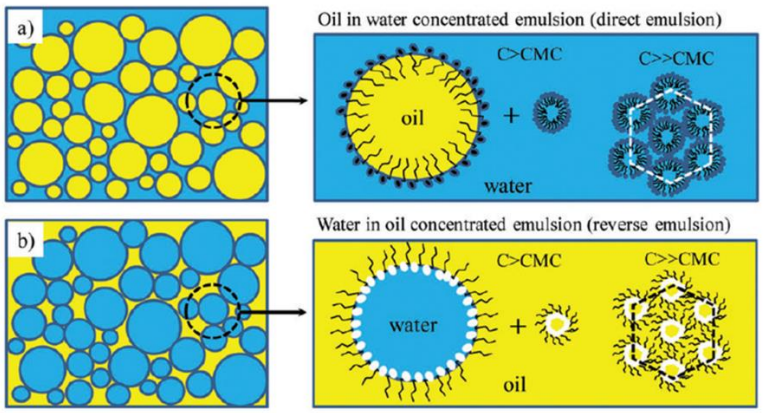

Figure 1. 5. Schematic showing the emulsion mechanism in (a) oil in water concentrated emulsion (b) water in oil concentrated emulsion [46].

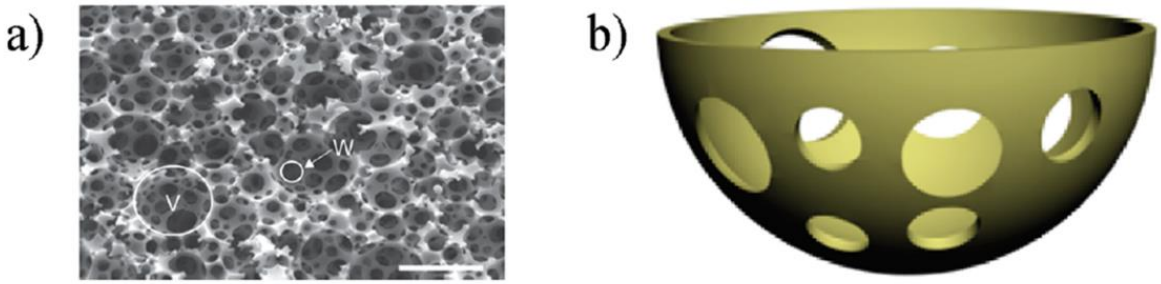

Figure 1. 6. (a) SEM image of a typical polyHIPE porous polymer (V and W indicate void and window, and the scale bar is 20 µm. (b) open-cell structure of the HIPE pore [45].

Recently, porous PDMS structures with controllable porosities have been fabricated employing different types of surfactants, nonionic (Triton X-100), cationic (Benzalkonium chloride), anionic (sodium dodecyl sulfate), and silicone-based block copolymer was used to stabilize the water-in-oil emulsion system [47]. The porosity and pore size distribution can also be adjusted in this technique. However, surfactants are used in this method which can affect the mechanical properties of the porous structures. Removing the surfactants from the cured polymer also requires additional effort.

1.4.3. Phase Separation Technique

Both three-dimensional (3D) porous structures and porous films have been produced by the phase separation technique [48]. In this method, a stable homogeneous phase (solution) is prepared containing primary and secondary materials. Then, the stable system is changed to two unstable phases. One of the two phases forms the droplets by the nucleation and growth mechanism, which results in a porous structure [49]. The phase separation technique can be divided into multiple sub-groups based on the approaches to induce the phase separation. The most common mechanism is solvent evaporation-induced phase separation (EIPS) [48]. In this method, two materials with different solubility in a solvent are mixed to create a homogeneous solution. By evaporating the solvent, one phase system changes to an unstable system, causing phase separation, and the formation of droplets occurs by the phase with a lower solubility in the solvent.

In a study performed by Zhao *et al*. [49], porous silicon rubber films are fabricated by evaporation of hexane solvent from the liquid silicon rubber (LSR)/liquid paraffin (LP)/hexane solution. By removing the solvent, one phase system is changed to LP-rich and LP-poor domains. The LP droplets are formed in the LP-rich zone, which coalesced to create larger droplets. The schematics of the solvent evaporation induced phase separation is depicted in Figure 1.7. The cured film is immersed in hexane solvent for four days to eliminate the LP phase from the porous structure after removing all the solvent and curing of silicon rubber. The SEM image of the micropores in the porous membrane cast at different temperatures is illustrated in Figure 1.8. It is shown that increasing the casting temperature results in larger pore size.

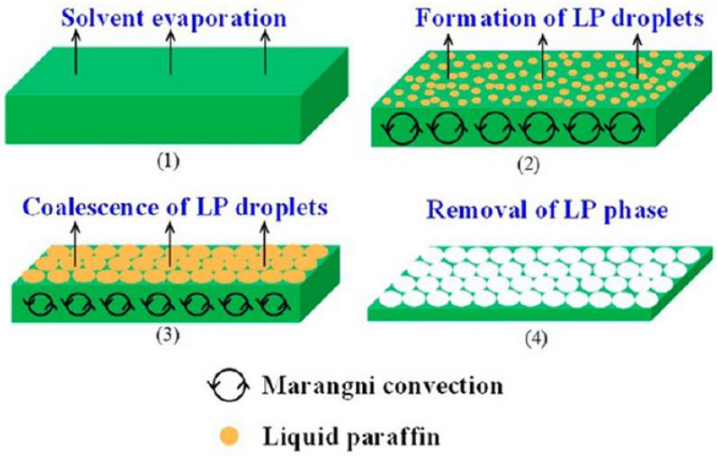

Figure 1. 7. Schematic showing the phase separation mechanism in LSR/LP/hexane solution [49].

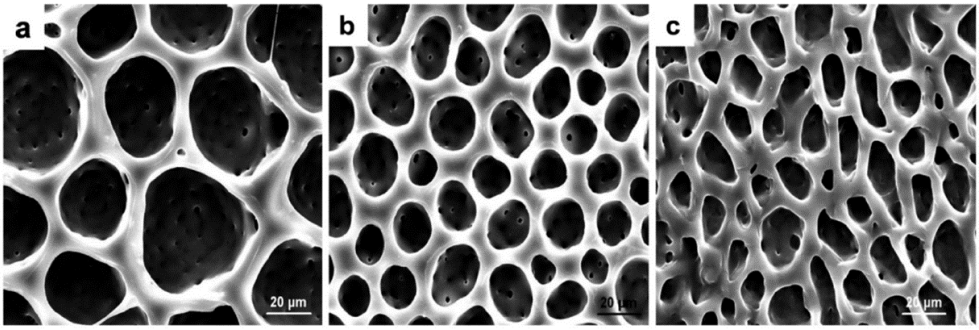

Figure 1. 8. SEM image showing the porous SR structure cured at different temperature levels (a) 30 ^{o}C, (b) 40 ^{o}C, (c) 50 ^{o}C [49].

One of the advantages of the phase separation technique is mixing the polymers or solvents in the ternary mixture. Solvent mixtures with similar solubility or polymer mixtures with different properties can be employed. Kim *et al*. [50] developed two phase separation steps in a polymer solution by removing the solvent from the system. In this study, Polystyrene (PS) and polyethylene glycol (PEG) are mixed with the toluene solvent to create the solution. The solubility of PEG in

toluene is less than PS in toluene. By starting the solvent evaporation, the phase for which the solvent is poor solvent (PEG), precipices from the solution. This results in PEG-rich and PEG-poor (PS-solvent rich) domains. The precipitated PEG-rich forms droplets on the surface, which by coalescing mechanism, create larger droplets. By continuing the solvent evaporation, the secondary phase separation occurs in each PG-rich droplet. In this step, the remaining solvent in each PEG droplet creates a spherical shape in the center of each droplet. Removing the solvent leads to creating cavities in the center of droplets forming the pore structure. After removing all the toluene, the pores in the shape of a ring surrounded by PEG inside the PS are formed.

1.5. Porous CPNC for Sensing Applications

Several techniques have been utilized for creating porous CPNCs for sensing applications. Solid templating is one of the most common techniques for developing porous networks using a sacrificial porogen with solid particles, such as salt and sugar [25, 51]. Open-cell structures with a high interconnection network can be achieved using this technique. However, the fabrication technique is not simple, and additional effort is needed to remove the solid particles after polymer curing. In the dip-coating method, a previously prepared polymer sponge is immersed in the nanomaterial solution, and the conductive network is transferred into the porous structure [52, 53]. Emulsion templating has been used for porous CPNC fabrication by creating water-in-oil emulsion droplets and removing the aqueous phase after polymerization [54, 55]. Porosity can be controlled by adjusting the aqueous phase's volume. Although the porosity can be controlled by adjusting the internal phase, surfactants are used in this technique, sacrificing the structure's mechanical properties, and additional effort is necessary to remove them [47].

Phase separation also has been used for developing porous CPNC. A homogeneous polymer solution is transferred into polymer-rich and polymer-lean phases based on the specific method used to induce phase separation. The droplets form and gradually grow, leading to a porous network after removing the secondary phase. The thermally induced phase separation technique has been utilized to fabricate porous TPU nanocomposites [5, 56]. EIPS has also been used for triggering phase separation to develop pristine porous polymers [49]. However, little attention has been devoted to using this technique to fabricate porous CPNCs. This method is straightforward, and the porous network is developed during the stepping heat treatment while the polymer is ongoing its curing cycle. The porosity can be controlled by adjusting the polymer weight in the ternary solution. However, little attention has been devoted to the simplicity and ability of this method for creating porous CPNCs for sensing applications.

1.6. Additive Manufacturing of CPNC

Most porous CPNC and even solid strain sensors have been fabricated using conventional molding and casting methods. Additive manufacturing (3D printing) has attracted significant interest recently as a rapid and accurate prototyping technology to fabricate 3D geometries layer-by-layer through a nozzle. Fused deposition modeling (FDM) is the most common additive manufacturing technique involving the melting and deposition of conductive thermoplastic polymer-based materials [57, 58]. Multiple 3D printing technologies have been introduced for manufacturing of conductive thermoset polymers by deposition of viscoelastic ink, such as aerosol jet printing [59], jet deposition of ink droplets [60], embedded 3D printing [61], and direct ink writing (DIW) [13, 33]. It is reported that DIW can be used for printing 3D geometries if the polymer ink has specific rheological properties. Having solid-like properties at low shear stress with sufficient storage modulus to retain the deposited shape and support the above layers; possessing a yield point to

enable flowing during the deposition and getting back to the solid-like properties after deposition, and shear thinning behavior to enable a smooth flow inside the nozzle without choking are the main features of ink for DIW of 3D geometries [62].

Due to their thixotropic flow properties, PDMS can be 3D printed under ambient conditions and used to create relatively thin multi-material devices [63]. Although the printed PDMS can maintain its geometric fidelity after curing, the low elastic modulus of the pre- and post-cured PDMS and its deformation under gravity still restrict the 3D geometries that can be fabricated due to the lack of self-supporting. Hinton *et al*. reported a 3D printing method for PDMS in a hydrophilic support bath, aiming to enable true freeform fabrication of complex structures [64]. Dispersion of nanoparticles as rheological modifiers in PDMS can significantly improve materials' storage modulus and viscosity, leading to 3D printable and highly elastic nanocomposites. Among the common nanoparticles, CNTs, due to the high electrical conductivity and reinforcement capability, and silica nanoparticles, because of excellent compatibility with PDMS polymers, have been used in the literature [65].

1.7. Scope of Work

The primary focus of this study is to develop porous polymer structures and porous CPNC with piezoresistive sensing functions. The goal is to develop a formulation to control the porous structures' porosity, pore morphology, and mechanical properties based on the desired applications. In addition, 3D printing of porous CPNC is investigated in this research for rapid and accurate fabrication of 3D sensors. One of the advantages of 3D printing with less attention in the fabrication of porous strain sensors is the ability to design structural patterns (e.g., grid, honeycomb, etc.) with adjustable infill densities. These patterns behave as macroscale porosity in

the CPNC structures, enhancing the sensors' light-weight, flexibility, and stretchability/compressibility. This technique has been used to develop macro-scale porous structures [65, 66]. However, DIW of porous structures with micro-scale pores has been challenging. Many conductive porous polymer fabrication processes are not compatible with 3D printing. For example, the solid templates can clog in the fine nozzle during the deposition, or dip coating requires immersing a sponge in the conductive solution. However, the phase separation method can be implemented in DIW since the pore formation is a post-processing step conducted during the heat treatment.

In this study, a simple and novel method is introduced for 3D printing of highly flexible porous CPNCs by combining DIW with the solvent evaporation induced phase separation technique. CPNC is prepared by dispersing CNT (as a conductivity/rheological modifier) at various concentrations in PDMS polymer. The ink is then prepared by mixing CPNC, solvent, and nonsolvent phases to achieve a homogenous CPNC solution. 3D structures with 100% infill density are deposited while the micro-scaled porous network is formed after printing during the curing cycle. Moreover, dual-scale porous CPNC is proposed to develop highly porous CPNC by controlling the structural pattern during 3D printing and using the phase separation method. A highly porous and flexible structure can be achieved without sacrificing mechanical performance. The macroscale porosity is established by adjusting infill densities and structural printing patterns, while microscale porosity is developed by EIPS of the deposited ink during the stepping heat treatment. This study significantly impacts different aspects of multifunctional materials, including porous polymers, porous nanocomposites, piezoresistive sensors, and 3D printing.

1.8. Objective

This dissertation constitutes a comprehensive study to develop highly porous and flexible polymer-based structures. The main objectives defined in this research can be categorized into the following groups.

I. Investigation of porous PDMS structures induced by the phase separation technique
II. Design of hierarchical porous PDMS structures with adjustable porosity, pore morphology, and mechanical properties
III. Additive manufacturing of porous conductive polymer nanocomposites developed using the phase separation technique
IV. Develop a simple and novel approach to achieve highly porous and flexible conductive polymer nanocomposites with dual-scale porosity and piezoresistive sensing functions

Chapter 2: Ternary Polymer Solution and Ternary Phase Diagram

2.1. Introduction

As it is mentioned in the introduction chapter, different types of mechanisms for inducing phase separation are reported in the literature, including thermally induced phase separation (TIPS), non-solvent induced phase separation (NIPS), vapor-induced phase separation (VIPS), and solvent evaporation-induced phase separation (EIPS). EIPS is a unique technique in which phase separation occurs by slowly removing the solvent from a polymer solution. This technique has been used for the fabrication of polymeric membranes [67, 68], porous electrospun fibers [69, 70], and porous polymeric plates [71]. A ternary polymer solution consists of polymer (P), non-solvent (NS), and solvent (S), which is miscible over a specific composition domain. The selection of these materials is that polymer dissolves in a mixture of a volatile solvent and a less volatile nonsolvent. By evaporating the solvent, one phase system changes to an unstable system, causing phase separation, and the formation of droplets occurs by the phase with a lower solubility in the solvent. This procedure is strongly depended on the thermodynamic and kinetic energy of the polymer solution. It has been shown that porous polymers with different pore size and morphology can be produced by changing the effective parameters, such as solvent/ nonsolvent, material molecular weight, and exterior environment [48].

2.2. Ternary Phase Diagram

The ternary phase diagram is a map describing the possible miscible, unstable, and composition changes of three materials in a ternary system. The behavior of a mixture containing polymer, solvent, and non-solvent phases can be described by this map. The ternary diagram can help to estimate and modify the phase separation procedure to achieve a porous structure with desired properties. A typical phase diagram of an NS/S/P ternary mixture is depicted in Figure 2.1. Region (A) shows the composition of a homogeneous polymer solution. The binodal curve demonstrates the single-phase and two-phase layout boundary, while the spinodal curve displays the unstable area (C). The region between the stable and unstable area is called the metastable zone (B), and the intersection of the binodal and spinodal curve is named the critical point. During the phase separation, the composition changes in either path 1 or path 2. The morphology of the final porous structure strongly depends on the composition pass. More detail about the role of the parameters in a ternary diagram will be explained later in this chapter.

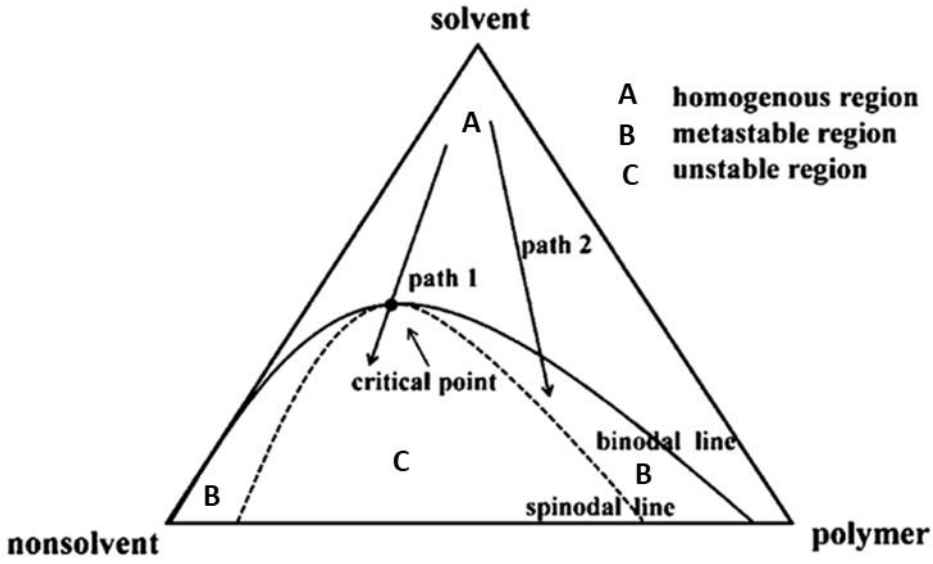

Figure 2. 1. Ternary phase diagram for the polymer/solvent/nonsolvent system [49].

In this section, the theoretical ternary phase diagram for PDMS as polymer, THF as a solvent, and Water as a non-solvent phase is described. The thermodynamic equations are derived to obtain the volume fractions required to build the phase diagram. The binodal, spinodal curve for this system is calculated numerically. Further information about the possible composition path changes and the final porous structure is described.

The thermodynamic behavior of the polymeric solution is described with the classical Flory-Huggins model [72]. Tompa [73] extended this approach to mathematically explain the ternary mixture containing non-solvent (1), solvent (2), and polymer (3) phases. Considering this method, the Gibbs free energy for such a mixture can be written as Eq. (2.1).

$$\frac{\Delta G_M}{RT} = n_1 ln\phi_1 + n_2 ln\phi_2 + n_3 ln\phi_3 + n_1\phi_2\chi_{12} + n_2\phi_3\chi_{23} + n_1\phi_3\chi_{13} \quad (2.1)$$

where *T*, is the absolute temperature, *R* is the gas constant; n_i and ϕ_i describe the number of moles, and the volume fraction of component *i*, respectively; χ_{ij} denotes the interaction parameter of a binary phase (*i*)/phase (*j*). By knowing the interaction parameters for a ternary polymeric solution, the phase diagram map containing binodal and spinodal curves can be obtained. The chemical potential of components in a mixture can be extracted from Eqs. (2.2)-(2.4) [74].

$$\frac{\Delta\mu_1}{RT} = ln\phi_1 + 1 - \phi_1 - \frac{\nu_1}{\nu_2}\phi_2 - \frac{\nu_1}{\nu_3}\phi_3 + (\chi_{12}\phi_2 + \chi_{13}\phi_3)(\phi_2 + \phi_3) - \chi_{23}\frac{\nu_1}{\nu_2}\phi_2\phi_3 - u_1u_2\phi_2\left(\frac{d\chi_{12}}{du_2}\right) - \phi_1{\phi_3}^2\left(\frac{d\chi_{13}}{d\phi_3}\right) - \frac{\nu_1}{\nu_2}\phi_2{\phi_3}^2\left(\frac{d\chi_{23}}{d\phi_3}\right) \quad (2.2)$$

$$\frac{\Delta\mu_2}{RT} = ln\phi_2 + 1 - \phi_2 - \frac{\nu_2}{\nu_1}\phi_1 - \frac{\nu_2}{\nu_3}\phi_3 + \left(\chi_{12}\frac{\nu_2}{\nu_1}\phi_1 + \chi_{23}\phi_3\right)(\phi_1 + \phi_3) - \chi_{13}\frac{\nu_2}{\nu_1}\phi_1\phi_3 + u_1u_2\frac{\nu_2}{\nu_1}\phi_1\left(\frac{d\chi_{12}}{du_2}\right) - \frac{\nu_2}{\nu_1}\phi_1{\phi_3}^2\left(\frac{d\chi_{13}}{d\phi_3}\right) - \phi_2{\phi_3}^2\left(\frac{d\chi_{23}}{d\phi_3}\right) \quad (2.3)$$

$$\frac{\Delta\mu_3}{RT} = ln\phi_3 + 1 - \phi_3 - \frac{\nu_3}{\nu_1}\phi_1 - \frac{\nu_3}{2}\phi_2 + \left(\chi_{13}\frac{\nu_3}{\nu_1}\phi_1 + \chi_{23}\frac{\nu_3}{\nu_2}\phi_2\right)(\phi_1 + \phi_2) - \chi_{12}\frac{\nu_3}{\nu_1}\phi_1\phi_2 + \left[\frac{\nu_3}{\nu_1}\phi_1\left(\frac{d\chi_{13}}{d\phi_3}\right) + \frac{\nu_3}{\nu_2}\phi_2\left(\frac{d\chi_{23}}{d\phi_3}\right)\right]\phi_3(\phi_1 + \phi_2) \quad (2.4)$$

where $\Delta\mu_i$ is the difference between the chemical potential of pure state and mixture for component *i*, $u_1 = \phi_1/(\phi_1 + \phi_2)$ and $u_2 = \phi_2/(\phi_1 + \phi_2)$ are the pseudo-binary mixture.

2.2.1. Binodal Curve

Based on the nature of the binodal curve, the chemical potential of the polymer-rich zone and polymer-lean zone are in equilibrium, as shown in Eq. (2.5)

$$(\Delta\mu_i)^I = (\Delta\mu_i)^{II}, \quad i = 1, 2, 3 \quad (2.5)$$

where *I* and *II* denote the polymer-rich and polymer-lean, respectively. There are six unknows in this equation, including $(\phi_1, \phi_2, \phi_3)^I$ and $(\phi_1, \phi_2, \phi_3)^{II}$. The binodal curve can be constructed by

multiple tie lines connecting two related nodes (one for polymer-rich and one for the polymer-lean phase). In addition to three equations achieved by substituting Eqs. (2.2)-(2.4) in Eq. (2.5). There are two relations based on the material balance at the polymer-rich and polymer-lean phases.

$$\sum(\phi_1, \phi_2, \phi_3)^I = \sum(\phi_1, \phi_2, \phi_3)^{II} = 1, \quad i = 1, 2, 3 \tag{2.6}$$

In order to calculate the six unknowns from the five coupled-nonlinear equations, one parameter can be considered as an independent variable (${\phi_3}^{II}$ in this study), and the remaining parameters can be solved using the least-square method. More information about the numerical calculation can be found in ref. [75].

2.2.2. Spinodal Curve

The spinodal curve representing the boundary between metastable and unstable regions can be obtained by Eq. (2.7) [74]

$$G_{22}G_{33} = {G_{23}}^2 \tag{2.7}$$

where $G_{ij} = \frac{\partial^2 \Delta G_M}{\partial \phi_i \partial \phi_j}$ is the second derivative of the Gibbs free energy respect to the composition. Using Eq. (2.1), it leads to Eqs. (2. 8)-(2.10).

$$G_{22} = \frac{1}{\phi_1} + \frac{\nu_1}{\nu_2 \phi_2} - \frac{\nu_1}{\nu_3}\phi_3 - 2\chi_{12} + 2\left(\frac{d\chi_{12}}{du_2}\right)(u_1 + u_2) + (\frac{d^2\chi_{12}}{du_2^2})u_1u_2 \tag{2.8}$$

$$G_{33} = \frac{1}{\phi_1} + \frac{\nu_1}{\nu_3 \phi_3} - \frac{\nu_1}{\nu_3}\phi_3 - 2\chi_{13} - 2\left(\frac{d\chi_{12}}{du_2}\right)u_2^2(1 - u_1) + (\frac{d^2\chi_{12}}{du_2^2})u_1u_2^3 \tag{2.9}$$

$$G_{23} = \frac{1}{\phi_1} - (\chi_{12} + \chi_{13}) + \frac{\nu_1\chi_{23}}{\nu_2} + \left(\frac{d\chi_{12}}{du_2}\right)u_2(u_1 - 2u_2) + (\frac{d^2\chi_{12}}{du_2^2})u_1u_2^2 \tag{2.10}$$

There are three unknowns required for the construction of the spinodal curve. Two coupled-nonlinear equations come from the substitution of Eqs. (2. 8)-(2.10) in Eq. (2.7), and the material balance ($\sum \phi_i = 1$). Similar to the binodal calculation, one parameter (i.e., ϕ_3) can be considered as an independent variable, and the other two parameters can be solved using the least-square numerical method.

2.2.3. Interaction Parameters

As described above, three interaction parameters are required to find the binodal and spinodal curves. Generally, the solvent-polymer binary interaction parameter (χ_{23}) is not dependent on the component's volume fraction. There are several experimental techniques to measure χ_{23}, including gas-liquid equilibrium, osmotic pressure, and light scattering [69]. The value of $\chi_{23} = 0.48$ is reported in the literature for THF/PDMS system at 20 ^{o}C [76]. The nonsolvent-polymer binary interaction parameter (χ_{13}) is usually calculated by the equilibrium swelling measurement [67]. When the polymer contacts non-solvent, the non-solvent diffuses in the polymer until the equilibrium state between the chemical potential of the liquid inside the polymer and inside the liquid phase is achieved. According to the Florye-Rehner theory, χ_{13} is dependent on the polymer concentration and can be expressed with Eq. (2. 11) [77, 78].

$$\chi_{13} = -\frac{\ln(1-\phi_3)+\phi_3}{{\phi_3}^2} \tag{2.11}$$

The non-solvent/solvent binary interaction parameter (χ_{12}) depends on the u_2 pseudo-binary mixture at different temperatures, which can be calculated from Eq. (2.12) [70].

$$\chi_{12} = \alpha_0 + \frac{\beta_0}{1-\gamma_0 u_2} \tag{2.12}$$

where α_0, β_0, and γ_0 are temperature-dependent parameters. The value of 0.720. 0.764, and 0.531 are reported for THF/Water systems at 20^{o}C, respectively [70].

2.3. Phase Diagram Results

The parameters required for constructing the phase diagram were calculated based on the numerical method described before. The thermodynamic ternary phase diagram for Water/THF/PDMS is illustrated in Figure 2.2. It is evident that the binodal and spinodal curves divide the phase map into three different regions. Region (A) is the homogenous domain where the mixture is stable. The area between spinodal and binodal curves (B) is called the metastable zone, while region (C) indicates the unstable area. The intersection of these two curves, called the critical point (CP) is shown in this figure. The CP for the water/THF/PDMS system was obtained as 39.6/52/8.4. The region above the CP is related to the polymer-rich zone, and the underneath area is the polymer-lean phase.

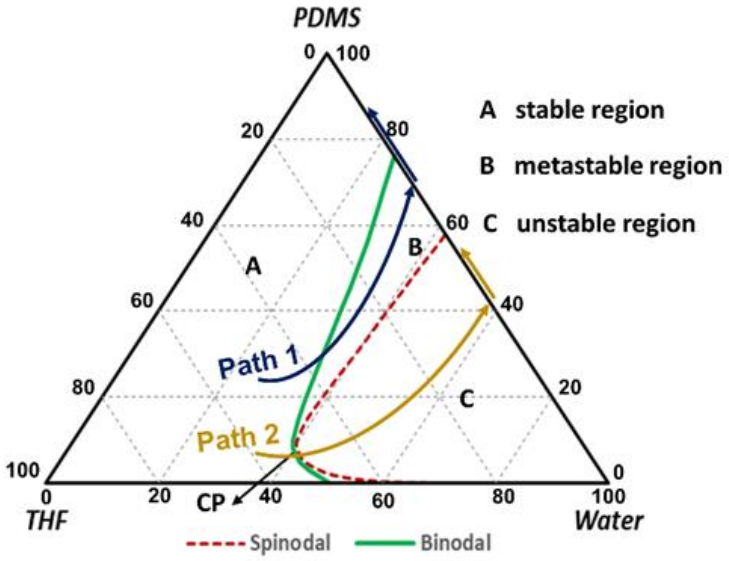

Figure 2. 2. Ternary phase diagram for PDMS/THF/Water system.

Two scenarios can be attributed to the phase separation mechanism based on the precipitation path on the phase diagram, as demonstrated in Figure 2.2. The nucleation and growth (NG) is the primary mechanism in the first scenario, where the composition slowly passes a line from a homogeneous region to the metastable domain (Path 1). The final porous structure, in this case, is the isolated cellular pores in the polymer matrix [70]. The nature of the phase separation is different based on the composition change path on the binodal curve. If the path is above the critical point, the isolated droplets containing non-solvent and solvent are formed in the continuous polymer-rich area. Then, these droplets are merged and grow by the concentration gradient until the polymer-rich phase solidifies. A thin layer of PDMS covers the droplets, considering the tension surface of the PDMS-rich domain, creating Water/THF encapsulation. If the composition path is located below the CP, the isolated droplets of the polymer-rich phase are formed in the polymer-

lean continuous phase. Similarly, the droplets are driven to grow until the continuous polymer-lean phase solidifies [79]. The encapsulated PDMS is the final product in this case.

In the second scenario, the mechanism of the pore formation is spinodal decomposition (SD) if the composition path passes the critical point (Path 2), leading to the liquid-liquid demixing in the unstable region (C in Figure 2.2). Continuous pore structures with interconnected networks are formed by the SD mechanism [49]. Considering the solvent evaporation in the phase separation procedure and the location of the CP in the ternary diagram, it is most likely that NG is the pore formation mechanism of any formulation for Water/THF/PDMS solution. Because of the same reason, it can be claimed that the NG occurs in the polymer-rich domain, and the product is the isolated droplets in the polymer matrix. The schematic of the NG and SD mechanism is shown in Figure 2.3.

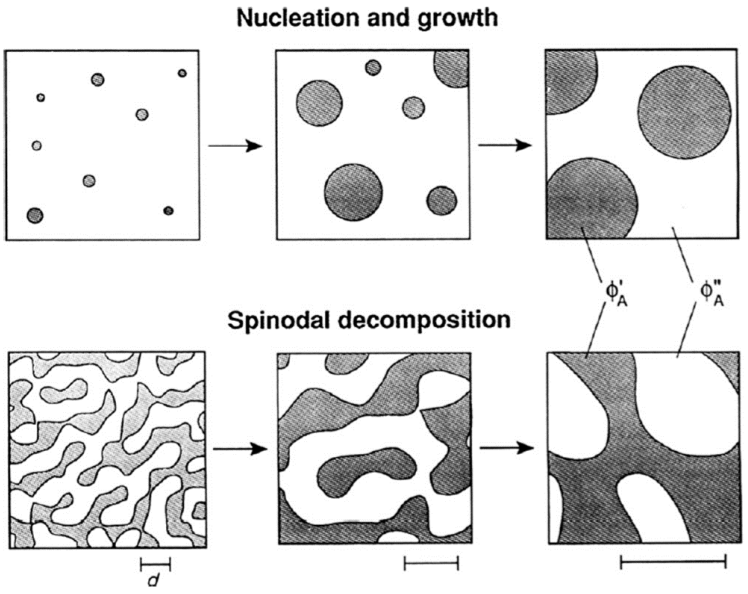

Figure 2. 3. Schematic showing the nucleation and growth, and spinodal decomposition mechanism of the pore formation [80].

NG is the most common mechanism of phase separation in the case of P/NS/S. This is owing to the fact that the critical point is located at the low concentrations of polymer in the liquid-liquid phase, which is not in the working zone in most porous polymer fabrications. The composition path for the Water/THF/PDMS mixture during the phase separation is likely similar to path 1 in Figure 2.2. In the first step of heat treatment, THF evaporated slowly, resulting in a slight increase in PDMS/Water concentration. After reaching the binodal line, phase separation occurs, and the Water/THF droplets are formed in the polymer-rich domain. Continuing the heat treatment at higher temperature causes more solvent and water evaporation, shifting the composition path toward a more polymer concentration.

2.4. Chapter Conclusion

The P/NC/S ternary phase diagram for PDMS polymer was obtained in this chapter. The parameters required for constructing the phase diagram were calculated based on the numerical method and thermodynamics equilibrations. The compositions of PDMS/Water/THF to achieve the uniform solution can be determined based on the developed phase diagram. The critical point was calculated as 8.4% PDMS weight. The region above the CP is related to the polymer-rich zone, and the underneath area is the polymer-lean phase. Because of the low polymer weight at CP, the nucleation and growth (NG) would be the primary mechanism of the phase separation, where the composition slowly passes a line from a homogeneous region to the metastable domain. The results demonstrated in this chapter can be used to understand the ternary formulation that can lead to a homogeneous mixture and the pore morphology based on the mechanical phase separation.

Chapter 3: Fabrication of Porous PDMS Structures with Tunable Properties Induced by Phase Separation Technique

3.1. Introduction

Polydimethylsiloxane (PDMS) is an organic and non-toxic silicon-based elastomer recognized for its outstanding properties, such as mechanical performance, chemical, thermal stability, and biocompatibility. This material has been widely used in various fields, including flexible strain sensors [13, 33], optical applications [81], and biomedical applications [82]. Recently, the fabrication of porous PDMS-based structures has received increasing consideration because of two primary purposes. In the first category, the porous PDMS is beneficial for specific applications, such as oil/water separation [40] or storage [83]. In the second group, by fabrication of the porous structure, the performance of the PDMS-based materials is improved compared to the solid PDMS structures. For example, it has been reported that porous PDMS has higher flexibility compared to bulk, nonporous material [25]. In addition, it has been established that the porous PDMS-based nanocomposites used as strain sensors have higher sensitivity compared to the solid ones [38]. Based on the desired features, structures with different bulk porosity, pore size, and pore morphology can be produced using PDMS as a primary polymer phase.

It is reported in the literature that the pore size distribution and pore morphology of porous polymers are dependent on the manufacturing method and the material used in the fabrication procedure. For example, the concentration and the type of the solvent, non-solvent, and polymer used in the EIPS can change the pore morphology of the composition [84]. It has been shown that

the ambient condition during phase separation, such as air circulation [85] and the rate of solvent removal [86], can also affect the pore morphology. In addition, the mechanical properties of the porous structures are different according to the porosity and the porous network. It is reported that different mechanical performances are desirable for specific applications. For example, more flexibility is required for wearable electronics, while higher stiffness is critical for biomedical engineering. Accordingly, a simple method for creating a porous structure with adjustable features required for different applications is of great importance. It is essential to develop a formulation for designing porous structures with the desired properties, such as pore size and mechanical behavior.

This chapter reports a simple method for synthesizing porous PDMS structures with tunable properties. Polymer solutions with various PDMS, water and THF concentrations are prepared, and the porous media are developed by removing solvent and non-solvent during the stepping heat treatment. The ternary phase diagram of the three-phase system obtained in chapter two is used to explain the composition changes and the phase separation mechanism. The effect of PDMS concentrations and water/THF content on the pore size distribution, mechanical behavior, and porosity of the samples are investigated. Porous PDMS with a wide range of pore size distribution and mechanical properties are fabricated by adjusting the non-solvent/solvent ratio in the developed approach. The optimal manufacturing parameters to achieve the desired properties of the porous structures are evaluated.

3.2. Experimental

3.1.1. Materials

All the materials were used in this study as they were received. As the polymer phase, SYLGARD 184 PDMS (base elastomer and hardener) was purchased from Dow Corning and was considered the polymer phase. Tetrahydrofuran (THF) purchased from Sigma-Aldrich was chosen as the solvent phase. Deionized water (DI-water) was used as the non-solvent phase.

3.1.2. Polymer Solution Preparation

The PDMS polymer solution was prepared by mixing the polymer, solvent, and non-solvent phases with different concentrations. The whole process of the solution preparation and molding is depicted in Figure 3.1. First, water was mixed with the PDMS base elastomer at 1000 RPM using a hot plate and magnetic stirrer bar. THF was added to the system in the next step. The solution was blended until a stable viscous mixture was reached, which can remain stable for several weeks without any phase separation. Before molding, the PDMS curing agent (part B) with the ratio of part A to B (10:1) was added and blended for 20 min using a mechanical shear mixer at 2000 RPM.

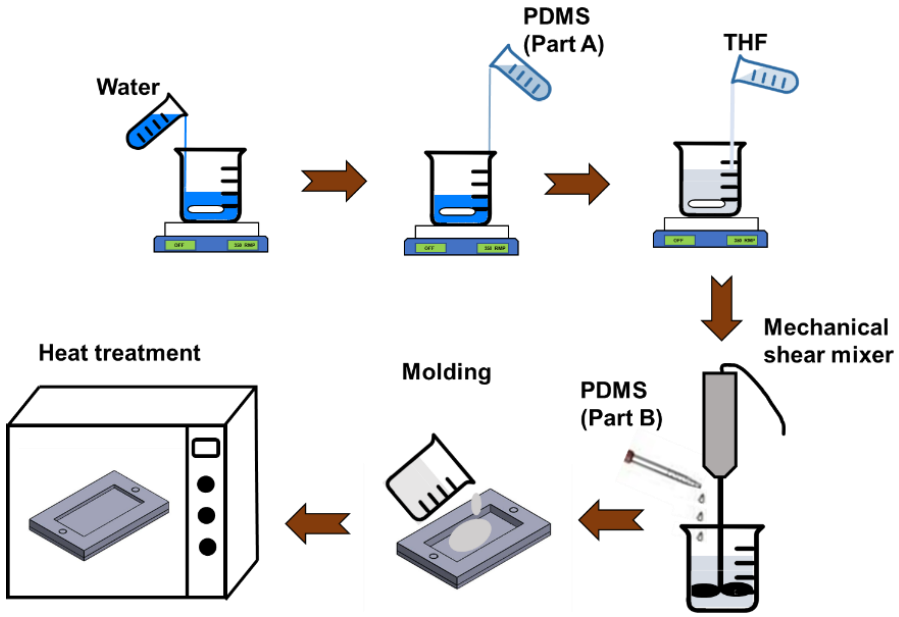

Figure 3. 1. Schematic showing the preparation of polymer solution and molding.

Several formulations were developed in three different categories to explore the effect of different phases in the ternary system on the properties of the porous structure. In the first group, a constant PDMS concentration of 40 wt% was chosen, and the ratio of water to THF (α) was varied from 1 to 8. The effect of nonsolvent/solvent content on the porous structure was investigated in this group. The consistency of the behavior observed in the first group in another polymer concentration was explored in the second experimental group, where the same α but with 60 wt% PDMS was considered. In the third group, multiple PDMS concentrations ranging from 20 wt% to 80 wt% and the constant α=2 were prepared to understand the effect of the polymer phase on the porous network. All the formulations developed for further analysis are listed in Table 3.1.

Table 3. 1. Material formulations of the polymer solution prepared for the experiments.

Category	Case number	PDMS (wt.%)	α
I	1	40	1
	2	40	2
	3	40	3
	4	40	4
	5	40	6
	6	40	8
II	7	60	1
	8	60	2
	9	60	3
	10	60	4
	11	60	6
	12	60	8
III	13	20	2
	14	30	2
	15	40	2
	16	50	2
	17	60	2
	18	70	2
	19	80	2

3.1.2 Porous PDMS Plate Formation

The prepared polymer solution was poured into a customized mold. The mold was prepared in the form of a window frame (170mm ×120mm) using a 1.5 mm thick metal shim. The metal frame was secured on a flat metal surface, and the viscous mixture was then poured inside the mold. The poured material was flattened smoothly using a baking scraper tool. The tool was moved in one direction to minimize entrapped air. Next, the mold was covered using a metal plate and placed inside the oven for solvent evaporation and polymer curing using a stepped heating procedure demonstrated in Table 3.2. During the first step, the oven was heated to 50 ^{o}C for 90 min. THF

started to evaporate slowly and the viscosity of the polymer solution was increased at this step. During the second step, the temperature was raised to 65 ^{o}C (close to THF boiling point of 67 ^{o}C [87]), and all the solvent was evaporated. The phase separation was induced in this step. The sample was kept at 97 ^{o}C for 180 min (close to the boiling point of water) to remove the non-solvent phase (water). Then, the sample was kept at 120 ^{o}C to reach a constant weight to ensure that all the THF/water were evaporated and the PDMS was completely cured.

Table 3. 2. Stepping heat treatment procedure for inducing phase separation.

Step	Temperature (^{o}C)	Time (minute)
1	50	90
2	65	90
3	95	120
4	120	120

3.2. Characterization

After completing the stepping heat treatment procedure, the porous PDMS pates with different pore geometries were obtained. Different characterization was conducted to evaluate the effect of the proposed formulation on the pore formation, including mechanical properties, pore size distribution, and porosity measurement.

3.2.1. Pore Size Characterization

The microscope imaging was performed to determine the pore size distribution and obtain the average pore size of the fabricated samples. Accordingly, the Leica SP8 laser scanning confocal microscope was utilized to take the images. For each case, several microscope images were captured from different locations of multiple samples. The number of pores explored in each sample was different based on the size of the pores. Generally, at least 30 pores were analyzed for each case. The captured images were evaluated using ImageJ open-source software [88]. The area of the pores in the microscope images was obtained. Then, the post-processing analysis was performed to calculate the average equivalent diameter and the standard deviations

3.2.2. Mechanical Properties

The mechanical properties of the porous PDMS plate were explored by performing a tensile test analysis. Dogbone samples following ASTM standard D412 [89] were cut using a designed cutting die and mechanical press from the porous plates. The schematic of the dogbone sample indicating the dimensions is depicted in Figure 3.2a, while the cutting die is shown in Figure 3.2b. The specimens were tested under tensile loading employing a single-column Instron mechanical testing device, and the mechanical properties were extracted.

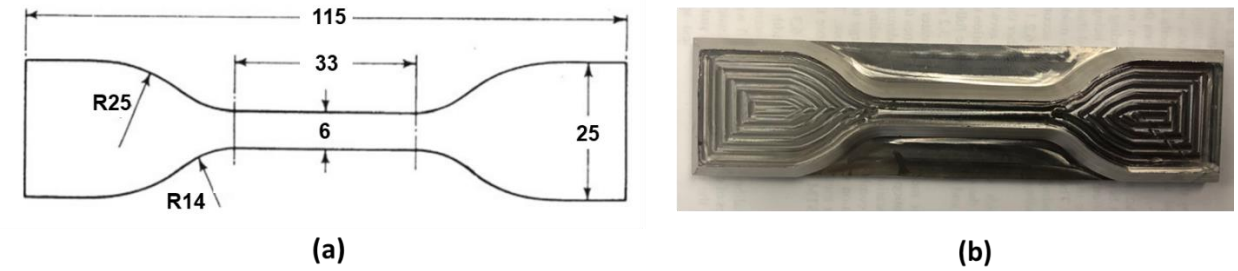

Figure 3. 2. (a) Shape and dimensions of the dogbone sample (dimensions are in mm) and (b) the cutting die designed for the tensile test.

3.2.3. Porosity Measurements

The porous samples' porosity (void fraction) was characterized using an analytical balance and measuring tools. In this regard, the volume of the samples with mass (M), thickness (h), length (l), and width (b) was calculated by measuring the dimensions from multiple points utilizing a digital micrometer (Fowler, "Xtra Value", with 0.001 inch resolution). The porosity (ϕ) of the specimens was determined using Eq. (3.1) [68].

$$\phi = \frac{V_{pores}}{V_{tot}} = 1 - \frac{\rho_{porous}}{\rho_{polymer}} \tag{3.1}$$

where V_{tot} and V_{pores} are the total volumes of the specimens and the volume of the pores, ρ_{porous} is the density of the porous sample calculated from the volume and mass of the specimens, and $\rho_{polymer}$ is the PDMS density obtained using a pycnometer (AccuPyc II 1340, Micromeritics Instrument Corp., GA), respectively.

3.3. Results

Three samples of the 19 prepared Water/THF/PDMS mixture with different formulations were failed to form the porous structure. There was no stable solution in #13, while no pores were created from the homogenous mixture of samples #18 and #19. In order to justify the failure of these points, their formulations are plotted in the ternary diagram shown in Figure 3.3. It is obvious that point #13 with 20%(wt.) PDMS is located in an unstable region and cannot result in a homogeneous solution. In addition, the composition path of points #18 and #19 do not intersect the binodal curve, leads to PDMS solidification without any pore formation.

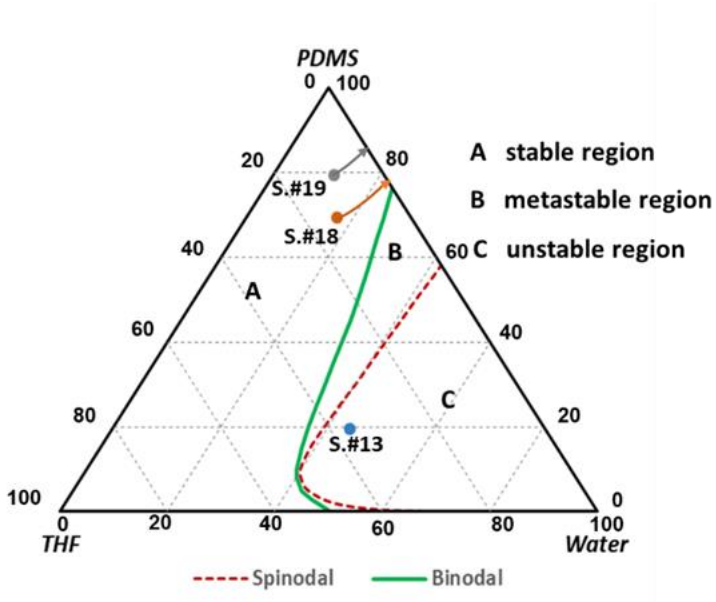

Figure 3. 3. Location of the failed formulation to create porous media on the ternary diagram.

3.3.1. Pore Size Distribution

The microscope images taken from the samples with various formulations for groups 1 and 2 are shown in Figure 3.4 and Figure 3.5, respectively. The pores are circular shapes with dark colors, while the bright continuous area is cured PDMS. It can be seen that NG of the water enriched droplets was the mechanism of the pore formation. The pore formation mechanism can also be explained by the ternary phase diagram (Figure 3.3), as all the formulations used in this study have a polymer concentration far above the critical point (PDMS>8.4%). The droplets were formed in the polymer-rich domain during the phase separation procedure, leading to the isolated porous structure. After coalescence and creating larger droplets, a thin film of PDMS covered the droplets due to the higher surface tension of the water compared to the polymer-rich solution. Then, the water was removed during the heat treatment, resulting in hollow cellular pores in the structure. Based on the microscope images, a higher water/THF ratio caused larger pore sizes in both 40% and 60% PDMS categories. Multiple pores were seen through the thickness for the samples with α=3, 4, 6, and 8, while only one pore was observed through the thickness for the samples with α=1 and 2.

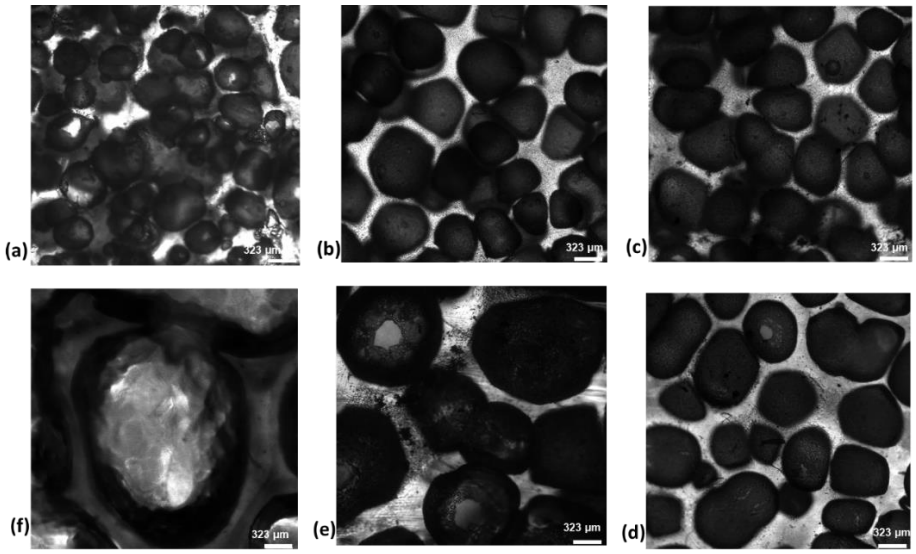

Figure 3. 4. Microscope images showing the pore distribution for the samples containing 40% PDMS with (a) α =8, (b) α =6, (c) α =4, (d) α =3, (e) α =2, and (f) α =1.

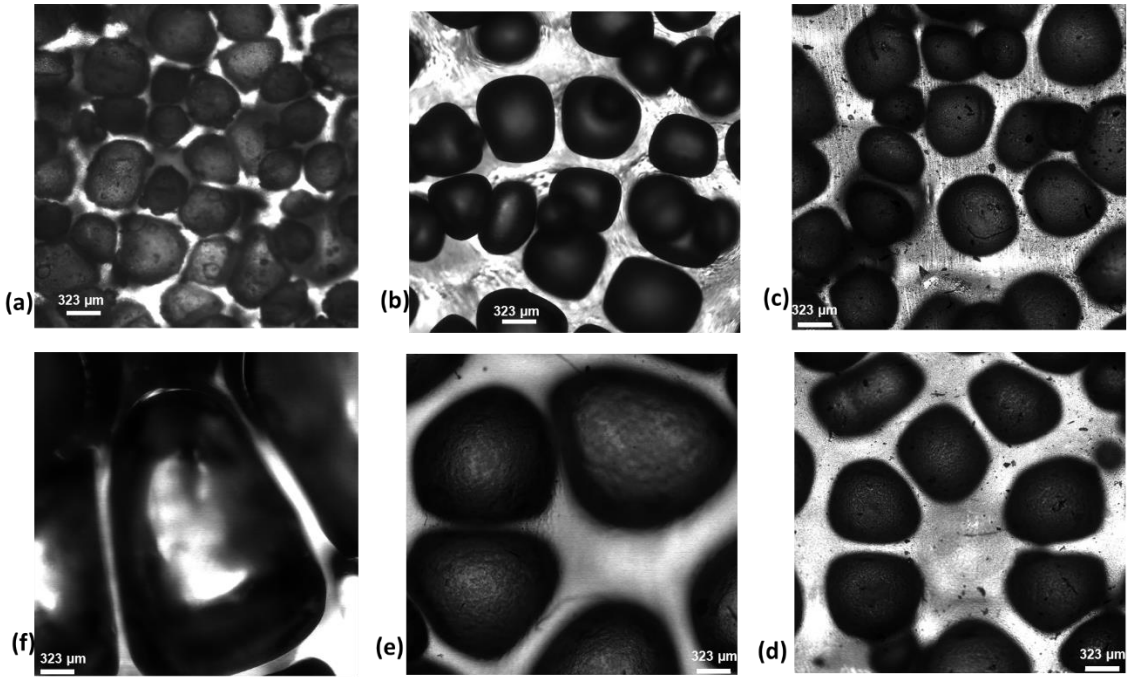

Figure 3. 5. Microscope images showing the pore distribution for the samples containing 60% PDMS with (a) α =8, (b) α =6, (c) α =4, (d) α =3, (e) α =2, and (f) α =1.

It is evident that the cellular pores were originated from the NG of isolated droplets. As expected from the ternary phase diagram, the droplets of Water/THF were dispersed in the polymer-rich domain of the metastable region. These droplets then coalesced and created a larger droplet since the viscosity of the polymer-rich area was not enough in the phase separation step (approximately T=50 ^{o}C). This phenomenon has been reported by other researchers. Bormashenko *et al*. [90] reported the coalescence of the water droplets on the surface of the polymer solution made of chlorinated solvents and amorphous polymers, resulting in a large pore size with a few millimeters diameter. A thin layer of polymer covered the large water droplets, considering the higher surface energy of the water droplets compared to the polymer solution [90]. As a result, the encapsulated water droplets were formed, leading to the isolated close pore structure. The water was evaporated at the last step of heat treatment, causing empty cellular pores in the continuous polymer. In addition, by comparing the empty spaces in Figure 3.4 and Figure 3.5, it can be observed that the pore concentration in 40% PDMS is higher than 60% PDMS, as anticipated.

The captured images were analyzed using the open-source ImageJ software to explore the average pore size in each formulation. The average equivalent diameter ($\bar{d}$) of the pores was calculated as depicted in Figures 3.6a and 3.6b for samples with 40% and 60% PDMS, respectively. It was observed that the pore size was reduced by raising the water/THF ratio for both groups. This phenomenon can be justified by the coalescence of the water droplets in the PDMS domain. The increased amount of solvent in a smaller value of α reduced the viscosity of the solution. Hence, the water droplets had more mobility to coalesce and create larger droplets, leading to larger pore sizes. It should be noted that there was a limitation in increasing the water/THF ratio. Both experiments and the ternary phase diagram showed that the value of $\alpha > 8$ resulted in an unstable mixture.

It should be noted the calculated equivalent pore size for α=1 in both groups was larger than the thickness of the samples (1.5 mm). In fact, the limitation of the thickness restricted the droplets to be formed in the spherical shape, resulting in the growth of the pores in-plane rather than out of plane. As can be observed from the microscope images (Figure 3.4, 3.5), the pore shape for the samples with α=1 was an elliptical shape in both PDMS concentrations. Moreover, the average pore size validates the microscope observation that only one pore can be formed in the thickness for the plates with α=1, 2.

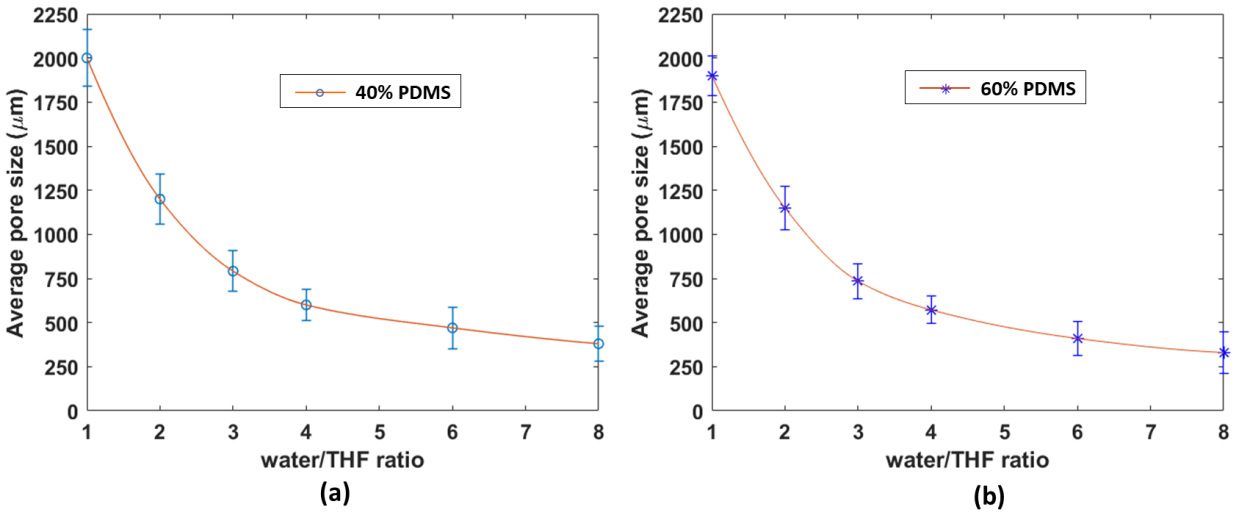

Figure 3. 6. The average pore size obtained for (a) 40% PDMS and (b) 60% PDMS with different Water/THF ratios (the points show the average values, errorbars show the standard deviation, and the lines show the second-order curve fit).

Comparing the results for 40% PDMS (Figure 3.6a) and 60% PDMS (Figure 3.6b), it can be concluded that keeping the Water/THF ratio consistent can result in similar pore sizes in different polymer concentrations. In order to prove this claim, the average pore size for the third group of

the formulation is calculated, as shown in Figure 3.7. Different PDMS concentrations with Water/THF=2 resulted in similar pore sizes. A slight increase in pore size for lower PDMS could be due to the lower viscosity of the mixture compared to higher polymer weight. As examples, the pore size distribution for the 40% PDMS with α=3 and α=4 are shown in Figures 3.8a 4.8b, respectively. It is obvious that droplets with both smaller and larger sizes than the average pore size are available in the structures. Hence, it can be concluded that the water/THF ratio is the parameter controlling the pore size in different polymer concentrations.

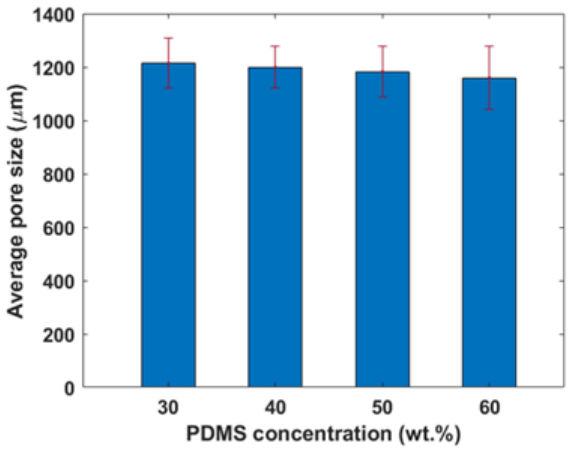

Figure 3. 7. The average pore size for the samples with α=2 and different PDMS concentrations (the errorbars show the standard deviation).

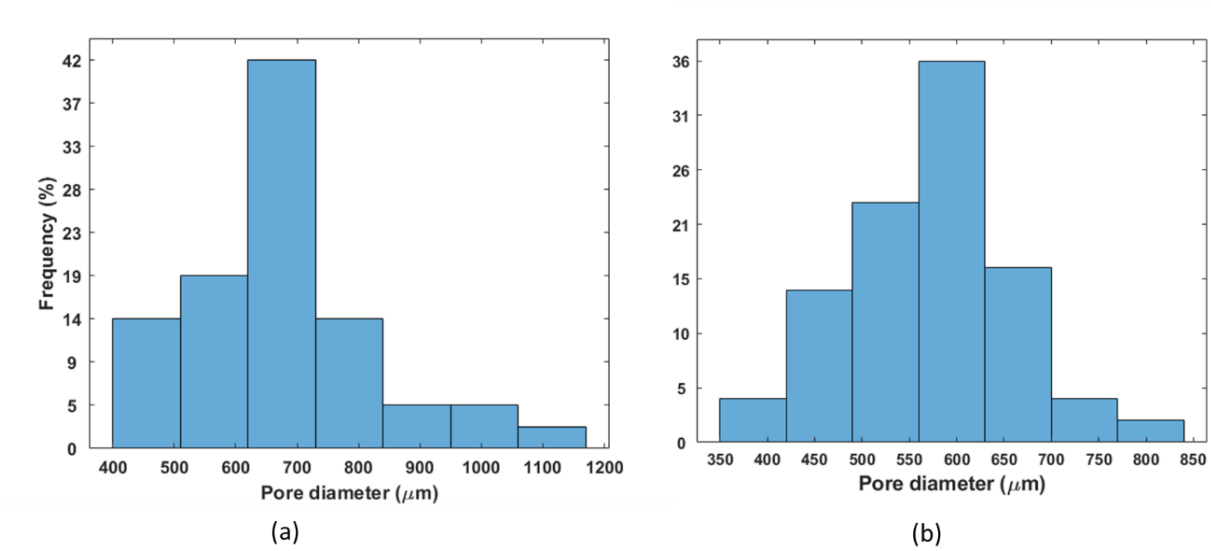

Figure 3. 8. The pore size distribution for samples with 40% PDMS containing (a) α=3 and (b) α=4.

3.3.2. Mechanical Behavior

The dogbone specimens cut from the porous plate were tested under tensile loading. As examples, the figure of the samples with 40% PDMS and α=0, 1, 2, 3, and 4 before the tensile test and the failure mode are illustrated in Figures 3.9(a)-(b), respectively. In addition, the shape of the sample with α=3 at the strain of ε=0% (initial) and ε=60% is depicted in Figure 3.10.

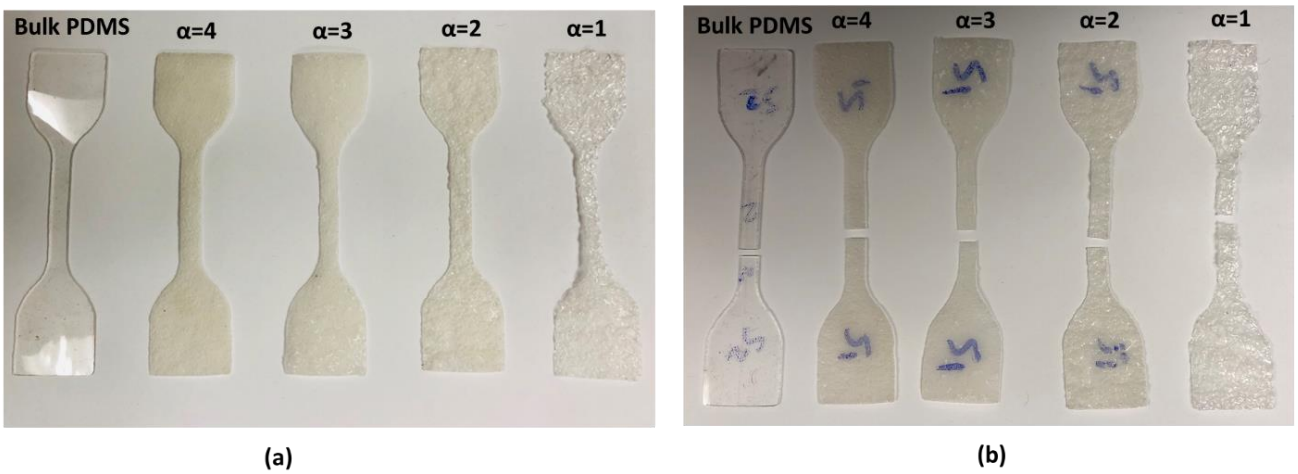

Figure 3. 9. (a) The dogbone samples used for the tensile tests, and (b) failure mode of the tested samples.

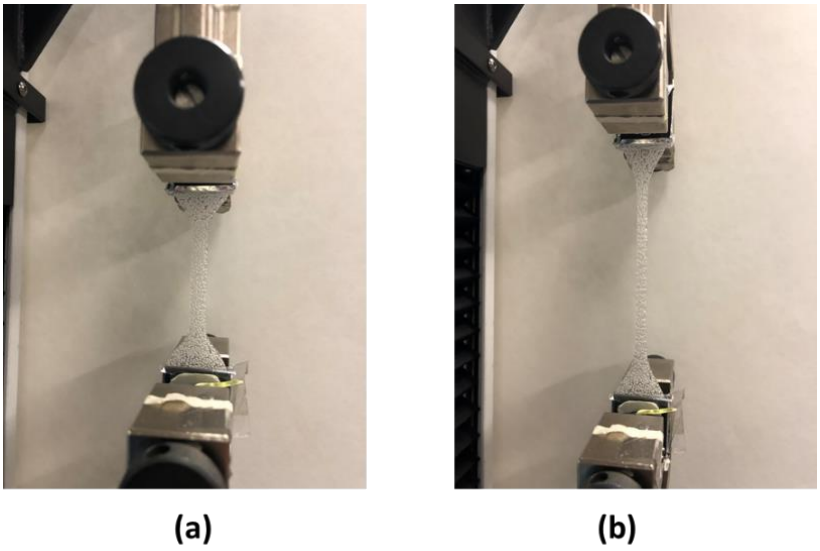

Figure 3. 10. Sample with α=3 (a) at the strain of ε=0% (initial) and (b) at the strain of ε=60%.

The stress-strain curves showing the mechanical performance of the samples with 40% and 60% PDMS concentrations and different α are illustrated in Figures 3.11 a, b, respectively. According to this figure, the porous PDMS samples in both groups became stiffer as the water/THF ratio

increased. Moreover, the 60% PDMS had higher stiffness than the 40% PDMS. The elastic modulus of the samples was calculated from the stress-strain curves. It was observed that for the samples with the same polymer concentration (40% PDMS), a wide range of elastic modulus increasing from 0.49 MPa (α=1) to 1.05 MPa (α=8) was achieved by raising the non-solvent/solvent content.

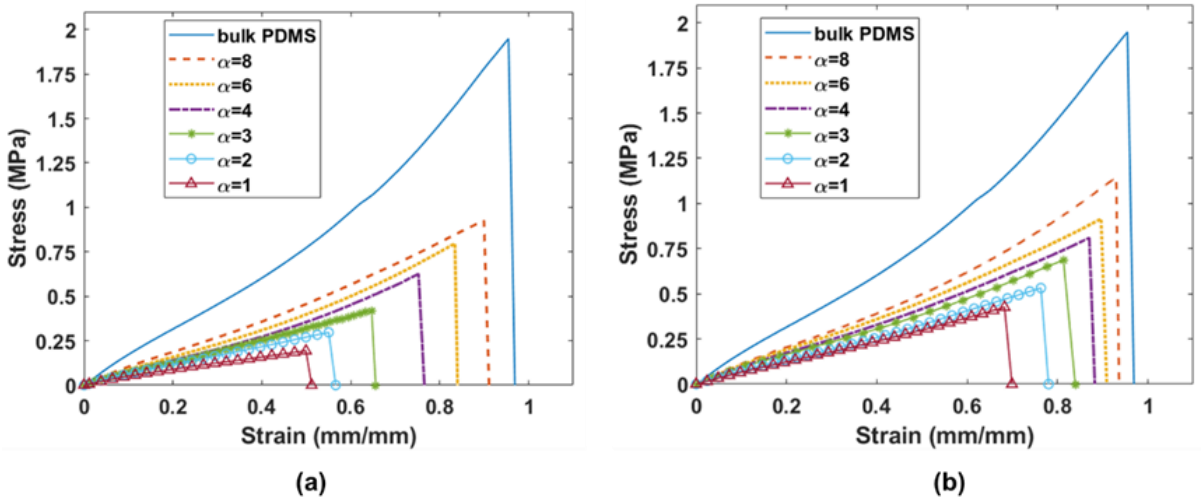

Figure 3. 11. The stress-strain curves for the samples with different α contained (a) 40% and (b) 60% PDMS concentrations.

For better illustration, the related strain of the samples at the stress of 0.18 MPa is depicted in Figure 3.12a for 40% PDMS and Figure 4.12c for 60% PDMS. For both cases, higher deformation in the samples with a lower water/THF ratio (larger pore size) was observed. The related stress of the specimens with 40% and 60% PDMS at the strain of 0.4 mm/mm is shown in Figure 3.12b, d. A higher stress value can be observed for the porous PDMS samples with a smaller pore size (higher water/THF ratio). The stiffness is controlled by the solid phase, which is the pore's wall in

the porous network. The porous structure with smaller pores had a higher ability to sustain the flow stress as the number of pores along the width was improved by increasing the water/THF ratio. In other words, the samples with larger pore sizes showed higher deformation, indicating more flexible behavior than the specimens with small pore sizes.

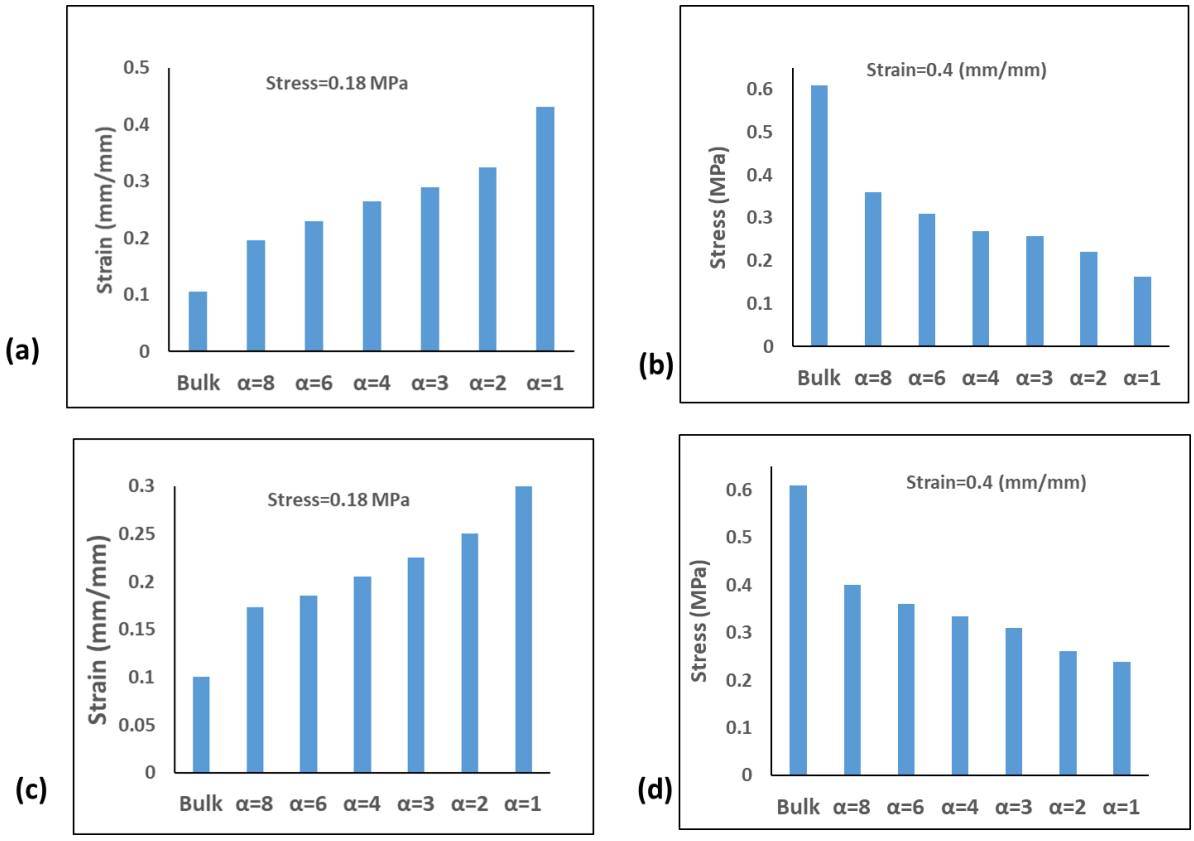

Figure 3. 12. (a) strain for the samples with 40% PDMS 0.18 MPa stress, (b) stress for the samples with 40% PDMS at 0.4 mm/mm strain, (c) strain for the samples with 60% PDMS at 0.18 MPa stress, and (d) stress for the samples with 40% PDMS at 0.4 mm/mm strain.

In order to show the effect of PDMS concentration on the mechanical performance of the porous plate, the stress-strain of specimens with constant α=2 and different PDMS concentrations is displayed in Figure 3.13a. It is evident that the higher PDMS concentration led to higher stiffness.

By comparing the strain of the samples at stress=0.2 MPa in Figure 3.13b, it is revealed that the flexibility of the structure was enhanced by reducing the PDMS concentration. For example, ε= 0.43 mm/mm for the sample with 30% PDMS, which is 34.8% higher than the sample with 60% PDMS. In addition, it is revealed that the strain in the sample with 30% PDMS is 258% higher than the bulk PDMS.

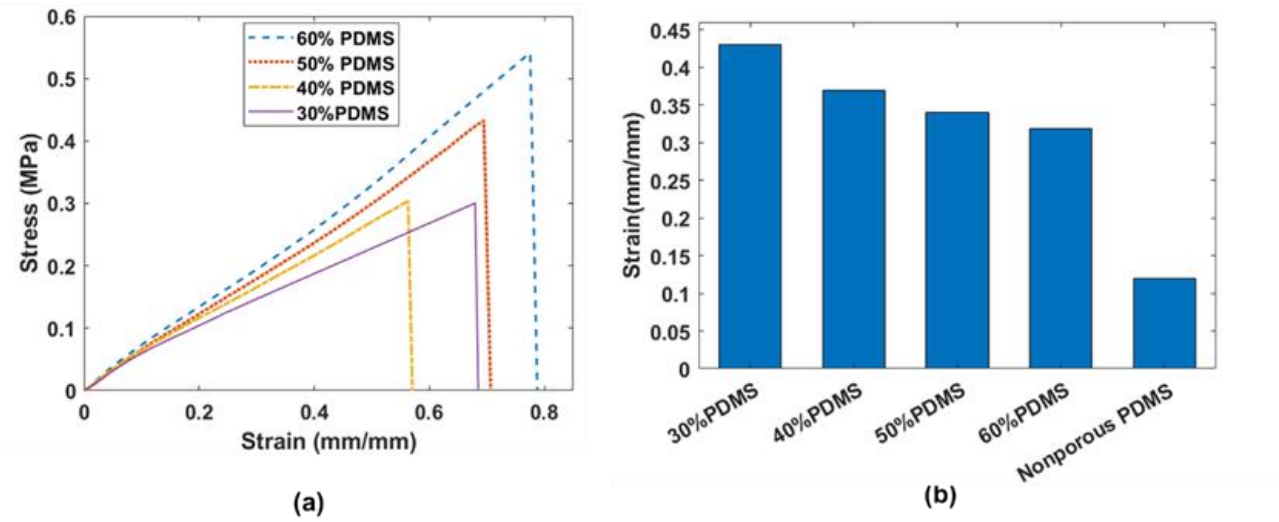

Figure 3. 13. Stress-strain curve for the samples with α=2 and different PDMS concentrations, and (b) comparing the strains for the samples with different PDMS weights at the stress of 0.2 MPa.

.

3.3.3. Porosity Measurements

The porosity was calculated from Eq. (3.1) by measuring the volume and mass of the samples. The obtained results for 40% and 60% PDMS with various Water/THF ratios (α) are depicted in Figure 3.14a. According to this figure, changing the α did not affect the porosity in both groups. It can be

concluded that a larger number of pores were formed in the sample with larger α (smaller pore size), making the void fraction a constant value. As shown in the microscopy images, larger spaces with no pores were seen for the samples with lower PDMS concentrations. This can be verified from Figure 3.14, as the porosity of the samples with 40% PDMS is higher than 60% PDMS. Moreover, the porosity of the fabricated sample with various PDMS loadings is shown in Figure 3. 14b. The calculated porosity was correlated with the amount of nonpolymeric phases used in the mixture. All the nonsolvent plus solvent phases were transformed into the porous network.

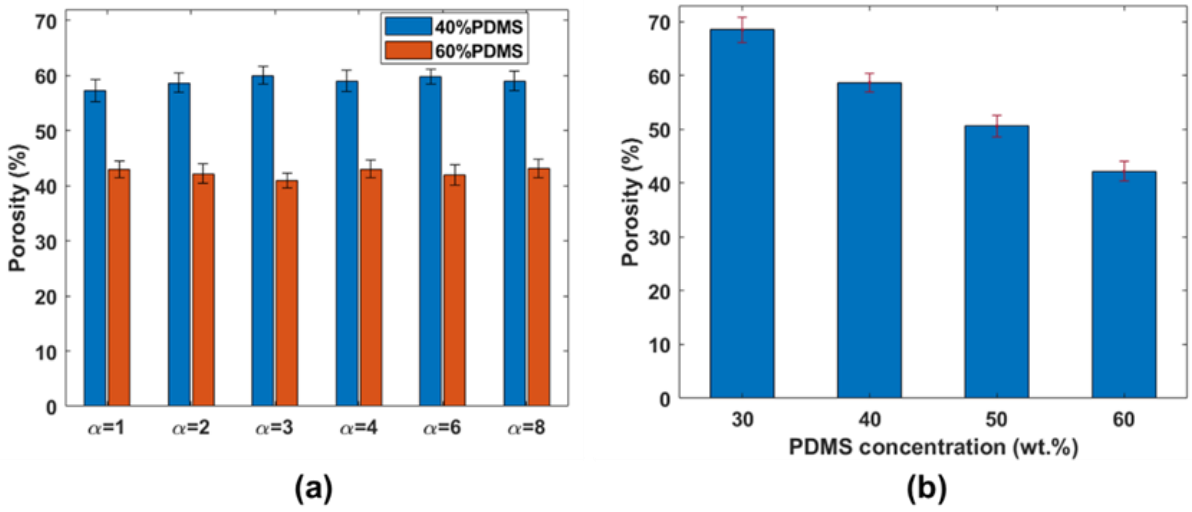

Figure 3. 14. (a) the porosity of the samples with 40% and 60% PDMS and various α, and (b) comparing the porosity of the specimens with α=2 and different PDMS concentrations (the errorbars show the standard deviation).

3.4. Chapter Conclusion

The fabrication and analysis of porous PDMS structures formed by solvent evaporation-induced phase separation were discussed in this paper. Different polymer solutions with various PDMS

concentrations and water/THF ratios were investigated. The analytical ternary phase diagram in the water/ THF/PDMS system was used to determine the stable, unstable, and metastable regions and the binodal, spinodal curves. It was shown that a phase diagram is an effective tool for predicting the stable/unstable formulations and the possible mass transfer path leading to PDMS samples with various porosity levels and pore sizes. The fabricated porous samples were analyzed to evaluate the pore size distribution, mechanical properties, and porosity microstructure. The isolated pores with an average pore size ranging from 330-1900 μm were obtained from nucleation and growth (NG) of the water enriched droplets in the PDMS-rich domain. It was observed that in the formulations with the same PDMS concentration, the average pore size was decreased by raising the water/THF ratio. However, similar pore size was achieved by changing the PDMS concentrations from 30% to 60% and keeping the water/THF ratio fixed.

In addition, the tensile tests of prepared samples revealed that increasing the water/THF ratio at a constant PDMS concentration can increase the stiffness of the porous PDMS structures. The porous structure with smaller pores had a higher ability to sustain the flow stress as the number of cells across the width was improved by increasing the water/THF ratio. In other words, the samples with larger pore sizes showed higher deformation, indicating more flexible behavior than the specimens with small pore sizes. This study showed that a wide range of elastic modulus ranging between 0.49-1.05 MPa could be achieved in the samples with the same density by adjusting the solvent and non-solvent content in the solution. Comparing the samples with different PDMS concentrations and the same water/THF ratio shows that higher polymer weight can increase the stiffness. It was shown that the strain in a sample with 30% PDMS is 34.8% higher than the sample with 60% PDMS and 258% higher than the bulk, nonporous PDMS. Moreover, the porosity of the fabricated structure was evaluated by measuring the void fraction of the samples. It was observed

that higher PDMS concentration leads to lower porosity. The results indicated that the porosity of the samples could be controlled by the polymer concentration, while a negligible effect was observed from changing the non-solvent/solvent ratio.

Chapter 4: Introducing Two-Step Phase Separation Method to Synthesis Hierarchical Porous PDMS Structure with Adjustable Properties

4.1. Introduction

Porous polymer structures have attracted significant attention due to their numerous applications in absorption [91], storage and release [83], and biomedical [92] areas. Compared to other porous polymers, porous PDMS structures have various advantages in various fields [7, 8]. As described in chapter three, the EIPS is one of the most promising methods for creating porous polymers. EIPS has been a reliable approach for fabricating porous polymers with different thicknesses, such as membranes [93] and three-dimensional structures [94]. The NG mechanism mostly leads to a cellular system leading to various cell sizes and morphology dependent on multiple parameters, including polymer and nonsolvent concentrations, type of the solvent, and heat treatment [49, 95].

Mechanical properties of the porous PDMS structure strongly depend on the pore size distribution, which is expected to be tailored for the intended application. For example, a high compliance structure is needed for wearable electronics [38] and tactile pressure sensors [96], while high hysteresis is favorable for energy absorption applications [97]. The effect of density (or porosity) on the mechanical properties of the porous structures has been explored, and some theoretical and empirical models have been developed to predict the elastic modulus of the porous materials and cellular solids [98, 99]. Moreover, several studies have been conducted to evaluate the effect of microstructure on the mechanical properties of porous structures. It was reported that the smaller pore size distribution leads to higher stiffness [100, 101]. In addition, the large pores usually have thinner walls, which are more vulnerable to crack propagation, making the large pore structures

fail at lower strain than those with smaller pores [102]. It was also found that less variation in the pore size leads to higher stiffness [103, 104]. Hence, controlling the pore size and the size distribution is vital for designing a porous structure with desired mechanical properties.

This chapter proposes a two-step phase separation procedure to fabricate porous PDMS structures with tunable microstructures and mechanical properties using a polymer/solvent/nonsolvent solution. Toluene and THF with different mixing ratios are employed as a solvent phase. Due to their difference in boiling points, THF and Toluene are evaporated in two separate steps by applying a stepping heat treatment. The heat treatment procedure enables controlling the size and distribution of the nonsolvent droplets precipitated during the phase separation. Tension tests are employed to evaluate the effect of pore size and pore distribution on the mechanical properties of PDMS sheets. The elastic modulus and its rate dependency, tensile strength, failure strain, and the hysteresis of the PDMS with different pore distributions are compared. An empirical model is also developed to design a porous structure with the desired elastic modulus and mechanical response.

4.2. Experimental Section

4.2.1. Materials

SYLGARD 184 PDMS (base elastomer and curing agent) acquired from Dow Corning was used as a polymer phase. Toluene and Tetrahydrofuran (THF) were purchased from Sigma-Aldrich and mixed with various ratios. These two solvents were chosen for inducing two-step phase separation as they have different boiling points. Deionized (DI) water was selected as the nonsolvent phase. All the materials were used as received in the experiments.

4.2.2. Polymer Solution Preparation

Different formulations were considered for preparing the PDMS solution, focusing on the effect of the solvent phase on the pore morphology of the structures. The polymer, the nonsolvent, and the solvent concentration in all the cases were selected 40 wt%, 48 wt%, and 12 wt%, respectively. It was observed in the previous chapter that this ternary combination is a promising route for creating the porous framework via the phase separation technique [105]. The various THF/Toluene ratio was employed for the solvent phase, resulting in 11 distinct formulations, as shown in Table 4.1. According to this formulation, Solvent=THF+Toluene, and the THF content in the solvent phase (THF/solvent) is changed from 0:10 (pure Toluene) to 10:10 (pure THF).

Table 4. 1. Different ternary formulations are used for creating the ternary PDMS solution.

Sample number	PDMS (%wt)	Water (%wt)	THF (%wt)	Toluene (%wt)	Solvent (%wt)	THF/solvent
1	40	48	0	12	12	0:10 (0%)
2	40	48	1.2	10.8	12	1:10 (10%)
3	40	48	2.4	9.6	12	2:10 (20%)
4	40	48	3.6	8.4	12	3:10 (30%)
5	40	48	4.8	7.2	12	4:10 (40%)
6	40	48	6	6	12	5:10 (50%)
7	40	48	7.2	4.8	12	6:10 (60%)
8	40	48	8.4	3.6	12	7:10 (70%)
9	40	48	9.6	2.4	12	8:10 (80%)
10	40	48	10.8	1.2	12	9:10 (90%)
11	40	48	12	0	12	10:10 (100%)

The polymer solution was prepared by mixing the ternary phases with the following procedure. First, the PDMS base elastomer (part A) was blended with water in a glass container. THF and Toluene with different weight ratios were added slowly to the PDMS/water while the system was mixing. The mixture was mixed at 500 RPM using a magnetic plate and a stirrer bar until the mixture reached a stable and uniform past-like structure.

4.2.3. Fabrication of Porous PDMS Sheets

Porous PDMS sheets were synthesized by the gravity casting of the prepared solution into a mold, followed by inducing the phase separation. The curing agent of the PDMS (part B) was added to the solution with a ratio of 10:1 (part A/part B). The mixture was blended for 5 min using the mechanical shear mixture at 1500 RPM. The solution was then poured into a mold consisting of a rectangular metal shim with an internal dimension of 170 mm ×120 mm × 1.5 mm. The viscous mixture was flattened utilizing the scraper tools to fill the frame uniformly. Next, the mold was covered with a metal plate and placed in the oven for the heat treatment procedure.

The heat treatment was applied in 5 steps under atmospheric pressure to induce the phase separation (in two steps) and remove the nonsolvent phase. The first step was for 30 min at 50 ^{o}C. In this step, soft curing of PDMS was started, the viscosity of the mixture was slightly increased, and the system became ready for phase separation. For the second step, the temperature was raised to 60 ^{o}C, and the sample was kept for 90 min. During this step, evaporation of THF led to the first step of the phase separation. The single-phase system was changed to the polymer-rich (PDMS dominant) and polymer-lean (water dominant) phases. The water droplets were formed by the NG mechanism. The growth and coalescence of the water droplets then resulted in the formation of larger droplets. The oven was heated to 75 ^{o}C for 60 min during the third step to ensure all THF

solvent was evaporated and the system was stabilized. Next, the temperature was raised to 97 ^{o}C for 90 min. In this step, Toluene started to evaporate, leading to the second phase separation. Finally, the temperature was raised to 120 ^{o}C (the fifth and final step) to remove the water droplets. This step was continued until a constant weight of the sample was achieved.

4.3. Characterization

Multiple characterization procedures were utilized to explore the effect of different solvent formulations on the microstructure and the mechanical properties of the cast PDMS sheets.

4.3.1. Pore Size Analysis

SEM images were captured from the internal surface of the porous PDMS. In this regard, a fracture surface of the porous samples was explored utilizing HITACHI TM3000 electron microscope with 15 kV acceleration voltage. Images were taken from different sample locations and processed using ImageJ open-source software to determine the pore size distribution.

4.3.2. Porosity

The porosity of the samples was evaluated by determining the bulk density of the porous samples, as explained in Eq. 3.1.

4.3.3. Mechanical Properties

The effect of the ternary formulations listed in Table 4.1 on the mechanical properties of the porous sheets was evaluated by tensile tests. A mechanical press and a customized cutting die were used to cut dog bone-shaped specimens from the fabricated sheets following the ASTM standard D412 for tensile testing of elastomers [89]. The details of the dog bone sample geometry are depicted in

Figure 4.1(a). The tensile test was carried out on the porous samples by controlling the displacement at different strain rates.

4.4. Results and Discussions

All the formulations described in Table 1 were incorporated, and the porous PDMS sheets with different properties were fabricated. The samples had different pore size distributions leading to distinct coloring ranging from fully transparent for the nonporous solid sample to cloudy, nontransparent for the highly porous sample. As an example, the picture of the solid PDMS dog bone sample (Figure 4.1b) is compared with the porous samples with THF/solvent= 10:10 (Figure 4.1c), 5:10 (Figure 4.1d), and 2:10 (Figure 4.1e). It is clear that the sample color changed from transparent toward milky as the THF/solvent ratio was decreased. This color change is due to the pore size distribution, which is discussed in the following section.

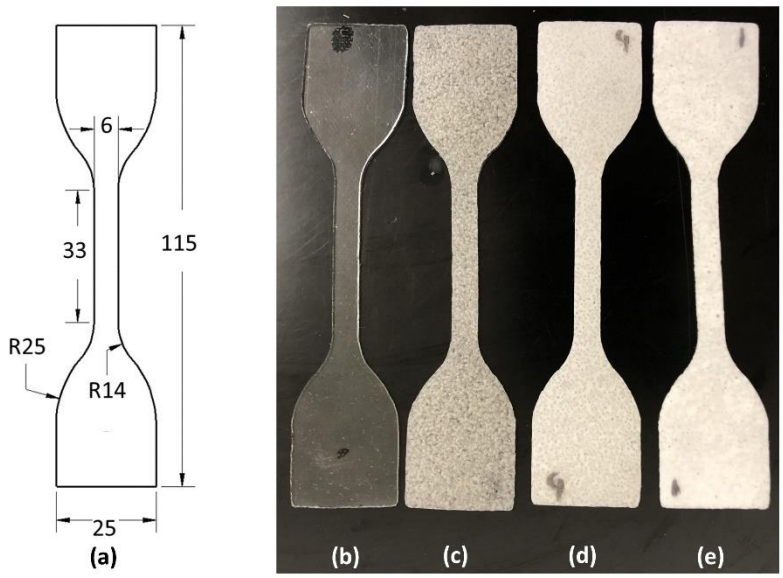

Figure 4. 1. (a) Dimensions of the dog bone sample (dimensions are in mm); (b) nonporous PDMS sample, (c) porous PDMS sample with THF/solvent= 10:10; (d) THF/solvent= 5:10; and (e) THF/solvent= 2:10 for the mechanical testing.

4.4.1. Pore Morphology and Distribution

The SEM images captured from the porous PDMS with different solvent formulations revealed two types of pore morphology. The first group was large pores with fewer numbers, while the second group contained much smaller pores with higher numbers. Figure 4.2a represents a combination of small and large pores in the sample with THF/solvent=3:10. In all the cases, both large and small pores were isolated and elliptical. The small pores filled the area between the large ones, as shown in Figure 4.2b. The distribution of the small pores in a higher magnification SEM image is depicted in Figure 4.2c.

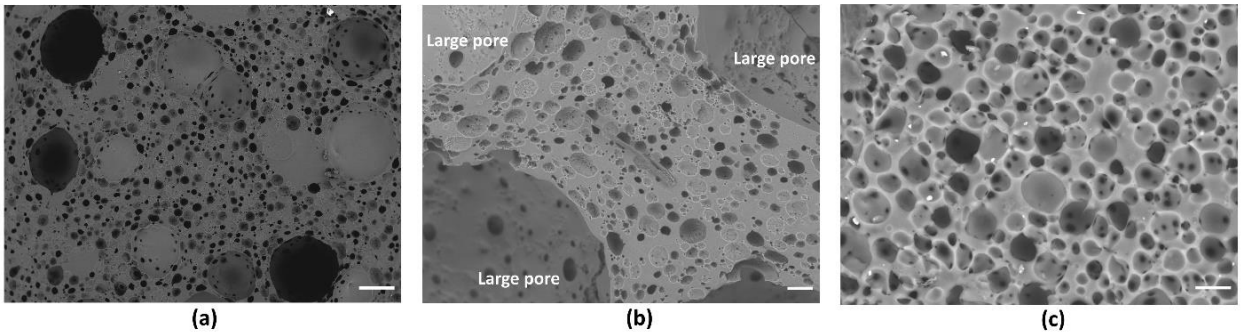

Figure 4. 2. SEM images for the sample prepared with THF/solvent = 3:10 showing (a) combinations of small and large pores in the sample (bar is 300 µm), (b) small pores within the cell edges as well as cell faces of the large pore (bar is 30 µm), and (c) distribution of the small pores (bar is 15 µm).

Statistical analysis was performed on the SEM images of all the samples listed in Table 1 (all the formulations with different THF/solvent ratios) to understand the pore size variations in the structures. The equivalent diameter distribution for the large and small pores within the samples fabricated with different formulations is illustrated in Figures 4.3a and 4.3b, respectively. Based on this figure, the majority (~ 97%) of the small pores were in the range of 7 µm<d_{small}<49 µm, with an average diameter of 28 µm. On the other hand, the average pore diameter of the large pore was 509 µm, while the majority (~95%) of the large pores were in the range of 210 µm<d_{large}<700 µm.

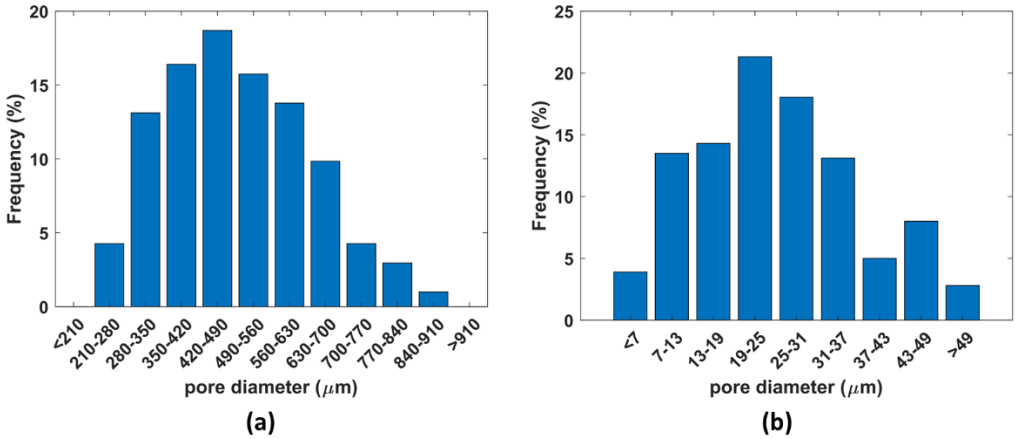

Figure 4. 3. Pore size distribution for (a) large pores and (b) small pores within all the samples fabricated with different formulations.

Comparing the SEM images of the samples with different THF and Toluene formulations revealed that the large pores were dominant in the formulations with a high THF content. On the other hand, the small pores were the majority where Toluene was the dominant solvent. The hybrid pore distribution in which the small pores filled the area between the large ones was the primary pore morphology for the formulations with both THF and Toluene. This trend is clearly observed in Figure 4.4 for the samples with THF/solvent= 0:10 (Figure 4.4a), THF/solvent= 2:10 (Figure 4.4b), THF/solvent= 4:10 (Figure 4.4c), THF/solvent= 6:10 (Figure 4.4d), THF/solvent= 8:10 (Figure 4.4e), and THF/solvent=10:10 (Figure 4.4f). No large pores were observed in the sample with pure Toluene (Figure 4.4a), while all the pores with pure THF were large (Figure 4.4f). The arrows in Figure 4 show the increase in the large pore density while the small pore density decreases from Figure 4.4a to Figure 4.4f as the THF/solvent ratio increases.

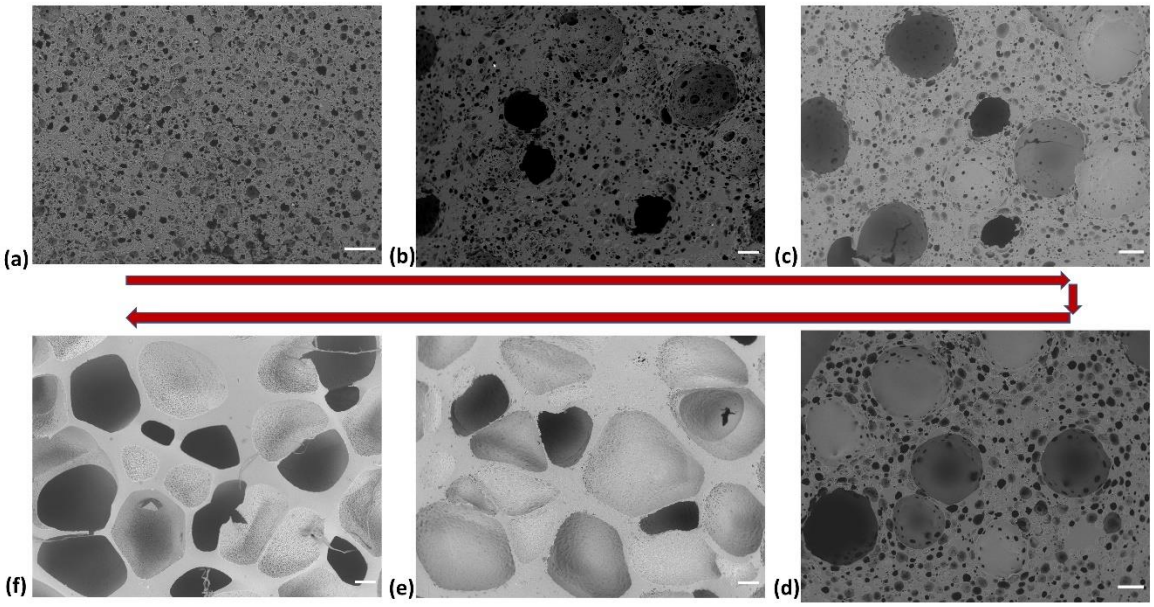

Figure 4. 4. SEM images showing the porous microstructure in the samples with (a) THF/solvent=0:10, (b) THF/solvent=2:10, (c) THF/solvent=4:10, (d) THF/solvent=6:10, (e) THF/solvent=8:10, and (f) THF/solvent=10:10 (scale bar is 200 µm in all images). The arrows from "a" to "f" show the increase in the large pore density and decrease in small pore density as the THF in the solvent is increased.

The formation of the large and small pores depends on the two-step phase separation mechanism that occurred during the multi-step heat treatment. First, evaporation of THF (due to a lower boiling point than Toluene) caused the formation of water precipitation in the form of droplets. Since the PDMS-rich domain is low viscous at this step, the water coalescence resulted in the formation of large pores. With a further increase in temperature, Toluene started to evaporate, leading to the second phase separation. The difference between the size of water droplets formed by evaporation of THF and Toluene is based on the difference in viscosity of the PDMS-rich domain at the time of solvent evaporation. THF evaporated quickly due to the higher volatility and lower boiling temperature when the viscosity of the PDMS was low. Therefore, the created water

droplets could move freely and merge to form super large templates. However, the polymer-rich domain was highly viscous at 97 ^{o}C, preventing the excessive coalescence of the water precipitated by the evaporation of Toluene. This phenomenon resulted in the formation of much smaller pores by the evaporation of Toluene compared to THF.

Different pore morphologies were observed in the samples fabricated with various combinations of THF and Toluene. As is shown in Figure 4.5, there were some windows on the surface of the large pores, which had various concentrations in different solvent formulations. After forming the large water droplets and stabilizing the system during the first step of the phase separation, the PDMS solution film covered the water droplets because of the higher surface tension of water than the PDMS. The window templating was created during the second phase separation when water precipitated from the film covered the large pores. By raising the temperature, the water inside the cells evaporated, resulting in the isolated pores, and the small pores laid on the surface of the large pores created the windows. Figure 4.5 shows that the windows' density in the pores dropped as the Toluene concentration reduced (THF/solvent ratio increased). In other words, the sample with fewer small pores had fewer windows.

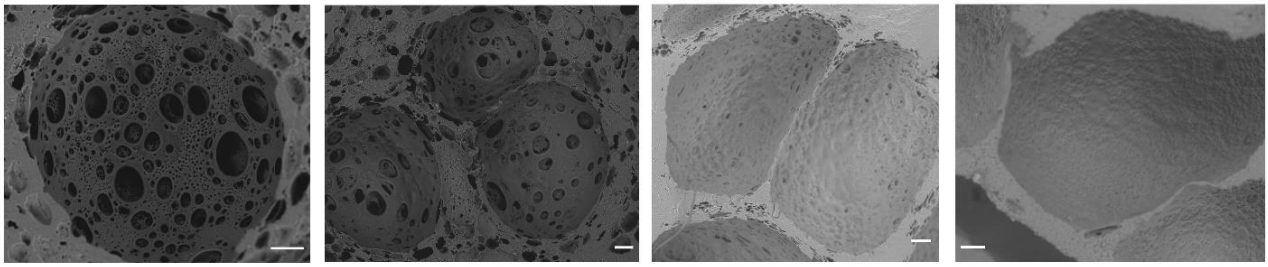

Figure 4. 5. SEM images showing the large pore and windows in the samples with (a) THF/solvent=1:10, (b) THF/solvent=3:10, (c) THF/solvent=7:10, and (d) THF/solvent=9:10, (scale bar is 80 µm in all images).

The relative area fractions of the large pores (ρ_L) with d>200 µm and small pores (ρ_S) were calculated from Eq. (4.1) for the fabricated samples,

$$\rho_L = 100\frac{A_L}{A_L+A_s}, \quad \rho_s = 100\frac{A_s}{A_L+A_s} \tag{4.1}$$

where A_L and A_s are the total area of the large and small pores in the SEM image, respectively. The fraction area of the large pores in the structure as a function of the THF/solvent ratio is depicted in Figure 4.6. It is obvious that ρ_L was increased almost linearly by raising THF content in the system. The relative area fraction of large pores, ρ_L is used as a parameter to present and explain the results in the rest of this article.

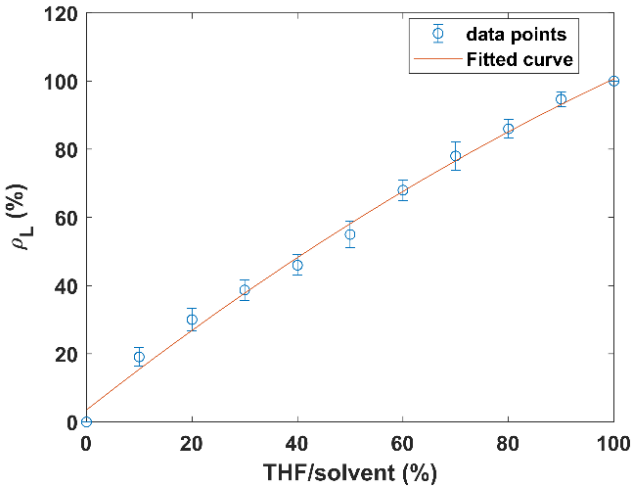

Figure 4. 6. The variation of the relative area fraction of large pores, ρ_L, with an increasing THF/solvent ratio (points show the average value, errorbars show the standard deviation, and the line shows the second order curve fit)

4.4.2. Porosity

The porosity of the samples with different microstructures was measured as depicted in Figure 4.7. This figure shows that the change in ρ_L did not result in any significant changes in the porosity of samples. All the samples had a porosity of around 60%, which is correlated with the polymer concentration (40%) used in the solution. It can be concluded that the porosity was directly related to the polymer concentration and was not affected significantly by the solvent formulation (microstructure). In other words, the pores could be formed in different sizes by adjusting the relative amounts of THF and Toluene, but the total volume fraction of the pores would be the same.

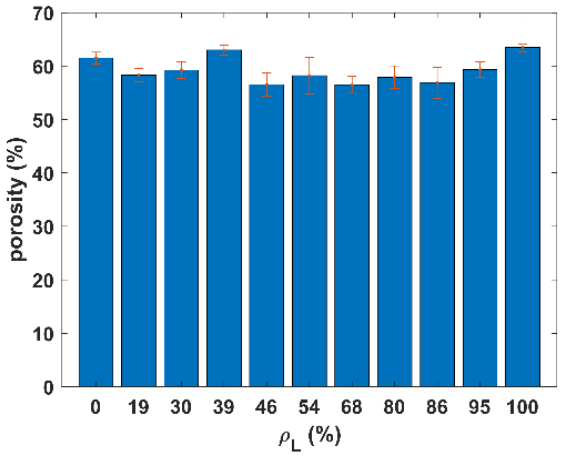

Figure 4. 7. The porosity of the samples with different microstructures fabricated from various solvent formulations (errorbars show the standard deviation).

4.4.3. Mechanical Properties

The mechanical behavior of the dog bone specimens was evaluated under tensile loading. The representative stress-strain curves until the failure point for the samples with ρ_L=0%, 30%, 54%, 86%, and100% are shown in Figure 4.8a. To better illustrate the initial slope of the curves, the stress-strain curve up to the 0.05% strain is depicted in Figure 4.8b. According to this figure, the flexibility of the porous PDMS structures varied dramatically by changing the THF/solvent in the solution. The modulus for the sample with ρ_L=54% (THF/solvent=5:10) was 0.64 MPa, while this value was 0.95 MPa for the specimen with ρ_L=0 (THF/solvent=0:10). The behavior of the solid PDMS under tensile loading is depicted in Figure 4.8c. The obtained value of the solid sample modulus (E_S) was 1.83 MPa. The modulus of the porous structures with different ρ_L was calculated, and the ratio of E/E_S is shown in Figure 4.8d. The elastic modulus was calculated from the linear regression of the linear portion of the stress-strain curve (up to 5% strain). It can be seen that the flexibility of the PDMS elastomer improved significantly as it became porous. The microstructure-

dependent modulus shown in Figure 4.8d can be divided into two regions on the right- and left side of the point with ρ_L=54% (THF/solvent=5:10) point. As shown in Figure 4.8d, the structure became stiffer as the uniformity of the pores increased (more uniform large cell for the ρ_L>54% and more uniform small cell for the ρ_L<54% region). The non-uniform cell structure resulted in more flexible porous PDMS. The microstructure with ρ_L=54% (THF/solvent=5:10) showed the highest variation in the pore distribution and the most flexibility. Based on these results, the flexibility of the porous PDMS sheets at a particular density would be dependent on the process-induced pore morphology, which can be judiciously tailored by controlling the solvent mixture in the solution.

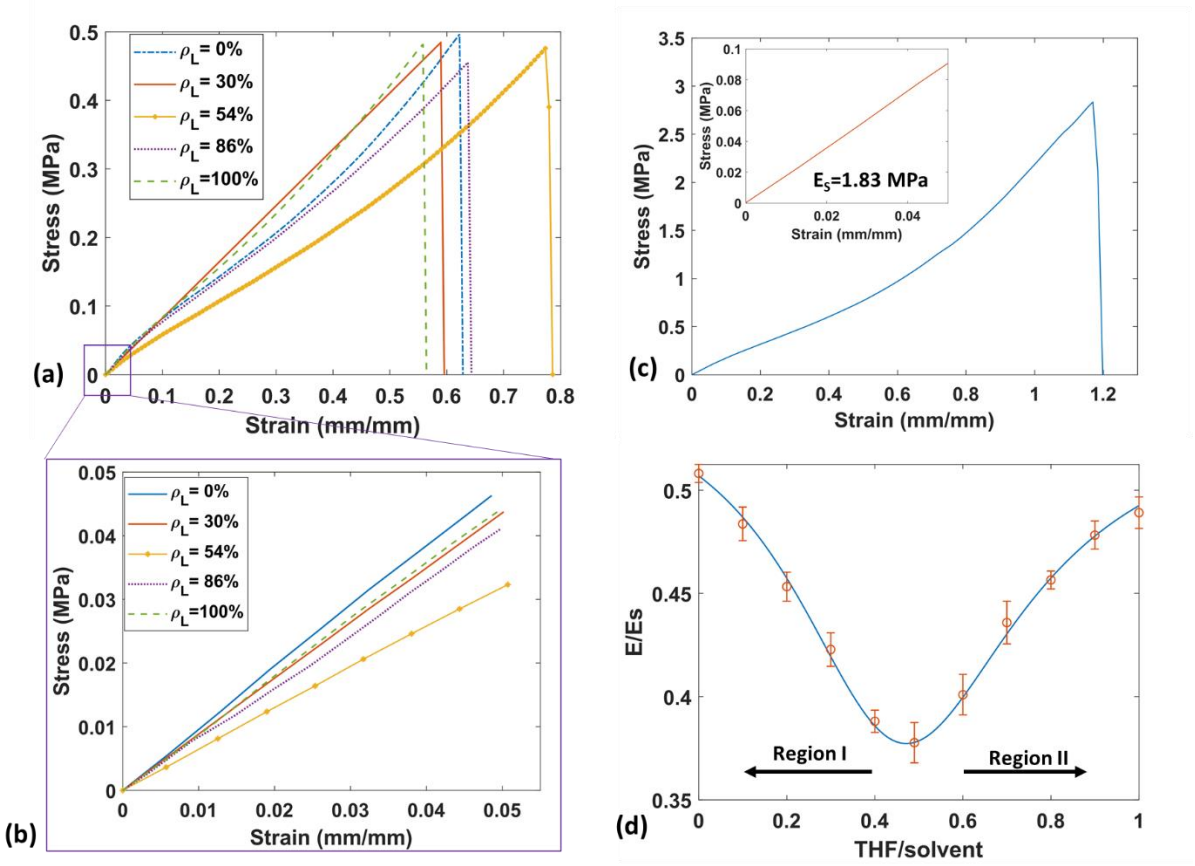

Figure 4. 8. (a, b) Stress-strain curve and their initial region for the porous samples with different microstructures of ρ_L=0% (THF/solvent=0:0), ρ_L=30% (THF/solvent=3:10), ρ_L=54% (THF/solvent=5:10), ρ_L=86% (THF/solvent=8:10), ρ_L=100% (THF/solvent=10:10), (c) the mechanical behavior of solid PDMS, and (d) variation of elastic modulus as a function of ρ_L (points show the average, errorbar show the standard deviation, and the line shows the fitted curve).

The failure strain and strength of the samples based on ρ_L are displayed in Figure 4.9. It can be observed that the strength in all the samples was uniform and close to 0.5 MPa. However, the failure strain varied by the solvent formulation. Accordingly, the lowest failure strain belonged to the sheets with ρ_L =100% (THF/solvent=10:10), while the sample with ρ_L =54% (THF/solvent=5:10) failed at the highest strain. In general, the larger pores have thinner walls leading to easier rapture and earlier failure. For samples with non-uniform cell sizes, disordered

stress distribution and crack propagation occurred, resulting in a higher failure strain. If a large pore failed in these structures, the smaller neighboring cells distributed the stress and delayed the failure.

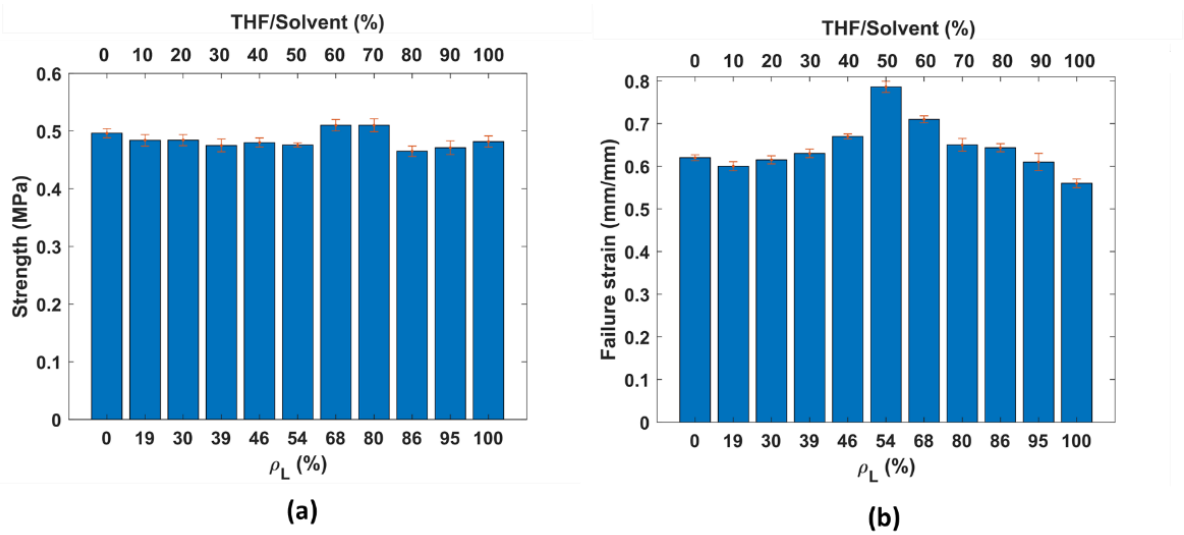

Figure 4. 9. (a) Strength and (b) failure strain of the porous PDMS with different microstructures ranging from ρ_L=0% (THF/solvent=0:0) to ρ_L=100% (THF/solvent=10:10) (errorbars show the standard deviation).

4.4.4. Rate Dependency Analysis

Tensile tests with multiple displacement rates were conducted to understand the rate dependency properties of the fabricated porous samples. The modulus of the dog-bone samples with different THF/solvent ratios subjected to loading rates of 1mm/min, 10mm/min, 25mm/min, 50mm/min, 100 mm/min, 250 mm/min, and 500mm/min was determined. Based on the results depicted in Figure 4.10, the stiffness increased in all the samples as the loading rate was raised, indicating the

loading rate dependency of the modulus. Generally, the elastic modulus at the loading rate of 500 mm/min was about 15-18% higher than the modulus at the rate of 1 mm/min.

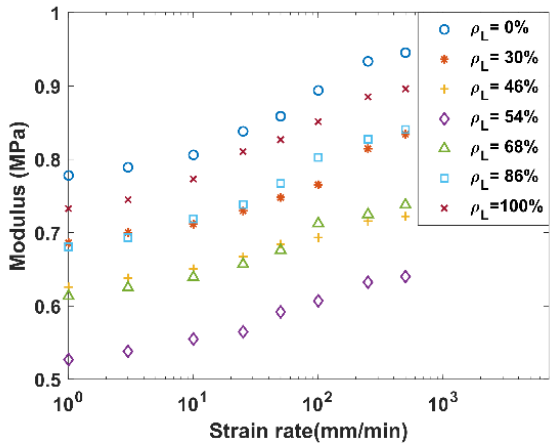

Figure 4. 10. The variation of modulus with changing the loading rate for different porous samples with ρ_L=0% (THF/solvent=0:0), ρ_L=30% (THF/solvent=2:10), ρ_L=46% (THF/solvent=4:10), ρ_L=54% (THF/solvent=5:10), ρ_L=68% (THF/solvent=6:10), ρ_L=86% (THF/solvent=8:10), ρ_L=100% (THF/solvent=10:10).

4.4.5. Hysteresis

To evaluate the energy absorption capacity of the porous PDMS, the tensile loading-unloading cycles up to the maximum strain of ε=10%, 20%, and 30% with multiple loading rates were applied on the dog bone samples. The stress-strain curves during the loading-unloading cycle at the rate of 1mm/min for the solid PDMS samples are compared with the samples with ρ_L =0%, 54%, and 100% in Figure 4.11a. The relative hysteresis is calculated for the samples based on the relationship described in the following equation.

$$Hysteresis\ (\%) = 100 \times \frac{loading\ energy - unloading\ energy}{loading\ energy} \quad (4.2)$$

The loading and unloading energy can be measured as the area under the stress-strain curve during the loading and unloading, respectively. The area under the curve was determined by integrating stress values with respect to the strain values using "trapz" in MATLAB. The calculated hysteresis of the samples is shown in Table 4.2. It can be seen that the energy absorption capacity of the PDMS elastomer improved dramatically by converting it to a porous structure. For instance, the sample's hysteresis with ρ_L =0% at the strain of 0.30mm/mm is 15.95%, which is around seven times the hysteresis of the solid PDMS (2.29%). According to Table 2, the hysteresis of the structures was consistent by changing the applied strain. Moreover, the hysteresis rate dependency was evaluated by applying the loading-unloading cycle up to 30% strain at multiple loading rates. Based on the results displayed in Figure 4.11b, the hysteresis of the porous structures was almost rate-independent, while the hysteresis of the solid PDMS fluctuated by changing the loading rate.

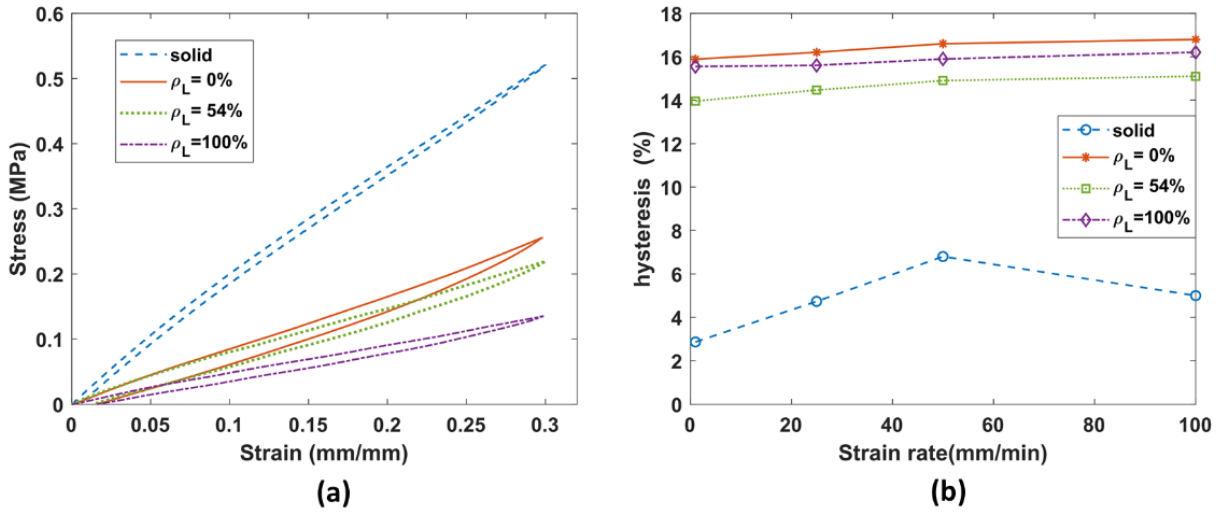

Figure 4. 11. (a) Representative stress-strain curve during the loading-unloading cycle, and (b) the rate-dependency of hysteresis for different samples.

Table 4. 2. Hysteresis (%) in different samples at multiple strains.

Sample	ε=10%	ε=30%	ε=50%
Solid	2.86	2.29	2.38
ρ_L=0%	15.89	15.95	15.97
ρ_L=54.4%	13.96	14.21	14.12
ρ_L=100%	15.55	15.37	15.58

4.7. Empirical Model

It was shown in this study that the pore distribution and the mechanical properties of the porous PDMS can be tuned by adjusting the combination of the solvents in the polymer solution. These properties were illustrated previously as a function of the THF/solvent ratio. It is critical to have a model to estimate the material properties to choose a proper formulation based on the desired properties of the porous PDMS. Considering the elastic modulus of the solid PDMS as E_S=1.84MPa, the following empirical relationship is found by fitting the experimental data displayed in Figure 4.6 for ρ_L, and Figure 4.8d for modulus, respectively. It should be noted that the parameters of THF/solvent and ρ_L are used as a percentage in these equations.

$$\rho_L(\%) = -0.0024\left(\frac{THF}{solvent}(\%)\right)^2 + 1.214\left(\frac{THF}{solvent}(\%)\right) + 3.503 \quad (4.3)$$

$$\frac{E}{E_S} = \frac{0.58\,{\rho_L}^2 - 60.41\rho_L + 2002}{{\rho_L}^2 - 109.4\rho_L + 3888} \quad (4.4)$$

To verify the proposed empirical model, two formulations of THF/solvent=3.5:10 (35%), 6.5:10 (65%) were evaluated. The PDMS solutions were prepared, and the porous sheets were fabricated following the procedure explained before. The dog-bone samples were tested, and the related modulus was calculated. The SEM imaging analysis was performed, and the fraction area of the large pore size (ρ_L) in the samples was determined. The experimentally obtained E and ρ_L were compared with the values calculated from the empirical formulations (Eqs. 4.3-4.4), as given in Table 4.3. According to this table, the predicted modulus and pore distribution of the porous structure is fairly accurate (within 4%).

Table 4. 3. Comparison of modulus and ρ_L calculated from experiments with the empirical model.

THF/Solvent	ρ_L (Eq. 4.3)	ρ_L (Experiment)	E (Eq. 4.4)	E (Experiment)
3.5:10	43.02%	41.59%	0.75MPa	0.72MPa
6.5:10	72.16%	69.68%	0.73MPa	0.70MPa

4.8. Chapter Conclusion

The fabrication and characterizations of porous PDMS with adjustable porosity and mechanical properties were introduced in this chapter. A two-step phase separation technique was developed for inducing the porous structure. Toluene and THF with various mixing ratios were utilized as the

solvent phase in the polymer/solvent/nonsolvent system, while the polymer and nonsolvent content were considered constant parameters. The pore distribution, mechanical properties, and porosity of porous PDMS structures with different formulations were examined. Two distinct pore size distribution was found in the porous network. The pores with an average size of 28 μm were related to the first step of phase separation (THF effect), while evaporation of Toluene resulted in the formation of the pores with an average size of 509 μm. It was found that the microstructure of the porous network changed with THF/Toluene ratio, leading to different pore morphologies and mechanical properties. Accordingly, the large pore concentration increased, and the small pores filling between the large pores decreased by raising the THF/solvent ratio. The porous PDMS density was directly related to the polymer concentration in the solution and independent from the solvent phase (microstructure).

However, the stiffness of the samples was highly affected by the process-induced pore morphology. It was shown that the hybrid-cell structure resulted in higher flexibility compared to the uniform cell structure. For hybrid-cell structure, the sample with THF/solvent=5:10 had the highest flexibility, which was 48% higher than the sample with THF/solvent=0:10. For uniform cell structure, the sample with smaller pores (100% Toluene) was stiffer than the sample with a larger pore size (100% THF). In conclusion, a wide range of PDMS stiffness values can be achieved at a particular porosity level by tuning the mixing ratio of THF/Toluene in the solvent phase. The empirical relationship was also developed based on the experimental data to estimate the elastic modulus and the pore size in the sample fabricated by the proposed formulations. Moreover, by comparing the hysteresis of the porous samples with the solid PDMS, it was demonstrated that the energy storage capability of the PDMS elastomer improved significantly by transforming nonporous PDMS into a porous structure.

Chapter 5: Additive Manufacturing of Porous Conductive Polymer Nanocomposites Developed Using Phase Separation Technique

5.1. Introduction

Highly flexible and electrically conductive polymer nanocomposite (CPNC) sensors have recently attracted significant interest from many fields, including electronic skin [1], biomedical applications [2], health monitoring [3], and body movement detection [4], CPNCs mainly consist of two material groups: conductive nanomaterials, including carbon nanotubes (CNTs) [13], metal nanowires and nanoparticles [10, 11], carbon nanofibers [12]; and flexible polymers such as thermoplastic polyurethane (TPU) [5], Ecoflex [6], and polydimethylsiloxane (PDMS) [33]. Piezoresistive sensors work by converting and detecting a mechanical stimulus to an electrical response. CPNC structures with high flexibility and sensitivity are required for novel sensing applications. Multiple methods have been introduced to increase the sensitivity of the sensors. Micro/nano cracks [34], fracture and bridging [35], and wrinkling of nanomaterial films [36] have been created to enhance the connect/disconnect in the conductive network, which improves the sensitivity. Porous CPNCs have been shown to improve the sensitivity of lightweight sensors by creating new conductive paths in the cells during loading-unloading [37]. In addition to increasing the sensitivity, porous networks enhance the flexibility and compressibility of the structures by providing superior surface areas [5].

Different fabrication techniques have been developed for creating porous CPNCs. Solid templating is one of the most common techniques for developing porous networks using a sacrificial porogen with solid particles, such as salt and sugar [25, 51]. Open-cell structures with a high

interconnection network can be achieved using this technique. However, the fabrication technique is not simple and requires removing the solid templates. Dip coating has been introduced as a simple method for transferring the conductive network into the prepared polymer sponge [52, 53]. Emulsion templating has been used for porous CPNC fabrication by creating water-in-oil emulsion droplets, followed by removing the aqueous phase after polymerization [54, 55]. Porosity can be controlled by adjusting the aqueous phase's volume. But, extra effort is required to remove the surfactant used to form the emulsions as the can sacrifice the structure's mechanical properties. Phase separation is another common fabrication technique for developing porous polymers. A homogeneous polymer solution is transferred into polymer-rich and polymer-lean phases based on the specific method used to induce phase separation. The droplets form and gradually grow, leading to a porous network after removing the secondary phase. The thermally induced phase separation technique has been utilized to fabricate porous TPU nanocomposites [5, 56]. Solvent evaporation-induced phase separation has been used to develop pristine porous polymers [49, 107]. However, little attention has been devoted to the simplicity and ability of this method for creating porous CPNCs for sensing applications.

Most of porous polymer fabrication methods require conventional mold casting techniques [108]. 3D printing is a mold-free novel manufacturing process that attracted significant interest for fabrications of flexible CPNCs [109]. Among 3D printing technologies, direct ink writing (DIW) is a reliable method for depositing a viscoelastic ink layer-by-layer through a nozzle. The ink should have special rheological properties, including shear thinning behavior, yield point, and sufficient storage modulus to have a smooth extrusion, attaining solid-like properties, and retain the deposited shape [62]. DIW has been used in literature for the synthesis of solid PDMS nanocomposites for piezoresistive sensing applications [110, 111]. In addition, 3D structures have

been fabricated using DIW by controlling infill densities and print patterns, leading to printed structural macro-scaled Porosity with applications as flexible sensors [65, 66]. However, DIW of porous structures with 100% infill density and micro-scale pores has been challenging. Despite a few studies in the literature [108, 112], most porous polymer fabrication methods are incompatible with the DIW technique. For example, solid templates such as sugar are likely to be clogged in the fine nozzle or alter the ink rheology, making it non-printable [108]. Dip coating also requires suspending the prepared sponge in a nanoparticle solution, which is not compatible with DIW.

In this chapter, a simple and novel method is introduced for 3D printing of highly flexible porous CPNCs by combining DIW with the solvent evaporation induced phase separation technique. CPNC is prepared by dispersing CNT (as a conductivity/rheological modifier) at various concentrations in PDMS polymer. The ink is then prepared by mixing CPNC, solvent, and nonsolvent phases to achieve a homogenous CPNC solution. 3D structures with 100% infill density are deposited while the micro-scaled porous network is formed after printing during the curing cycle. Specific heat treatment is applied to induce phase separation by solvent evaporation, followed by evaporation of the nonsolvent phase during the curing procedure. The homogeneous template-free ink enables DIW with a wide range of nozzle sizes without any concerns of clogging and reduces manufacturing time-cost, as removing the templates is unnecessary. The piezoresistive behavior of porous CPNC is evaluated to find the optimum CNT concentration that provides the highest sensitivity and flexibility. The sensors made with the optimum formulation are then fully characterized to evaluate the durability and reliability of the 3D printed sample for long-term piezoresistive applications. Finally, the ability of the porous CPNC to detect human motion is explored.

5.2. Experimental Section

5.2.1. Materials

SYLGARD 184 PDMS elastomer kit (base polymer and the curing agent) purchased from Dow Corning was employed as the polymer phase. Heptane purchased from Sigma-Aldrich was used as the solvent phase. Multi-walled CNT with an average diameter and length of 9.5 nm and 1.5 µm, respectively, was acquired from Nanocyl. DI water was utilized as the nonsolvent phase. Tetrahydrofuran purchased from Sigma-Aldrich was employed for dispersion of CNT in PDMS using the solvent-assisted technique.

5.2.2. CPNC Solution Preparation

The schematic of the material preparation and fabrication process is shown in Figure 5.1a. The ink used for the fabrication of porous structures contained CPNC/solvent/nonsolvent ternary phase solution. Bulk CPNC was first prepared by dispersing CNT with different concentrations in the PDMS base elastomer (part A) using the solvent-assisted ultrasonication technique. CNT was mixed with 30 ml THF in a glass container for 5 min using a magnetic stirrer at 350 rpm to wet the CNTs. The mixture was then sonicated for 10 min using a 750W probe sonicator to improve the CNT dispersion in THF. Next, PDMS base elastomer was added and blended with the CNT plus THF for additional 5 min using a magnetic stirrer at 500 rpm. Then, the mixture was sonicated for 30 min to disperse the CNTs in PDMS. The mixture was then placed on a hot plate at 70 ^{o}C while stirring at 150 rpm until all the THF was evaporated. The remaining material contains CPNC with CNT concentrations of 1 wt%, 1.25 wt%, 1.5 wt%, 1.75 wt%, and 2 wt%.

The ternary phase solution was prepared by mixing CPNC, Heptane, and DI-water. The mixing ratio of CPNC/solvent/nonsolvent was chosen as 40 wt%/12 wt%/48 wt%. The feasibility of creating porous PDMS structures based on this formulation was observed in our previous studies.[107, 113] Based on the experimental and analytical analysis, polymer content with at least 30% concentration can control the porosity. Raising the ratio of solvent/nonsolvent can also increase the pore size, while the small ratios can result in an unstable mixture. Hence, 40% concentration polymer and the solvent to the nonsolvent ratio of 1 to 4 were selected for this study. All the components were added to a mixing cup and blended using a planetary centrifugal mixer (Thinky AR-100) until a uniform viscous mixture was achieved. The PDMS curing agent (Part B) was then added with the ratio of Part A: Part B = 10:1 and mixed for another one minute before DIW.

5.2.3. DIW of Porous CPNC

A commercial 3D printer was customized to enable pneumatic DIW functionality. A 3 ml syringe was filled with the prepared ink. The defoaming function of the planetary centrifugal mixer was employed to eliminate the air trapped in the syringe. Dispensing tip needle with 22 gauge was utilized for ink depositing. A circular disc model with a diameter of 12.7 mm and a height of 2.87 mm was designed using SOLIDWORKS software. The model was then converted to a G-code utilizing a combination of Slic3r and Repetier opensource software. DIW was performed at the speed of 5 mm/s. Figure 5.1b demonstrates the DIW of the ink in the shape of a disc. It should be noted that the 3D printability of the prepared inks was evaluated by the rheology experiments, which will be discussed later.

The printed structures were placed in an oven under atmospheric pressure to apply the stepping heat treatment. The first step was heating at 50 ^{o}C for 30 min. The solvent evaporation slowly started, and the viscosity of the mixture was slightly increased at this step. The oven was then heated up and held at 88 ^{o}C for 90 min. Heptane was evaporated at this step which resulted in phase separation. The single-phase mixture was transformed into polymer-rich and polymer-lean phases. The water droplets grew and coalesced to form larger droplets in this step. Next, the sample was kept at 98 ^{o}C for 4 hr to remove the water. Finally, the temperature was increased to 120 ^{o}C to ensure that all the water/Heptane was evaporated and the CPNC was cured completely. The samples were kept at this temperature until a constant weight was achieved. Removing the water droplets from the cured CPNC caused a porous network in the final structure. The shape of the cured sample is shown in Figure 5.1b. Moreover, the ability of the prepared CPNC solution ink for DIW of complex geometries with fine nozzles was verified by printing an "A" letter using a 27 gauge needle, as shown in Figure 5.1c. The homogeneous template-free ink enables DIW with a wide range of nozzle sizes without any clogging issues and reduces manufacturing time-cost, as removing the templates is unnecessary.

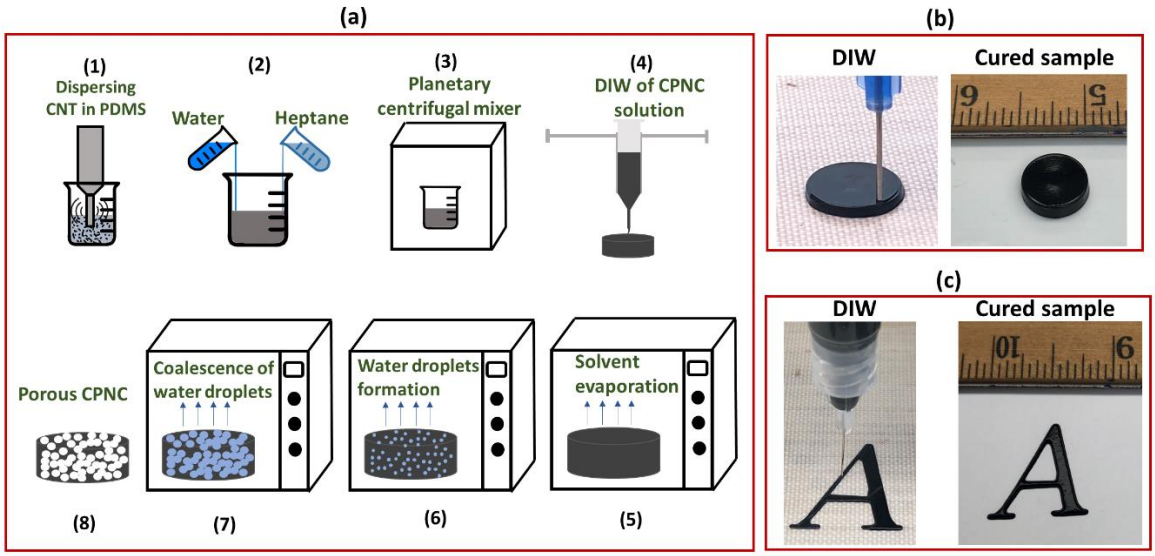

Figure 5. 1. (a) Schematics showing different steps of the preparation, 3D printing, and curing of porous CPNC, (b) DIW of a disc-shaped sensor (with 0.5-inch diameter) and the cured sample, and (c) DIW of complex geometry with fine nozzle (27 gauge) and the cured sample.

5.3. Characterization

5.3.1. Rheology Experiment

The rheological properties of the CPNC solution inks with multiple CNT loadings were evaluated using TA Instruments Discovery HR-2 rheometer. The rheology tests were conducted using a 40 mm diameter cone fixture with a 2^{o} angle. A steady shear flow test was performed at 25 ^{o}C, and the material's viscosity as a function of shear rate was determined. In addition, an amplitude sweep test was conducted to evaluate the yield point of the CPNC inks. Oscillation amplitude with the frequency of 1 Hz and stress starting from 1 Pa with 5 Pa step was applied, and the values of storage modulus and shear modulus were calculated in each step. The amplitude sweep test was stopped after achieving the cross-over point of G' and G'' curves.

5.3.2. Microstructure and Porosity Characterization

The pore morphology of the fabricated samples was characterized using a scanning electron microscope (SEM). HITACHI TM3000 and Zeiss NEON 40 field-emission SEM instruments were employed to capture images from the fabricated samples' internal surface. The surface was sputter-coated before imagining to increase the electrical conductivity and reduce the possible charging effect. The SEM images were characterized using ImageJ opensource software [88] to calculate the average pore size and the pore size distribution. The equivalent diameter calculated from the cell area ($d = (4A \,/\, \pi)^{1/2}$) in the SEM images were considered for the statistical analysis.

The Porosity of the samples was evaluated from the density of the solid and porous CPNCs, as explained in Eq. 3.1.

5.3.3. Mechanical Properties

The mechanical behavior of the porous CPNC samples was investigated under compressive loads. The experiments were conducted using an Instron 3345 single column mechanical test instrument with the compression fixture. The loading-unloading responses of the porous samples with various CNT loadings were determined by applying compression displacement loads with the rate of 2 mm/min. Moreover, the rate-dependency of the fabricated specimens was evaluated by applying loads up to 15 % strain at various strain rates between 0.001-3 s^{-1}.

5.3.4. Conductivity and Piezoresistive Behavior

The electrical conductivity of the porous CPNC samples with multiple CNT concentrations was evaluated. The 3D printed samples were placed between two copper plates attached to the compression fixture and were soldered to wires. The electrical resistance (R) of specimens with

the cross-sectional area of (A) and heigh of (l) was recorded using HIOKI RM3545-02 resistance meter over a minute, and the average conductivity (κ) was calculated as $\kappa=l/RA$.

The piezoresistive response of the printed samples with different CNT loadings was characterized by applying the compressive loads up to various strains ranging from 1% to 40% at the 2mm/min loading rate. Materials were placed between the copper plates attached to the Instron fixture. Each test was performed for 18 compressive loading-unloading cycles while the electrical resistance was measured using the resistance meter. The average relative resistance change ($\Delta R/R$) was calculated for each test as:

$$\frac{\Delta R}{R}(\%) = 100 \times \frac{R-R_o}{R_o} \tag{5.1}$$

where R and R_o are the real-time and initial electrical resistance, respectively. The gauge factor (GF) representing the sensitivity of the samples at each strain (ε) was determined as the ratio of relative resistance change over the applied strain (GF= $\frac{\Delta R/R}{\varepsilon}$).

Further piezoresistive experiments were performed on the CPNC sample with the highest sensitivity to evaluate the capability of the 3D printed porous structure for strain sensing applications. The dependency of the piezoresistive behavior to the loading rate was evaluated by comparing the resistance change of the sample loaded up to 15% strain at different strain rates ranging from 0.001 s^{-1} to 3 s^{-1}. The electrical and mechanical relaxation behavior was also explored by holding the sample at 15% strain for 3 hr while recording the resistance and the stress data. Finally, the long-term piezoresistive response of the fabricated sensor was investigated by tracking

the resistance change of the samples under a fatigue compressive load up to 15% strain at 2 mm/min for 700 cycles.

5.3.5. Sensing Applications

The potential application of the printed porous CPNC as a flexible compression sensor was explored. The 3D printed samples were mounted on a cell phone to detect the human finger stimuli during pressing different buttons. The sensor was placed between two electrodes using copper tapes connected to the resistance meter probes. The piezoresistive signal responded to strain loads when pressing the cell phone's home, turning on/off, and the volume up/down button was determined.

5.4. Results and Discussion

5.4.1. Rheological Properties

There are three main properties required for a viscoelastic ink to be feasible for DIW: the material should show a shear-thinning behavior, the ink should have solid-like properties at low shear stress, and possess a yield point. The results of the steady shear test describing the viscosity of the materials as a function of shear rate are shown in Figure 5.2a. A typical shear thinning behavior was observed for all the CNT concentrations, as the viscosity dropped by increasing the shear rate. Shear-thinning is essential for a smooth DIW to avoid clogging the ink inside the needle during the deposition. The viscosity of the CPNC mixture with different CNT loadings at the shear rate of 1 s^{-1} is compared in Figure 5.2b. The mixture with 1% CNT had the lowest viscosity of 148.7 Pa.s compared with 436.7 Pa.s for the mixture with 2% CNT. As expected, the viscosity of the

CPNC solution was increased by raising the CNT loading due to the reinforcement effect of CNT dispersed in the mixture.

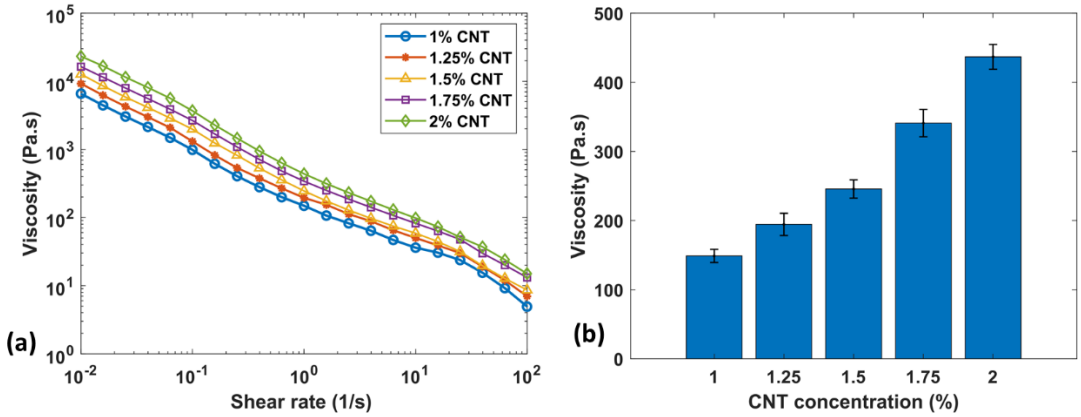

Figure 5. 2. (a) Variation of viscosity as a function of shear rate and (b) viscosity at 1 s^{-1} shear rate for solutions with different CNT concentrations (the errorbars show the standard deviation).

The amplitude sweep test was also conducted to find the possible yield point of the prepared mixtures. The variation of storage modulus (G') and loss modulus (G'') as a function of oscillation stress for the materials with different CNT concentrations were obtained, as illustrated in Figure 5.3a. The solid-like behavior ($G'>G''$) was observed in all the mixtures, which is critical for inks to retain their shape after extrusion and support the materials deposited on the top without spreading. In addition, all the CPNC solutions with different CNT loadings had a yield point at the cross-over of G' and G'' curves ($G'=G''$). The yield point is also essential for DIW applications, indicating the mixture's ability to flow inside the nozzle during printing and return to the solid-like properties to retain the shape after deposition. The yield stress values for the solutions with various CNT loadings are depicted in Figure 5.3b. The yield stress in all the mixtures was larger than 50 Pa, reported as a necessary property for DIW, helping the material return to a solid-like shape after

depositing.[112] The reinforcement capability of CNT resulted in a significant improvement of yield stress by raising the nanomaterials density. The yield stress was 67 Pa for the material with 1% CNT compared with 356 Pa for 2% CNT. A similar effect was observed in Figure 5.3a, as the storage/loss modulus of the mixture increased by raising the CNT loading. The rheological properties of the CPNC solution (shear thinning behavior, sufficient *G'*, and yield stress) indicated the capability of the proposed formulations for DIW applications.

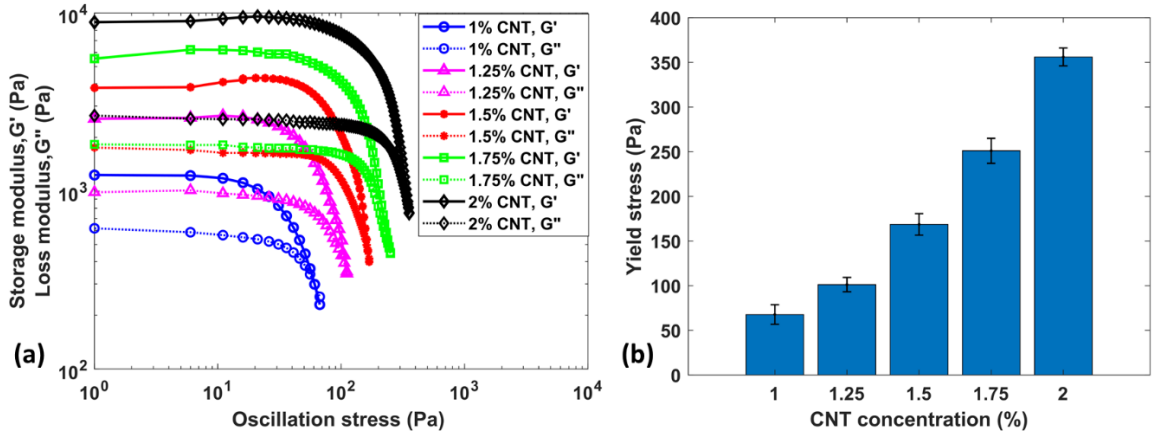

Figure 5. 3. (a) Amplitude sweep test results and (b) yield stress for the mixtures with various CNT concentrations (the errorbars show the standard deviation).

5.4.2. Microstructure and Porosity

Representative SEM images of the 3D printed porous CPNC containing 1% CNT at different magnifications are shown in Figure 5.4. No discernable voids related to air pockets in the sample's internal surface were observed in the low magnification image (Figure 5.4a). This figure indicates that the porous network is formed by the droplets formed during the phase separation and not by the air bubbles trapped during the 3D printing or the solvent/nonsolvent removal. The pores were

uniformly distributed across the sample, as depicted in Figures 5.4a and 5.4b. Water-enrich droplets, formed by nucleation and growth mechanism during the phase separation, caused the cellular structures shown in Figure 5.4b. The joining area of three adjacent cells is illustrated in Figure 5.4c. The SEM image of a cell wall is shown in Figure 5.4d, where some CNTs stick out from the cell wall, and some lay down on the wall, although most of the CNTs were covered by the PDMS polymer.

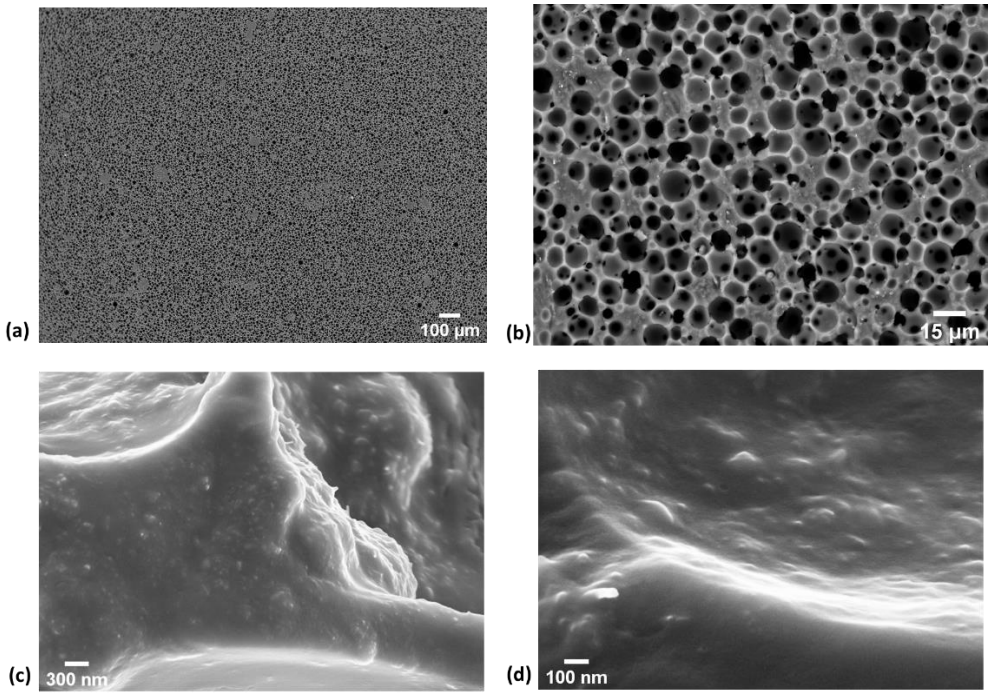

Figure 5. 4. SEM images of the micro-scaled porosity in the CPNC sample with 1% CNT: (a) low magnification image showing no voids or air trapped in the structure during the DIW, (b) pore distribution in the internal face, (c) the joining area of three adjacent cells, and (d) SEM image of a cell wall where some CNTs stick out from the cell wall, and some lay down on the wall.

The image analysis was conducted on the SEM images captured from porous CPNCs with different CNT concentrations. At least 300 pores from different locations of the samples were explored. The pore size distribution for the porous structures with 1% CNT and 2% CNT as representatives are depicted in Figures 5.5a and 5.5b, respectively. The average pore diameter was calculated as shown in Figure 5.5c. Single-mode distribution can be observed in Figures 5.5a and 5.5b with the larger frequency of the pores around the average size. While the average pore diameter for all the samples was between 5.4 µm to 9.9 µm, the pore's size was decreased at a higher CNT concentration. This trend can be attributed to the increased viscosity of the mixtures at higher CNT loading. As explained before, nucleation and growth is the pore formation mechanism in the phase separation technique. The rheological analysis showed that raising the CNT concentration increased the viscosity of the polymer solution. Hence, the higher viscosity can reduce the coalescence of the water droplets formed in the phase separation process, leading to smaller pore sizes.

The porosity of the 3D printed CPNCs with various CNT loadings was determined, as shown in Figure 5.5d. All the fabricated samples had a similar porosity of around 60%. This number correlates well with the initial formulation used for preparing the CPNC solution, indicating that all the solvent/nonsolvent phases were transferred into the porous network. 40% of the ternary mixture was made of CPNC, while the rest was solvent/nonsolvent removed during the heat treatment. The results indicated the ability of the proposed formulation to control the pore size in the structure by adjusting the CNT loading while keeping the porosity constant.

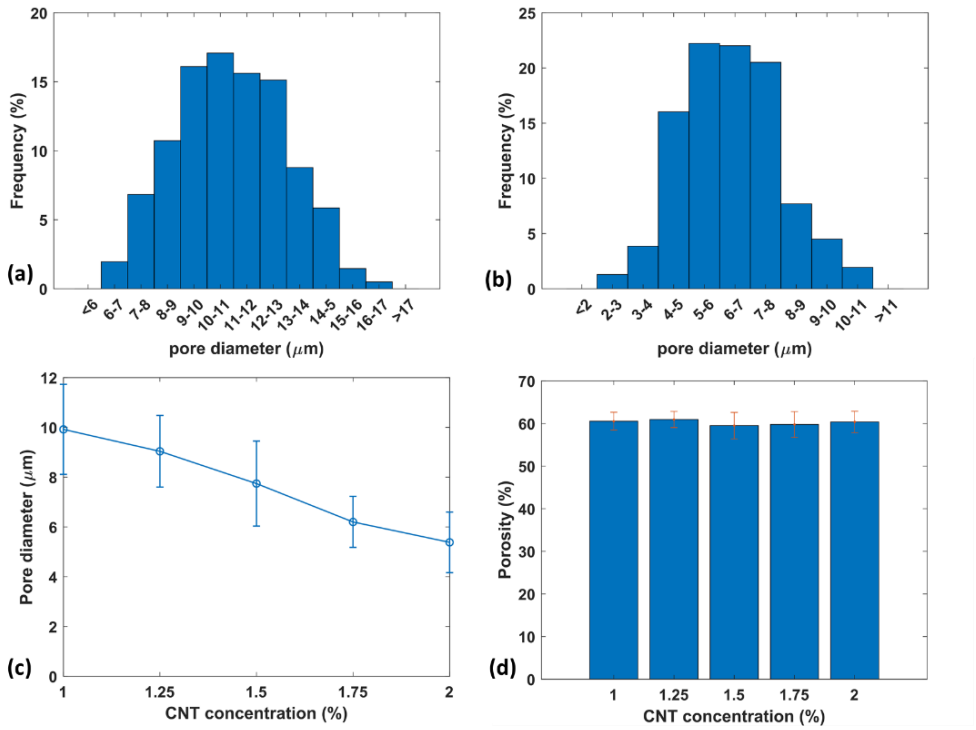

Figure 5. 5. The pore size distribution for the porous structures with (a) 1% CNT and (b) 2% CNT; (c) average pore diameter vs. CNT concentration of the CPNC samples (the points show the average values and the errorbars show the standard deviation), and (d) the porosity in the 3D printed samples with different CNT loadings (the errorbars show the standard deviation).

5.4.3. Mechanical Properties

The mechanical behavior of the 3D printed CPNCs under compressive loading-unloading cycles was determined. The stress-strain responses up to 30% strain are illustrated in Figure 5.6a. The compressive mechanical behavior of the solid sample with 1% CNT is also depicted in Figure 5.6b. As expected, the material's stiffness increased by raising the CNT concentration. However, the stiffness of the porous structures was much smaller than the solid sample, which is desired for strain sensing applications where flexibility is essential. The stress values in the samples at 10% strain were compared, as depicted in Figure 5.6b. Materials with 1% CNT had average stress of

36.7 kPa compared with 49.6 kPa for 2% CNT samples. The stress value was 274 kPa in the 1% CNT solid CPNC at the same strain. Figure 5.6c shows the values of the strain at specific stress of 50 kPa. Based on this figure, the average strain in the sample with 1% CNT was 47.6% higher than 2% CNT and 22.7% higher than samples with 1.5% CNT, indicating enhanced flexibility of the porous structures by reducing the CNT loadings. At this stress, the strain in the 1% CNT solid sample was 2.2%. Comparing the mechanical response between solid and porous structures indicated that 60% porosity developed in the sample had enhanced the flexibility of the structure by 580%, which is preferable for piezoresistive sensing applications. Accordingly, porous CPNC with 1% CNT can be a potential structure for flexible sensing applications requiring higher compliant properties.

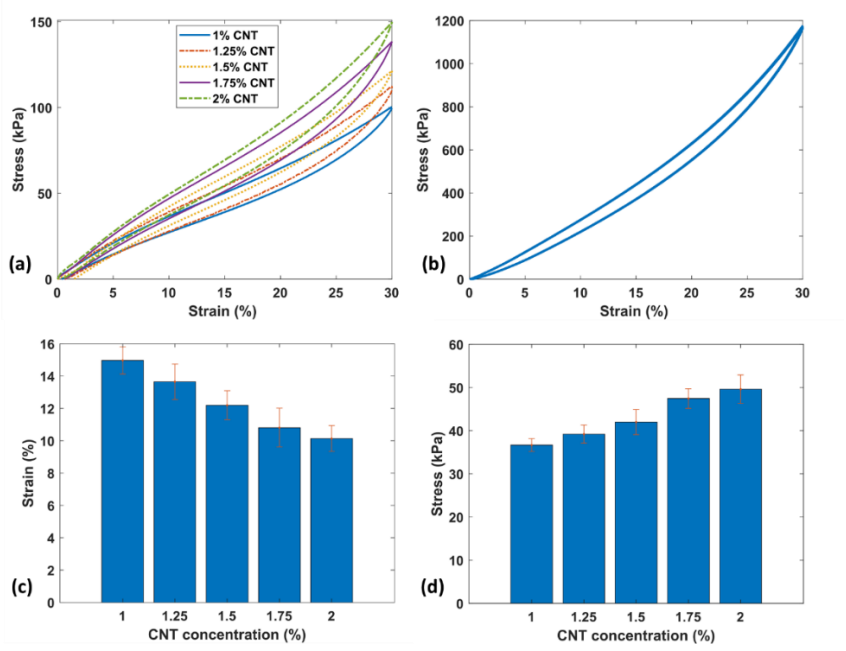

Figure 5. 6. (a) stress-strain curve during the compression loading-unloading of porous samples, (b) stress-strain curve during the compression loading-unloading for 1% CNT solid sample, (c) comparison of stress at the 10% strain, and (d) comparison of strain at the 50 kPa stress for the samples with different CNT concentrations (the errorbars show the standard deviation).

5.4.4. Electrical and Piezoresistive Properties

The electrical conductivity of the samples with various CNT concentrations was calculated, as depicted in Figure 5.7a. The conductivity was increased as the CNT loading raised: the conductivity value was 330.0 μS/cm for 2% CNT, significantly higher than the 1% CNT (2.5 μS/cm). The polymer nanocomposite made with less than 1% CNT content did not show conductive behavior. The trend shows that 1% CNT is closer to the CNT/PDMS percolation threshold, likely resulting in higher piezoresistive sensitivity than the samples with higher CNT loadings.

The piezoresistive behavior of the 3D printed porous CPNCs was evaluated to find the optimum CNT loading resulting in the highest sensitivity. The relative resistance change was obtained for all the samples subjected to the compression loads varying from 1% to 40% strain. The average GF for each test was calculated, and its variation as a function of applied strain is demonstrated in Figure 5.7b. The experiments revealed that the piezoresistive sensitivity dropped as the CNT concentration was increased. The sample with 1% CNT had the highest sensitivity in all the applied strains. The GF at 10% strain was compared among all the CNT loadings, as shown in Figure 5.7c. The sensitivity of 1% CNT with GF of 7.6 was 192% higher than that of the 2% CNT samples with GF of 2.6 at this applied strain. It was also observed that the highest GF occurred at the lowest applied strain. The sensitivity was then reduced nonlinearly and became smooth at the strains higher than 30% for all the samples. For example, the GF at 1% and 40% strain was 19.8 and 2 for the CPNCs with 1% CNT; 9.2 and 1.6 for 1.5% CNT; and 6.8 and 1.1 for 2% CNT, respectively. It is worth noting that the value of the gauge factor in piezoresistive strain sensors depends on multiple parameters, including applied strain, conductive nanomaterial type and concentration, strain/deformation rate, and type of matrix. The typical gauge factor in compression strain sensors

implementing PDMS-based nanocomposite reinforced by carbon-based nanoparticles reported by other researchers is listed in Table 5.1. Within the range of 10% applied strain, the gauge factor in this study is comparable with the literature.

In addition, the piezoresistive behavior of the solid sample (1% CNT) is compared with the porous structures in Figures 5.7b and 5.7c. It was observed that keeping the CNT concentration as 1%, the porous network enhanced the gauge factor of the CPNC from 4.67 to 7.59 (by 62%) at 10% applied strain and from 9 to 19.8 (by 120%) at 1% applied strain. The improvement is associated with the enhancement in the conductive network due to porosity. The CNT located on the pore walls can create new conductive pathways (both tunneling effect and contact resistance) when the pores are compressed during the compressive load, leading to more changes in the electrical resistance than the solid structure.

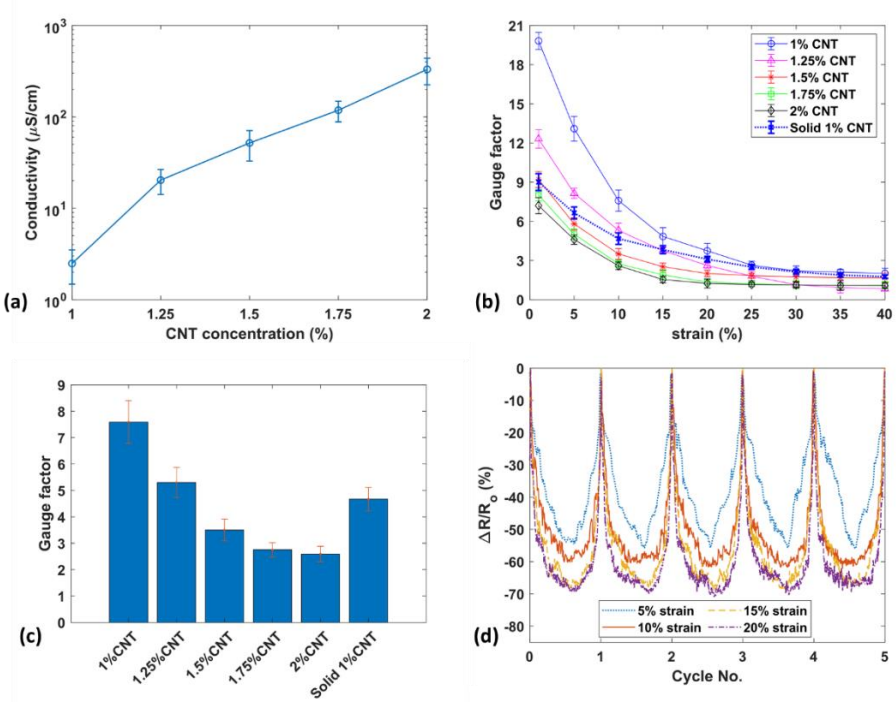

Figure 5. 7. Effect of CNT on (a) conductivity (points show the average values and the errorbars show the standard deviation) and (b) piezoresistive response at different strains of the porous CPNC (points show the average values, the errorbars show the standard deviation); (c) comparing GF at 10% strain for different CNT loadings (the errorbars show the standard deviation); and (d) representative signal response at multiple strains for the sample with 1% CNT.

Table 5. 1. Comparing the sensitivity (gauge factor) of the PDMS-based nanocomposites.

Material	Applied strain (%)	Gauge Factor	Reference
PDMS/CNT	10.0	7.6	This study
PDMS/CNT	10.0	≈ 6.8	[111]
PDMS/Carbon nanofiber	10.0	1.7	[25]
PDMS/Graphene	9.5	8.8	[114]
PDMS/Carbon Black	10.0	1.1	[115]
PDMS/Carbon nanofiber	15.0	3.1	[116]
PDMS/CNT	10.0	≈ 3.0	[117]
PDMS/Carbon nanofiber	10.0	6.4	[51]
PDMS/CNT+SiO_2	10.0	2.0	[9]

Representative sensing responses in five loading-unloading cycles with high repeatability for the sample with 1% CNT under the strains up to 5%, 10%, 15%, and 20% are shown in Figure 5.7d. The negative resistance changes shows that the electrically conductive network was enhanced due to the compressed CNT network caused by the applied load compared to its undeformed state. However, there is a limitation in the conductive network change and thereby the relative resistance change. It has been shown that the tunneling effect between the neighboring CNTs is the dominant piezoresistive behavior for the samples with a low CNT concentration.[118] The tunneling effect reduces if the CNT network gets closer and becomes stable after a threshold distance. Hence, increasing the applied compression load has no further effect on the piezoresistive response. As depicted in Figure 5.7d, the values of the resistance change were similar for the loads higher than 15% strain, and the conductive network reached saturation. Similar behavior was observed for the porous CPNC samples with different CNT loadings, resulting in a nonlinear reduction of GF as a function of strain depicted in Figure 5.7b.

Moreover, the piezoresistive results indicated that 1% CNT resulted in the highest sensitivity with GF of 19.8 at 1% strain compared with other CNT loadings. The tunneling effect is more dominant at 1% CNT, where the conductive networks are farther away than the higher CNT loadings with more conductive pathways. The contact resistance between CNT increased by raising the nanomaterial density, leading to lower sensing sensitivity. There are more changes in the electrical pathways in 1% CNT where there are fewer initial conductive networks than the higher CNT concentrations, enhancing the electrical resistance changes and the sensitivity. Additionally, the mechanical behavior shown in Figure 5.6 demonstrated the highest flexibility of 1% CNT formulation among all the CNT loadings. Hence, the highest sensitivity and flexibility among all the formulations lead to selecting 1% CNT as the optimum formulation for piezoresistive sensing

applications. Further characterizations were conducted on 1% CNT samples to evaluate the reliability of this structure as a flexible strain sensor.

The rate dependency analysis was performed to explore the relationship between the mechanical /piezoresistive properties of the porous CPNC and the strain rate. Cyclic compression loads up to 15% strain at various strain rates were applied on the 3D printed samples while the stress and the resistance were measured. The stress-strain behavior at different strain rates is depicted in Figure 5.8a. The material's stiffness was slightly increased by raising the strain rate and then became stable at strain rates higher than 0.06 s^{-1}. The piezoresistive response of the sample as a function of strain rate is also illustrated in Figure 5.8b. The sensing response was increased from 62% at the rate of 0.001s^{-1} to 66% at 0.006 s^{-1} and then dropped to 62.6% at 0.06 s^{-1} strain rate. A stable trend was observed for the higher strain rates (between 0.06 s^{-1} - 3 s^{-1}). The relative changes in the values of stress and GF at different strain rates compared to the values at 0.001 s^{-1} are shown in Figure 5.8c. It can be seen that the stress was enhanced up to 10% by raising the strain rate from 0.001 s^{-1} to 3 s^{-1}, correlated with the viscoelastic properties of PDMS elastomers. The GF showed a similar rate-dependent behavior up to the strain rate of 0.006 s^{-1} with a 6.7% improvement compared with 0.001 s^{-1}. However, the sensing response was reduced at the higher strain rates. This behavior can be attributed to the ability of the conductive network to respond to the deformation. The conductive network tries to reach equilibrium when the pores collapse. However, in the faster deformation rates, the new conductive network cannot reach equilibrium before starting the new cycle, leading to an incomplete tunneling effect and a slight reduction in the resistance change. Both mechanical and piezoresistive responses of the developed porous CPNC became stable at strain rates higher than 0.06 s^{-1}. In general, the sensor did not lose its sensitivity

by raising the strain rate (all the GF relative changes are positive in Figure 5.8c), indicating the ability to detect stimuli with a wide range of rates.

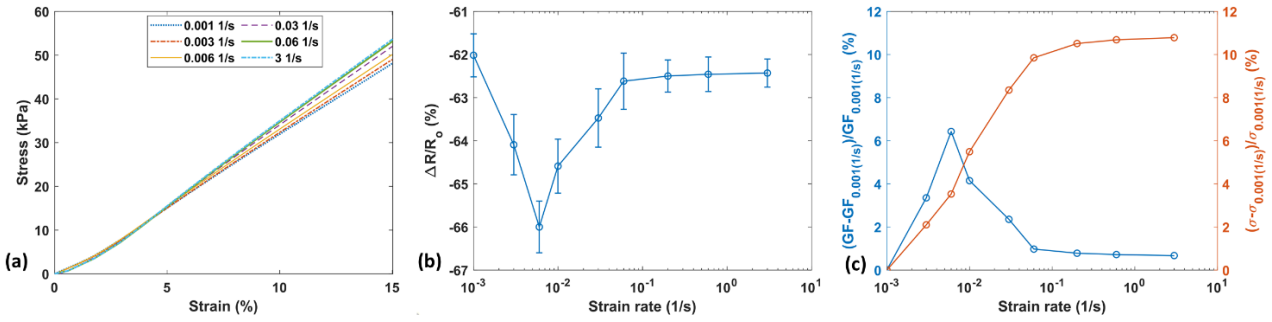

Figure 5. 8. The effect of strain rate on (a) mechanical and (b) piezoresistive response of the CPNC sample under compression load up to 15% strain (points show the average values, the errorbars show the standard deviation), and (c) the relative changes in the values of stress and GF at different strain rates compared to the values at 0.001 s^{-1} (points show the average values, the errorbars show the standard deviation).

The relaxation behavior of the sensor was explored by applying the 15% strain load and holding for 3hrs while recording the sample's resistance and the stress using the resistance meter and the test machine load cell, respectively. The relative changes in the mechanical and piezoresistive response at each time compared with the values at the initial holding time are illustrated in Figure 5.9a. The viscoelastic behavior of the PDMS elastomer-based CPNC resulted in degradation over time in both resistance and stress. The stress and resistance reduction after 3hr were 12.1% and 15.6%, respectively. The majority of the relaxation occurred after a short time and then became smooth, as the stress dropped by 10% and resistance by 14% in the first 20 min. The relaxation in electrical resistance is associated with the changes in the conductive network over time caused by the viscoelastic behavior of the supporting elastomer matrix. Similar behavior has been observed

elsewhere in the conductive polymer nanocomposites indicating that the conductive fillers are well coupled with the polymer matrix [119, 120].

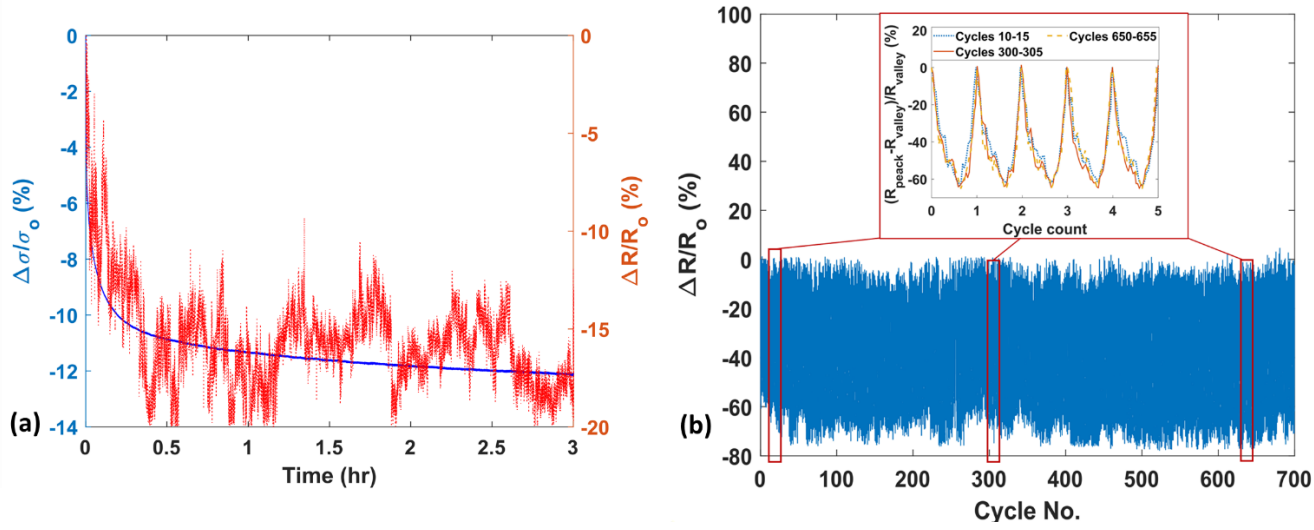

Figure 5. 9. (a) relaxation behavior showing changes in the stress and resistance under 15% strain load for three hr.; and (b) piezoresistive response in the fatigue compression load up to 15% strain for 700 cycles and details of comparing five cycles at three different times in the test.

The durability of the fabricated sensor was investigated under a fatigue compressive load up to 15% strain at 2 mm/min for 700 cycles. The piezoresistive behavior was obtained, as depicted in Figure 5.9b. A slight fluctuation in the sensing response can be observed in this figure. However, this fluctuation occurs in both the peak and valley of the resistance change in each cycle. For better illustration, the peak to valley resistance change for five cycles at three different times in the fatigue test is illustrated: cycles 10-15 (initial), cycles 300-305 (middle), and cycles 650-655 (end). It was observed that the relative resistance change in each cycle was stable during the fatigue test. The results indicated the reliability and the consistent sensitivity of the fabricated sensor in the long-term loading conditions.

5.4.5. Sensing Application

The 3D printed porous CPNCs were mounted on a cell phone to evaluate the potential applications of the structure as a piezoresistive sensor for human motion detection. Three regular cell phone functions were explored: turning off/on by pressing-holding the on/off button for five seconds, turning up/down by pressing-holding the volume up/down button for three seconds, and home screen by pressing-releasing the home button. The picture of sensors mounted on each button and the related sensing response for the mentioned functions are depicted in Figure 5.10. The holding of the on/off button is obvious in Figure 5.10a by the plateau area in each cycle. A shorter plateau area can be seen in Figure 5.10b, as the up/down button was pressed-held for three seconds in this test. Finally, the press-release function of the home button resulted in a faster sensing response with a sharper trend than the previous functions (Figure 5.10c). The developed sensor successfully detected different compression strains performed by human fingers in daily activities. The results indicated the capability of the 3D printed porous CPNC as a flexible piezoresistive sensor with potential biomedical sensors and robotics applications.

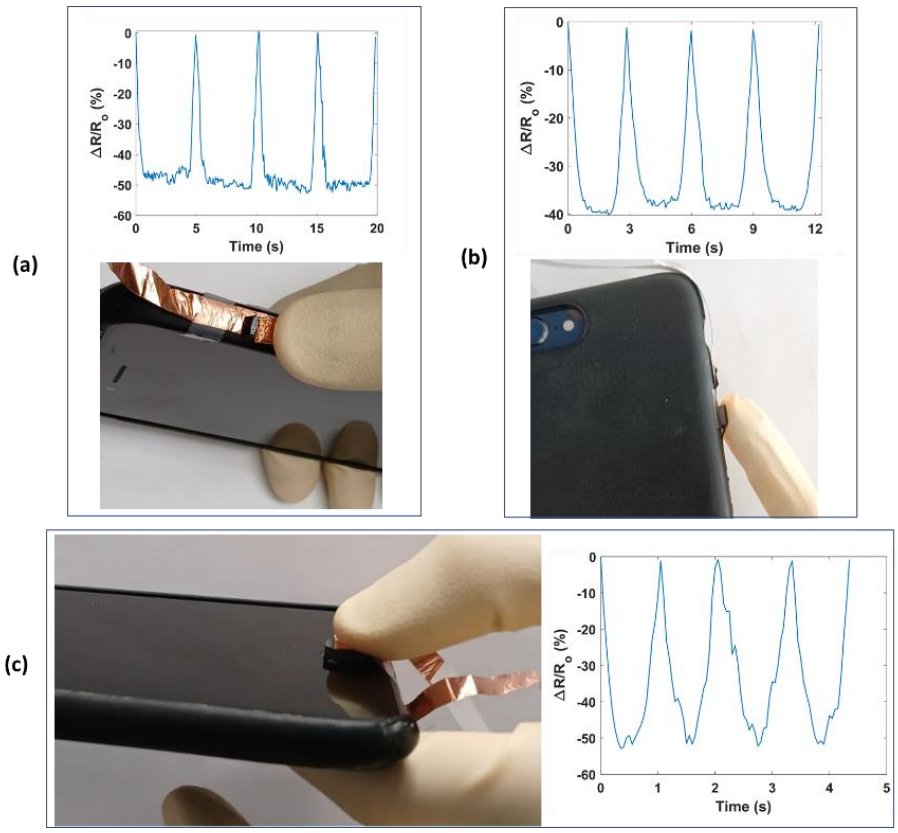

Figure 5. 10. Piezoresistive sensing response of the porous CPNC samples mounted on a cell phone to detect the human motion during (a) press-hold turn off/on button for 5 seconds, (b) press-hold volume up/down button for 3 seconds, and (c) press-release home button.

The ability of the 3D printed porous CPNC to detect small-scale motion and its application as a wearable sensor was also evaluated. The 3D printed porous sensor was employed to detect the human muscle movement during speaking. In this regard, a rectangular sensor with a dimension of 30 mm×7 mm×2 mm was 3D printed adhered to a polyimide tape. The sensor was then attached to the human throat to detect muscle movement during speaking (Figure 5.11a). Three expressions of “Hello”, “Hi”, and “Bye” were pronounced clearly with a regular speaking rate. The sensor’s resistance changes during the speaking were measured with the wires affixed to the sensor and the resistance meter. The resistance was stable during relaxation, but there was a prompt rise when the

operator spoke. As shown in Figure 5.11, distinguished sensing responses were observed with a bimodal resistance change signal when “Hello” was pronounced (Figure 5.11b), a narrow signal when “Hi” was pronounced (Figure 5.11c), and a wider signal when “Bye” was pronounced (Figure 5.11d). The measure resistance change was correlated with the jaw moment and the muscle on the throat during speaking. There are two syllables in “Hello” that causes two jaw movement, leading to a bimodal resistance change signal, compared to a unimodal resistance change signal in “Bye” and “Hi”. It took around 1.46s for the operator to pronounce “Hello” compared with 1s and 0.6s for “Bye” and “Hi”, respectively. Moreover, pronouncing "Bye" requires a wider jaw opening, leading to a higher resistance change than "Hi", as shown in Figure 5.11. The results indicated the ability of the 3D printed CPNC to detect human muscle movement with excellent repeatability and acceptable sensitivity.

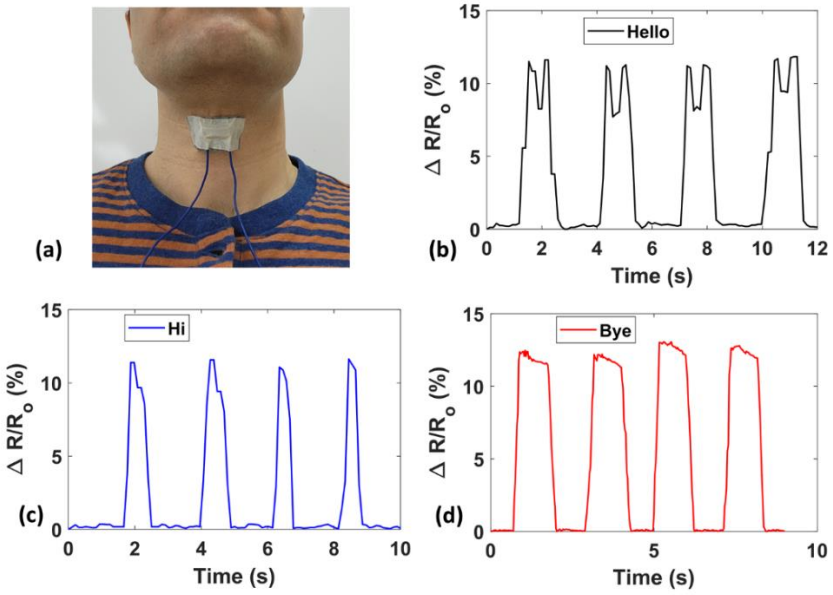

Figure 5. 11. (a) 3D printed CPNC attached on the throat to detect the muscle movement during speaking, (b) sensing response when “Hello” was pronounced, (c) sensing response when “Hi” was pronounced, and (d) sensing response when “Bye” was pronounced.

5.5. Chapter Conclusion

A novel approach was developed in this study for 3D printing of porous CPNCs by combining the DIW method and solvent evaporation induced phase separation technique. The ink was prepared by mixing CNT/PDMS nanocomposite with solvent and nonsolvent phases. Acceptable rheological properties of the ink, including shear thinning behavior, yield stress, and sufficient storage modulus, indicated the printability of the prepared mixtures. Free-standing, disc-shaped piezoresistive sensors were fabricated by deposition of the prepared ink. The micro-scaled porous network was developed during the curing cycle by phase separation followed by the evaporation of the nonsolvent phase. The homogeneous template-free ink has enabled DIW of porous structures with a wide range of nozzle sizes without any clogging, and reduced the manufacturing time and cost as removing a template is not needed [121].

The microstructure of the porous CPNC samples was characterized using SEM, showing the average pore size between 5.4 μm to 9.9 μm in the structures with different formulations. A consistent porosity was observed in the samples fabricated with different CNT loading. The results showed that the pore size distribution can be controlled by adjusting the CNT loading while keeping the porosity constant. Cyclic compression loading-unloading was applied on the samples to evaluate the piezoresistive and mechanical properties of porous CPNCs with different CNT concentrations. The samples with 1% CNT showed the highest sensitivity as high as GF=19.8 (191% higher than 2% CNT) and the highest flexibility (47.6% higher than 2% CNT). In addition, comparing the results of solid material with porous structure shows that the sensor's sensitivity and flexibility were enhanced by 580% and 120%, respectively, with the development of the porous network. A highly repeatable piezoresistive response with a constant GF was observed during the fatigue compression tests for 700 cycles, indicating the reliability of the 3D printed porous sample

in long-term sensing functions. Moreover, the relaxation behavior and the rate dependency of the piezoresistive and mechanical properties of the fabricated samples were characterized. Finally, the application of the 3D printed porous CPNC as a flexible sensor was evaluated by detecting the human motion during pressing/releasing the cell phone buttons in daily activities.

Chapter 6: 3D Printed Highly Porous and Flexible Conductive Polymer Nanocomposites with Dual-Scale Porosity and Piezoresistive Sensing Functions

6.1. Introduction

Highly flexible electrically conductive materials have drawn significant attention due to their promising wearable electronics, health monitoring, and robotics applications. CPNC has recently been implemented as flexible and stretchable/compressible piezoresistive sensors due to the outstanding deformation capability compared with conventional rigid strain sensors. The multifunctional materials used in the strain sensors are prepared by dispersing a conductive nanofiller such as CNTs [33], carbon fibers [12], metal nanowires and nanoparticles [10, 11], and graphene [114] in flexible polymers, including PDMS, Ecoflex [6], and thermoplastic polyurethane [5].

Multiple approaches have been studied for enhancing the sensitivity of the CPNC sensors. The abrupt changes in the conductive network can increase the resistance change during the deformation, leading to high piezoresistive sensitivity. Fracture and bridging in the conductive pathways [35], developed micro/nano scale cracks [34], wrinkled conductive nanomaterial films [36], and developed porous networks [37] have been implemented to increase the resistance change in the CPNC. In addition to the enhanced sensitivity, the porous structures' lightweight, high flexibility, and superior deformation capability have recently attracted interest in novel sensing applications.

Most porous CPNC and even solid strain sensors have been fabricated using conventional molding and casting methods. Additive manufacturing (3D printing) has attracted significant interest recently as a rapid and accurate prototyping technology to fabricate 3D geometries layer-by-layer through a nozzle. Fused deposition modeling is the most common additive manufacturing technique involving the melting and deposition of conductive thermoplastic polymer-based materials [57, 58]. Multiple 3D printing technologies have been introduced for manufacturing of conductive thermoset polymers by deposition of viscoelastic ink, such as aerosol jet printing [59], jet deposition of ink droplets [60], embedded 3D printing [61], and direct ink writing (DIW) [13, 33]. It is reported that DIW can be used for printing 3D geometries if the polymer ink has specific rheological properties. Having solid-like properties at low shear stress with sufficient storage modulus to retain the deposited shape and support the above layers; possessing a yield point to enable flowing during the deposition and getting back to the solid-like properties after deposition, and shear thinning behavior to enable a smooth flow inside the nozzle without choking are the main features of ink for DIW of 3D geometries [62].

Several techniques have been introduced to develop porous CPNC, including solid templating [25, 51], dip-coating method [53], emulsion technique [54], and phase separation [122]. Most of these fabrication processes are not compatible with 3D printing. For example, the solid templates can clog in the fine nozzle during the deposition, or dip coating requires immersing a sponge in the conductive solution. However, the phase separation method can be implemented in DIW since the pore formation is a post-processing step conducted during the heat treatment. As shown in the previous chapter, a polymer solution can be utilized as a viscoelastic ink for DIW of 3D geometries, and microscale pores are developed in the CPNC structures. One of the advantages of 3D printing with less attention in the fabrication of porous strain sensors is the ability to design

structural patterns (e.g., grid, honeycomb, etc.) with adjustable infill densities. These patterns behave as macroscale porosity in the CPNC structures, enhancing the sensors' light-weighting, flexibility, and stretchability/compressibility.

In this chapter, dual-scale porous CPNC is developed by combining phase separation and 3D printing techniques. The objective is to achieve a highly porous and flexible structure without sacrificing the mechanical performance of the structure. The macroscale porosity is established by adjusting infill densities and structural printing patterns, while microscale porosity is developed by EIPS of the deposited ink during the stepping heat treatment. Both macroscale and microscale porosities are controlled, and each effect on the mechanical and piezoresistive response of the CPNC is explored. The printing nozzle size impact on the performance of the piezoresistive sensors is also evaluated.

6.2. Experimental Methods

6.2.1. Materials

The polymer implemented in this study was SYLGARD 184 PDMS elastomer purchased from Dow Corning (both base polymer and the curing agent). Multiwalled CNT acquired from Nanocyl was used as the conductive nanofiller. Tetrahydrofuran (THF), acquired from Sigma Aldrich, was employed to assist CNT dispersion. Heptane purchased from Sigma Aldrich was utilized as the solvent phase, while Deionized water (DI-water) was used as the nonsolvent phase. Water is used in the rest of this paper to call the nonsolvent phase instead of DI water. Aerosil R8200 fumed silica nanoparticle kindly provided by Evonic was employed as the rheology modifier. All the materials were used as they were received.

6.2.2. Ink Preparation

Polymer ternary mixture was used as the ink for DIW. First, CPNC was prepared by dispersing CNT in the PDMS polymer using solvent-assisted sonication. 1% CNT concentration was utilized since it showed the highest sensitivity and flexibility among different CNT loadings, as discussed in the previous chapter. CNT was mixed with 30 ml THF in a glass container using a magnetic stirrer at 350 RPM for 5 min. Next, a 750W probe sonicator was used to disperse the CNT in the solvent for 10 min. Then, PDMS base elastomer (without curing agent) was added to the CNT/THF mixture. Silica nanoparticles with different mixing ratios to polymer were added while the mixture was blended using the magnetic stirrer. After 5 min, the mixture was sonicated for another 30 min, so the CNT and silica dispersed in the PDMS polymer. Next, the mixture was placed on a hot plate at 75 ^{o}C until all the THF was evaporated.

Next, the ternary polymer solution was prepared by mixing CPNC, nonsolvent, and solvent phases. Based on our previous study, PDMS loading up to 70% can be mixed with water and Heptane with the nonsolvent/solvent ratio of 4/1 to form a uniform composition, leading to porous PDMS structure by inducing the phase separation [101]. Hence, CPNC prepared previously with different loadings was blended with Heptane and water using a planetary centrifugal mixer (Thinky AR-100) until a uniform viscous black mixture was reached. The PDMS curing agent with the ratio of base to hardener of 10:1 suggested by the manufacturer was added. The final product was used as the conductive ink for DIW of the porous CPNC structures.

6.2.3. DIW of Dual-Scale Porous Structure

3D cubic shape models with 13 mm × 13 mm× 3 mm were created using SOLIDWORKS software. The models were converted into a G-code for 3D printing utilizing the combinations of Repetier

and Slic3r opensource software. Macroscale porosity was developed by designing structural printing patterns. Grid patterns with different infill densities ranging from 30% to 50% were generated. A commercial 3D printer was modified to operate with pneumatic DIW functions. The prepared ink was loaded into a 3ml syringe capped with different needle sizes ranging from 22 to 27 gauge (0.41 mm, 0.33 mm, 0.26 mm, and 0.21 mm). The defoaming function of the planetary centrifugal mixer was implemented to remove the air trapped in the syringe before deposition. The printing speed of 5 mm/s was considered for DIW.

Specific heat treatment was implemented to induce phase separation and develop the structure's microscale porosity. The 3D printed samples were placed in an atmospheric pressure oven under a three-step heating procedure. First, the oven was set at 75 ^{o}C (below the Heptane boiling point) for 15 min for equilibration. The temperature was then raised to 85 ^{o}C and held for 90 min. The solvent evaporated, inducing the phase separation at this step. The water-enriched droplets form and grow with nucleation and growth mechanics to the larger droplets. The uniform polymer solution was transformed into polymer-rich and polymer-lean domains. Next, the oven was heated up to 97 ^{o}C (close to the nonsolvent boiling point) and held for 5 hr. The water droplets were removed from the structure at this step. Finally, the sample was kept at 120 ^{o}C until a uniform weight was achieved. All the solvent/nonsolvent were removed, and the polymer was completely cured, leading to porous CPNC with dual-scale porosity. Different steps in material preparation, 3D printing, and heat treatment are illustrated in Figure 6.1a schematically. The snapshot of a sample during 3D printing and the cured sample after the heat treatment is shown in Figure 6.1b. The dual-scale porous CPNC was highly flexible and deformable. As depicted in Figure 6.1c, the sample can be squeezed by a finger and released to the original shape.

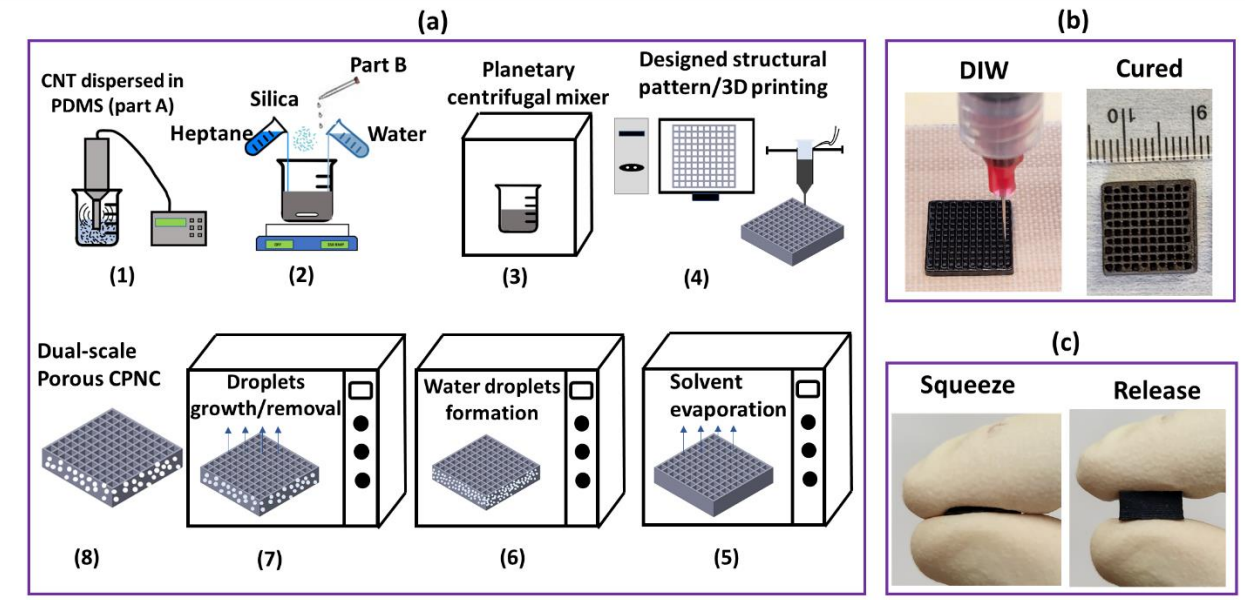

Figure 6. 1. (a) Schematic illustrates different material preparation steps, 3D printing, and phase separation. (b) pictures of a dual-scale porous sample during DIW and after the heat treatment, and (c) highly flexible porous CPNC can be squeezed and released to the original shape by a finger.

The different 3D printed samples can be categorized into four groups, where three main parameters in designing the dual-scale porous structure were investigated. First, keeping the infill density fixed as 40% and a constant needle size of 0.33 mm, the effect of microscale porosity was evaluated by preparing inks with 30%, 40%, 50%, and 100% PDMS loadings in the ternary mixture. It is worth noting that 100% PDMS means no water/Heptane in the mixture, and the structure has no microscale porosity. Second, the effect of macroscale porosity was explored by DIW of the ink with 40% PDMS using a fixed needle size of 0.33 mm and various infill densities of 30%, 40%, 50%, and 100%. Similarly, 100% infill means no macroscale porosity in the structure. Finally, the effect of deposition nozzle size was explored by DIW of the ink with fixed 40% PDMS loading, and printing design of 40% infill density, with different needle sizes of 0.21 mm, 0.26 mm, 0.33

mm, and 0.41 mm. A fully solid sample was also fabricated as a reference to compare the effect of each parameter on the porosity, pore morphology, mechanical properties, and electrical properties of the CPNC structures. The fabricated samples and the related categories are listed in Table 6.1.

Table 6. 1. The information of different samples 3D printed in this study.

Group No.	Explored parameter	PDMS loading (%)	Infill density (%)	Needle size (mm)
1	Microscale porosity (PDMS loadings)	30.00	40.00	0.33
		40.00	40.00	0.33
		50.00	40.00	0.33
		100.00	40.00	0.33
2	Macroscale porosity (Infill density)	40.00	30.00	0.33
		40.00	40.00	0.33
		40.00	50.00	0.33
		40.00	100.00	0.33
3	Printing needle size	40.00	40.00	0.21
		40.00	40.00	0.26
		40.00	40.00	0.33
		40.00	40.00	0.41
4 (full solid)	N/A	100.00	100.00	0.33

6.3. Characterization

6.3.1. Rheology Analysis

The 3D printability of the prepared inks was evaluated before DIW. The appropriate ink should possess three main rheological features to be feasible for the DIW technique. It should have shear-thinning behavior, possesses a yield point, and have solid-like properties at low shear stress. Since the polymer solution contained up to 70% solvent plus nonsolvent material, silica nanoparticles with mixing ratios of 5%, 10%, and 15% (by weight to polymer) were added to modify the rheological properties. The rheology analysis was conducted employing TA Instruments Discovery HR-2 rheometer with a 2^{o} angle cone fixture with 40 mm diameter size. The variation of the polymer solution's viscosity with a shear rate ranging between 0.01 to 100 (1/s) was obtained in the steady shear flow test. In addition, the amplitude sweep test was performed to identify the yield point in the mixture. Amplitude oscillation stress with 1 Hz frequency was applied from 1 Pa with the step of 5 Pa, and the variation of storage modulus (G') and loss modulus (G'') was obtained. The test was stopped after reaching the yield point where G' and G'' cross each other.

6.3.2. Porosity and Pore Size Distribution

The macroscale and microscale pores were evaluated by characterization of the scanning electron microscope (SEM) images captured from the internal surface of the fabricated sample. HITACHI TM3000 SEM device and Thermo Quattro S field-emission environmental SEM with 15 kV acceleration voltage were employed for capturing the images. The internal surface was sputter-coated to enhance the electrical conductivity and reduce the charging effect. The captured images were characterized using ImageJ opensource software [88]. The macroscale and microscale pores

were identified. The average cell size was calculated by statistical analysis of at least 200 microscale and 30 macroscale cells from different locations in the samples.

The porosity of the samples was calculated from the bulk density of the porous structure and density of the solid sample, as explained in Eq. 3.1.

6.3.3. Mechanical Properties

The compressive mechanical properties of the samples with different porosities were evaluated. The compressive displacement loads up to 70% strain with the strain rate of 0.01 (1/s) was applied employing an Instron 3345 single column mechanical test instrument. In addition, the loading-unloading behavior of the material was evaluated by applying 18 cyclic loads up to 30% strain. The compressive elastic modulus was obtained from the linear regression of the stress-strain curve in the elastic region.

6.3.4. Piezoresistive Response

The piezoresistive behavior of the porous CPNC with different formulations was investigated under the compressive load. The samples were placed between two copper plates attached to the compression clamps. The electrical resistance of the samples was recorded during the cyclic load via the HIOKI RM3545-02 resistance meter connected to the copper plates with wires. Eighteen cyclic loads with maximum strains ranging from 1% to 30% were applied, and the electrical resistance change in each cycle was obtained. The average electrical resistance change ($\Delta R/R$) and the gauge factor (GF) were calculated for each test as:

$$\frac{\Delta R}{R}(\%) = 100 \times \frac{R - R_o}{R_o} \tag{6.1}$$

$$GF = \frac{\Delta R/_R}{\varepsilon} \quad (6.2)$$

where R is the instantaneous electrical resistance, R_o is the initial resistance, and ε is the applied strain. The values of GF represent the strain sensitivity of the fabricated sensors. A durability test was conducted on the samples to evaluate the long-term piezoresistive response by applying the cyclic load for 700 cycles with a maximum of 15% strain load.

6.4. Results and Discussion

6.4.1. Rheological Properties

The effect of shear rate on the viscosity of the CPNC solution prepared with different silica weights was evaluated, as shown in Figure 6.2a. A typical shear thinning behavior was observed in the flow sweep test, as the viscosity was reduced constantly by increasing the shear rate. For instance, the viscosity of the ink with 5% silica was 8101 Pa.s at 0.01 s^{-1} shear rate decreased to 5.4 Pa.s at 100 s^{-1} shear rate. Shear-thinning behavior is an essential property of the ink for DIW to enable a smooth flow inside the nozzle and avoid choking issues. It is also clear that adding silica nanoparticles improved the viscosity of the CNPC solution. The viscosity of the inks at 0.01 s^{-1} shear rate is compared among the mixtures with different silica concentrations in Figure 6.2b. The average viscosity for the pristine CPNC (zero silica) was 7020 Pa.s enhanced up to 16580 Pa.s by adding 15% silica nanoparticles.

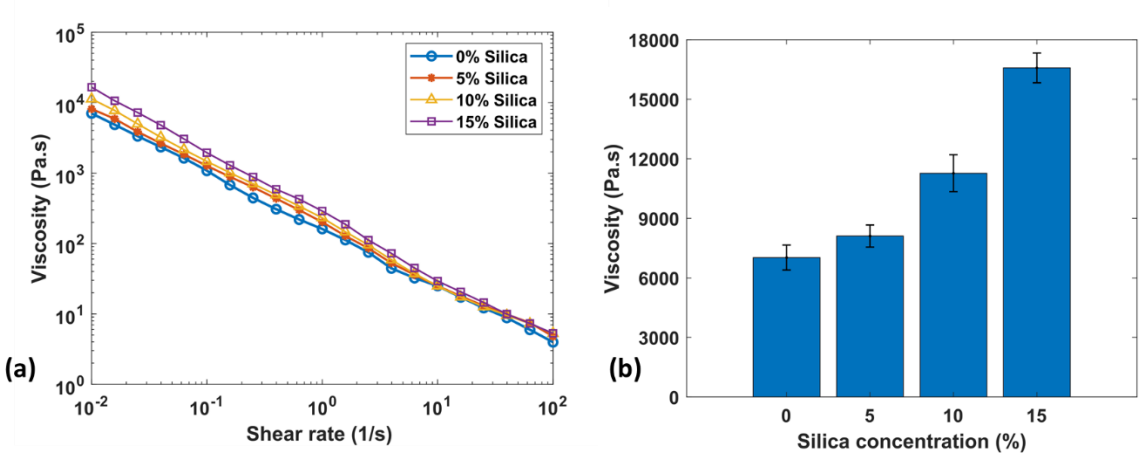

Figure 6. 2. (a) effect of shear rate on the viscosity and (b) comparison of the viscosity at 0.01 s^{-1} shear rate for the inks prepared using different silica loadings (the errorbars show the standard deviation).

The results of the amplitude sweep test are demonstrated in Figure 6.3. The effect of oscillation stress on the *G*' and *G*″ of the prepared inks with various silica nanoparticles are shown in Figure 6.3a. Both storage and loss modulus in all the formulations were initially stable by raising the applied oscillation stress and then reduced exponentially. All the inks showed typical slid-like properties at low oscillation stresses as the storage modulus values were larger than the loss modulus (*G*'>*G*″). This feature is vital for DIW as the deposited ink can retain the shape and support the materials printed on the top without spreading. The storage modulus was also enhanced by raising the silica concentration. In addition, clear yield points were observed in all the mixtures at the cross-over points of *G*' and *G*″ curves (where *G*'=*G*″). The obtained values of yield stress for the inks with different silica concentrations are depicted in Figure 6.3b. The yield stress was increased from 111 Pa up to 357 Pa by raising the silica wights from 0% to 15%, indicating the nanoparticle's rheological modifying capability. The yield stress was 171 and 201 for the mixtures with 5% and 10% silica, respectively.

The rheological analysis showed that all the formulations could be 3D printed as they showed shear thinning behavior, solid-like properties at low stress, and possessing a yield point. However, a higher storage modulus is desired for DIW since the material can hold the shape and support the above layer more efficiently. This feature is more critical in our post-deposition process when the printed structure should hold its shape during a couple of hours of heat treatment. Accordingly, the compositions with 0% and 5% silica would not be the optimum choices. Additionally, 15% silica concentration had large yield stress, viscosity, and higher nanoparticle concentration, leading to choking issues during the deposition. Hence, the 10% silica was selected as the optimum formulation for 3D printing porous CPNC structures.

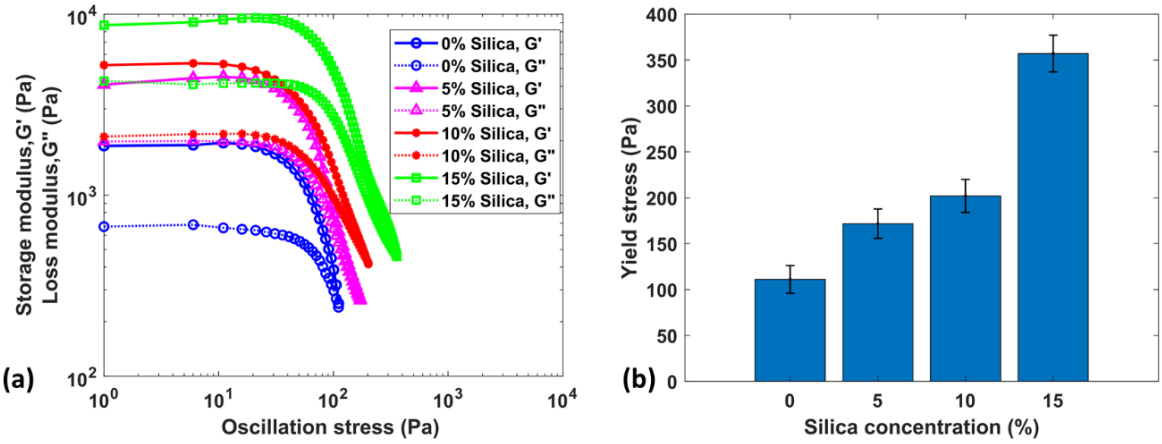

Figure 6. 3. (a) The amplitude sweep test results and (b) the yield point for the inks prepared with various silica loadings (the errorbars show the standard deviation).

6.4.2. Pore Morphology and Porosity

The SEM images of different groups of 3D printed CPNC samples are shown in Figure 6.4. Low and high magnification SEM images illustrate the macroscale and microscale porous network,

respectively. The dual-scale porous sample 3D printed with 40% infill density using the solution with 40% PDMS is illustrated in Figure 6.4a-6.4d. The structure has both macroscale and microscale porosity. It can be seen in Figure 6.4a that all the infill density design has developed a structural pattern (macroscale porosity) in the structure. The phase separation also developed microscale porosity in the deposited material. Figure 6.4b shows the area between four adjacent macroscale cells filled with microscale pores. The microscale porous network is also depicted in Figure 6.4c. The water-enriched droplets formed and grew during the phase separation, leading to cellular networks after PDMS curing and removing the water. The high magnification SEM image (Figure 6.4d) demonstrates a microscale pore where some CNTs were stuck out from the cell wall.

The internal surface of the sample with 100% infill and 40% PDMS is shown in Figure 6.4e, 6.4f. There is no macroscale porosity (Figure 6.4e), while the microscale porous network was uniformly distributed in the sample (Figure 6.4f). On the contrary, the sample fabricated with 40% infill and 100% PDMS has macroscale porosity (Figure 6.4g) but no microscale porous network (Figure 6.4h) as no nonsolvent /solvent phases were used in ink.

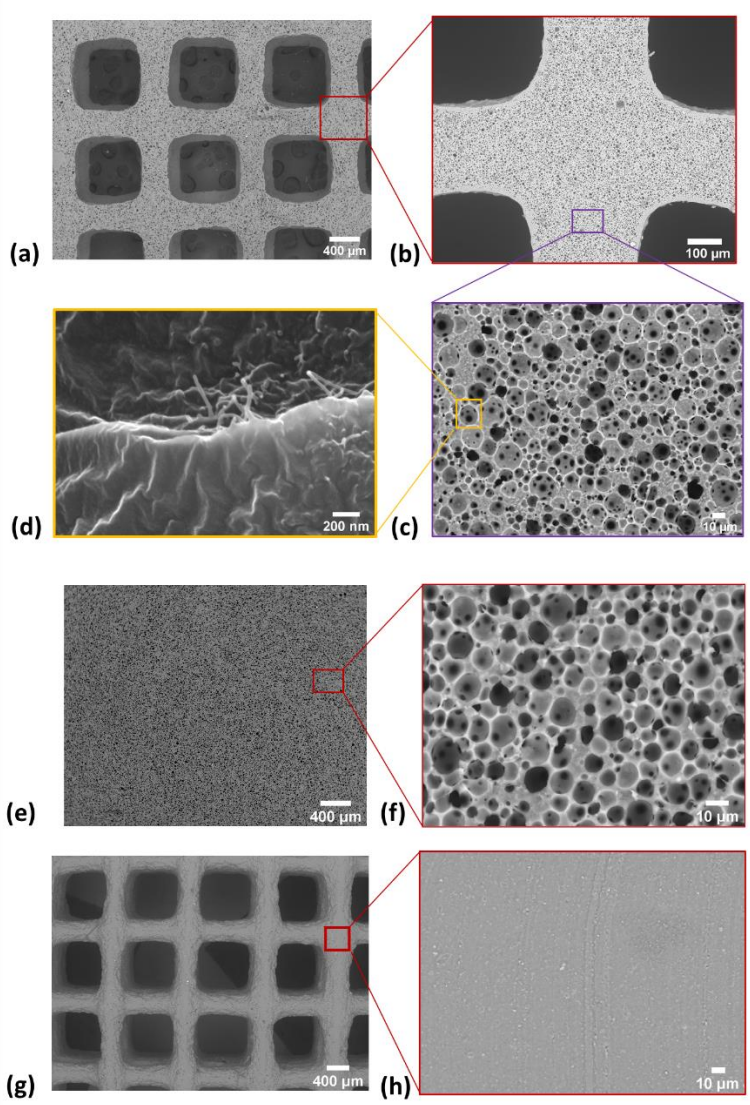

Figure 6. 4. SEM images of the samples with 40% infill and 40% PDMS: (a) Macroscale pores, (b) area between four adjacent macroscale cells, (c) microscale porous network, (d) CNTs are sticking out from a microscale cell wall. (e) Low and (f) high magnification SEM images of the samples with 100% infill and 40% PDMS. (g) Low and (h) high magnification SEM images of the samples with 40% infill and 100% PDMS.

The average size of macroscale pores (*a*, width of each square cell) and microscale pores (*d*, equivalent diameter of each cell) were calculated from the cell area as:

$$a_{macro} = \sqrt{A_{macro}} \tag{6.3}$$

$$d_{micro} = \sqrt{4A_{micro}/\pi} \tag{6.4}$$

where A_{macro} and A_{micro} is the area of the macroscale and microscale pores. In addition, the porosity of the developed structures was measured. The effect of infill density, PDMS loading, and needle size on the pore sizes was obtained as depicted in Figures 6.5 and 6.6. As expected, increasing the infill density reduced the macroscale pore size as there were fewer empty spaces in the structural pattern (Figure 6.5a). However, the microscale pore sizes with an average value of 11.6 µm were independent of the infill density since all the samples were 3D printed from the same ink formulation, as shown in Figure 6.5b. On the other hand, changing the PDMS weight ratio didn't affect the macroscale pore size with the average value of 0.96 mm (Figure 6.5c), as all the samples were 3D printed using the same infill density. The microscale pores were enlarged by reducing the PDMS weight (Figure 5d). The 30% PDMS ink led to 14.6 µm pores compared with 8.5 µm in the samples with 50% PDMS. Higher water content in the samples with lower PDMS weight enhanced the possibility of growing and coalescing the water-enriched droplets during the phase separation. Increasing the water plus Heptane in the ternary solution also reduces the mixture's viscosity, which allows the formed droplets to grow to larger droplets and microscale pores. The larger droplets also resulted in more interconnected pores in the samples with lower PDMS weight as more windows were observed in 30% PDMS concentration than 40% demonstrated in Figures 6.5e and 6.5f, respectively.

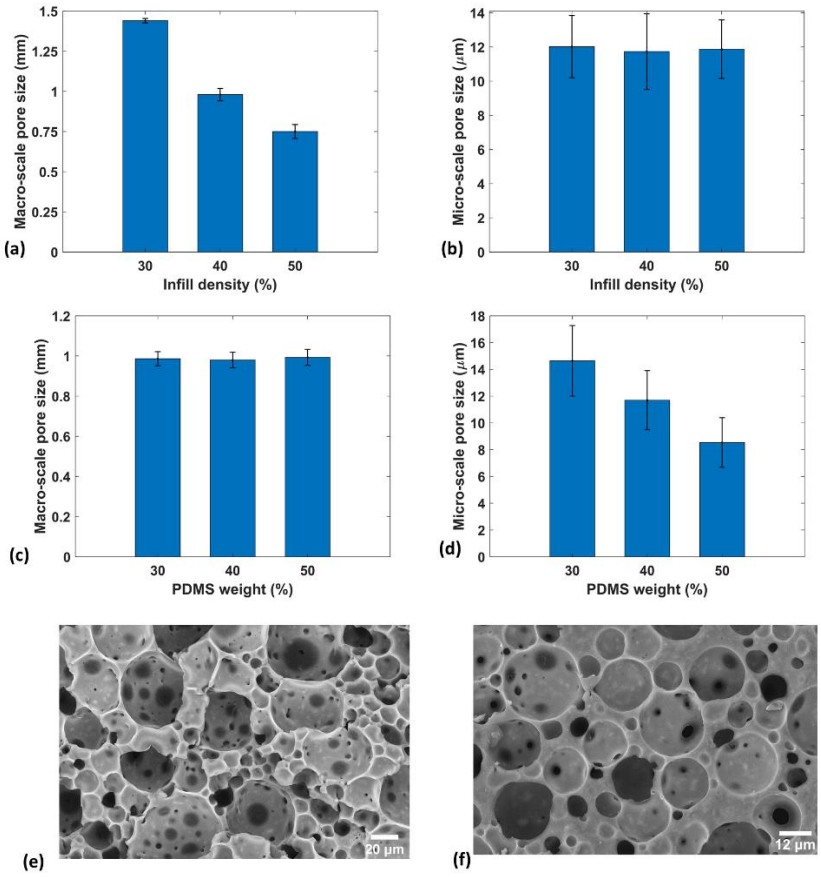

Figure 6. 5. The effect of infill density on (a) macroscale and (b) microscale pore size. The effect of PDMS weight on (c) macroscale and (d) microscale pore size (the errorbars show the standard deviation in all the curves). SEM images of samples made with (e) 30% and (f) 40% PDMS.

The effect of needle size on the macroscale pore size is shown in Figure 6.6a, where the macropores enlarged linearly with increasing the needle size. It is obvious that there were more cells with smaller sizes in the structural pattern to keep up the same 40% infill density when a smaller needle was used. As shown in Figure 6.6b, the microscale pore size slightly increased from 10.0 μm up to 13.9 μm by raising the needle size from 0.21 mm to 0.41 mm. This could be attributed to the limited area of the CPNC layer in the structures when the material was deposited utilizing smaller needle sizes. The SEM image of the internal surface at the joining area of four

adjacent macropores between 0.21 mm and 0.33 mm needle is compared in Figures 6.6c and 6.6d, respectively. It can be seen that the filled area of 0.41 mm is much wider than the 0.21 mm needle. During the phase separation, the formed water-enriched droplets had more space to grow in the 0.33 mm needle sample, while the narrow area compressed the formed droplets and prevented further growth, leading to smaller microscale pore sizes when the 0.21 mm needle was employed for the DIW.

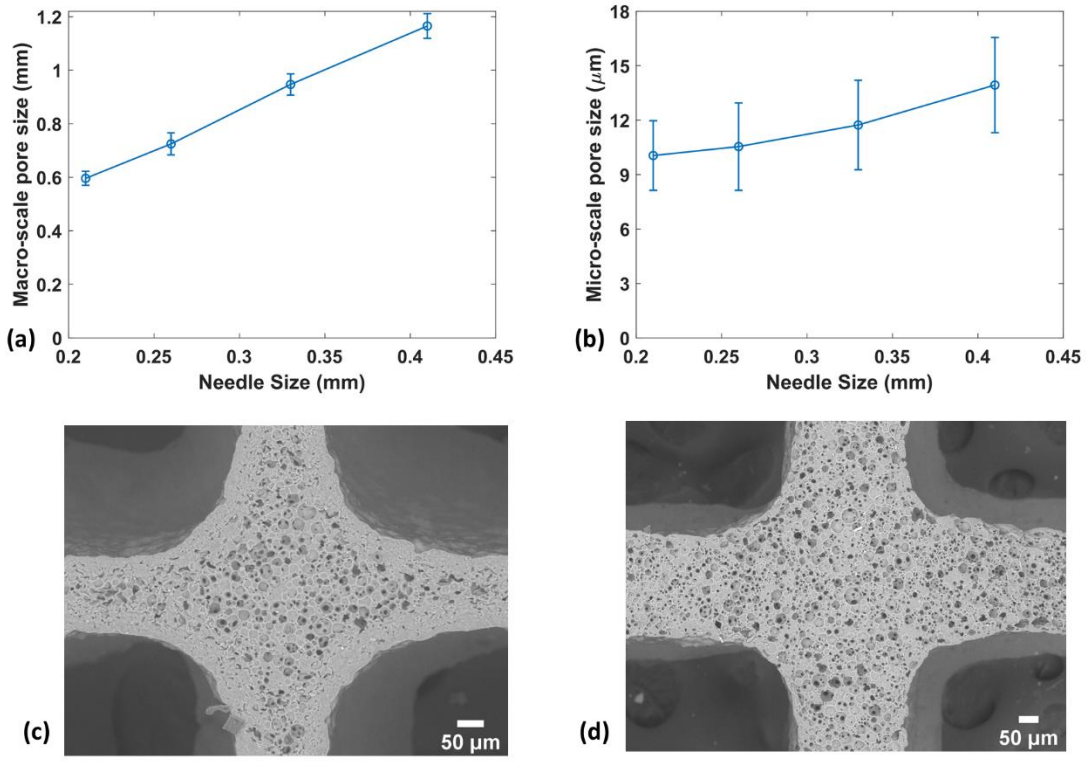

Figure 6. 6. The effect of needle size on (a) macroscale pore and (b) microscale pore size (the points show the average values, and the errorbars show the standard deviation). The SEM images show the area between four adjacent macropores in the samples printed with (c) 0.21 mm and (d) 0.33 mm needle.

The porosity of the samples with different formulations was determined. The effect of PDMS loadings on the porous structure is shown in Figure 6.7a. The porosity increased linearly from 56.7% at 100% PDMS to 81.9% at 30% PDMS. The more water plus Heptane in the ternary mixture, the more porosity since all the water/Heptane was transformed into the porous network during the phase separation. It is worth noting that there is no nonsolvent/solvent in ink utilized for the 100% PDMS sample and no microscale porosity in this structure. The results indicated the excellent effect of developing dual-scale porosity. 56.7% was the maximum porosity achievable by designing the structural pattern during the DIW. However, the porosity can be improved up to 81.9% (44% improvement) by employing the ink containing the ternary mixture and inducing the phase separation.

The variation of porosity as a function of infill density is depicted in Figure 6.7b. As expected, the porosity was enhanced by reducing the infill density. The 100% infill density demonstrates the pure microporosity as a solid geometry was 3D printed, and the porosity was developed after extrusion and during the heat treatment. The porosity for this sample was almost 60%, which is exactly correlated with the nonpolymeric phase (water+Heptane) in the ternary mixture. The results indicated that the phase separation method transformed all the nonsolvent/solvent phases into the porous network. Here again, it can be seen that the maximum porosity without dual-scale design was 60% which can be improved up to 83.5% by adding 30% infill density.

The effect of needle size on the porosity was also explored. As illustrated in Figure 6.7c, porosity was 77% in the samples developed using 0.21 mm needle enhanced up to 83.2% by increasing the needle size to 0.41 mm. Theoretically, all the samples in this category should have the same density (porosity) since the same PDMS loading and infill density was employed for the fabrication. The difference could be associated with the higher number of free surfaces in the samples when a

smaller needle size was used for extrusion. A thin film of solid CPNC covered the structure's free surface. This film was observed in all the samples' free surfaces (Figure 6.6c, 6.6d), developed due to the surface tension in the PDMS polymer. The increased number of printed patterns in the samples with smaller needle sizes enhanced the weight of the solid polymer films. In addition, there was a higher chance for the solvent/nonsolvent phases to escape the material before the separation process is complete in the structure with a thinner layer and more free spaces, leading to lower microscale porosity when a smaller needle size was utilized.

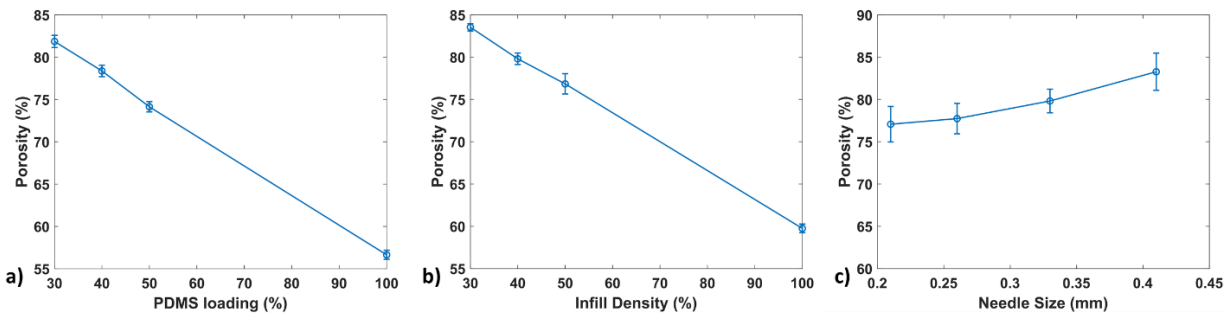

Figure 6. 7. Effect of (a) PDMS loading, (b) infill density, and (c) needle size on the porosity of the CPNC structures (the points show the average values, and the errorbars show the standard deviation in all the curves).

6.4.3. Mechanical Properties

The effect of PDMS loading on the mechanical behavior of the 3D printed porous structures under compressive loading was evaluated. As a representative, the stress-strain curves for the samples with 30%, 40%, and 50% PDMS loadings compressed up to 70% strain are shown in Figure 6.8a. A typical mechanical response in the elastomer foams under compression load was observed. The trend started with a small linear region followed by a positive slope plateau and densification. The

structure's stiffness increased by raising the PDMS concentration. The loading-unloading response of the samples with a maximum 30% strain in 18 cycles is depicted in Figure 6.8b. In order to show the effect of dual-scale porosity, the stress-strain for 100% PDMS (pure macroscale) and full solid sample are shown in Figure 6.8c. It can be seen that the porous structure has more compliance behavior improved by reducing the PDMS loading. The stiffness was directly proportional to the density of the fabricated structures. The higher polymer in the samples with more density led to greater stiffness.

The specific elastic modulus defined as elastic modulus over the density was calculated in the structures in Figure 6.8d. It was observed that the specific modulus enhanced from 20 MPa.cm3/g in 100% PDMS loading up to 34 MPa.cm3/g in the dual-scale porous sample with 30% PDMS loading. The strain values at 100 kPa for all the samples were determined to compare the structures' flexibility, as depicted in Figure 6.8e. It can be seen that the flexibility was enhanced dramatically by developing the dual-scale porosity. The strain was 40% in the sample with 30% PDMS loading compared with 4% in the full solid structure, showing 900% improvement. The outstanding flexibility of the developed structure makes it ideal for piezoresistive sensing applications. It should be noted that creating 40% infill density by 3D printing could only enhance the flexibility by 225% (from 4% strain in the full solid sample to 13% strain in 100% PDMS sample), but adding the microscale porosity can boost it up to 900% improvement.

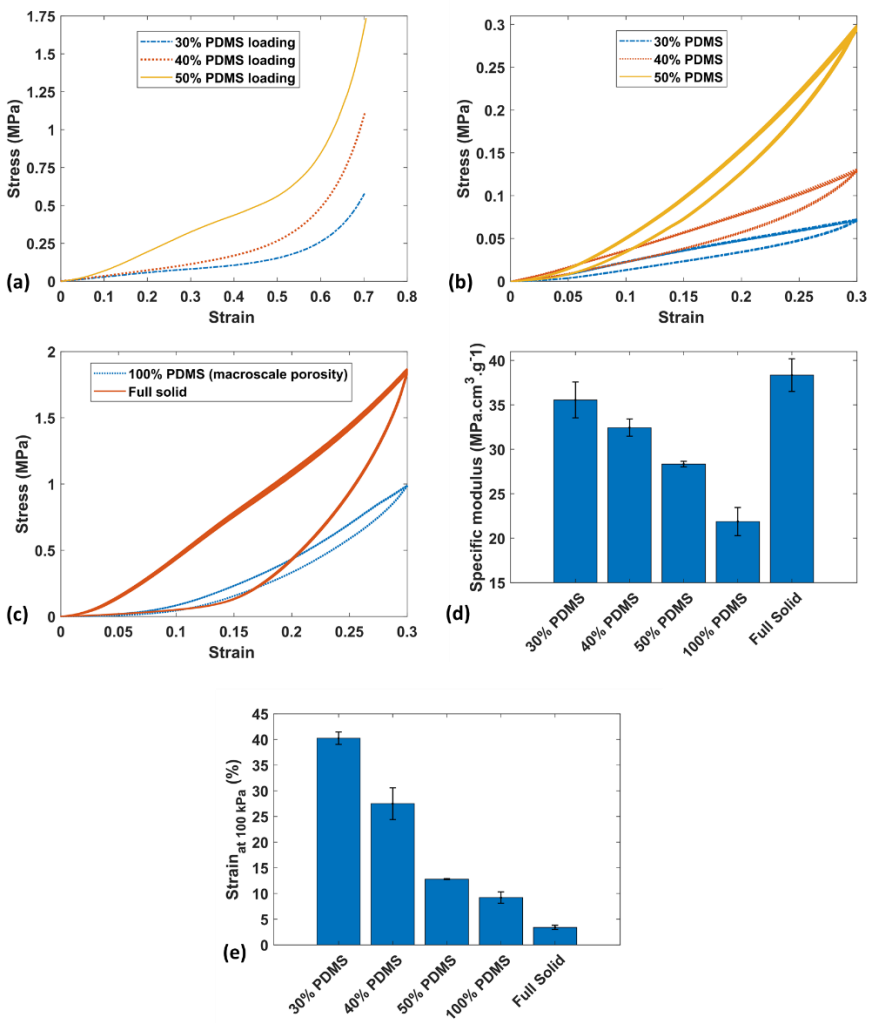

Figure 6. 8. (a) Stress-strain up to 70% strain load and (b) cyclic strain-strain up to 30% strain for the samples with different PDMS wights. (c) cyclic stress-strain curves for full solid and 100% PDMS samples. Comparison of (d) specific modulus (the errorbars show the standard deviation), and (e) strain at 100 kPa for the samples with different PDMS loadings (the errorbars show the standard deviation).

A similar analysis was conducted on the samples developed with various infill densities. As shown in Figure 6.9a, the structure stiffness was enhanced by raising the infill density. The porous structures demonstrated a repeatable compression response in the cyclic load shown in Figure 6.9b. The specific modulus was enhanced from 20.4 MPa.cm3/g in the pure microscale porous (100%

infill) to 34 MPa.cm3/g in the dual-scale porous structure. Comparing the strain values at 100 kPa showed enhanced flexibility from 4% in the full solid up to 41% in the dual-scale porous sample printed by designing 30% infill density. It is worth noting that creating pure microscale porosity can only enhance the flexibility from 4% strain to 13% (in the 100% infill sample), indicating the outstanding flexibility that the development of dual-scale porosity can add. The results revealed that the microscale porosity (PDMS loading) affected the structure's mechanical properties more than the macroscale porosity (infill density). For example, the pure microscale porous sample with 40% PDMS led to a 21.9 MPa.cm3/g specific modulus, which is greater than 20 MPa.cm3/g in the pure macroscale porous developed by 40% infill. The pure microscale porous sample also had higher flexibility than the pure macroscale as the strain at 100 kPa was 13% and 9.2% in these samples, respectively.

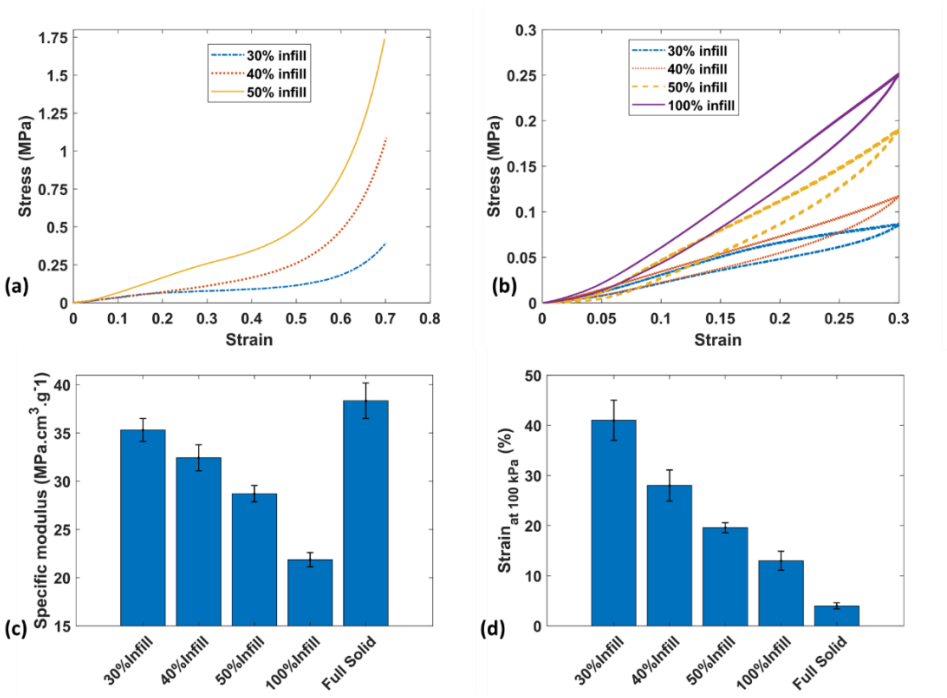

Figure 6. 9. (a) Stress-strain up to 70% strain load and (b) cyclic strain-strain up to 30% strain for the samples with different infill densities. Comparison of (c) specific modulus (the errorbars show the standard deviation), and (d) strain at 100 kPa for the samples with different infill densities (the errorbars show the standard deviation).

The effect of needle size on the compressive behavior of the dual-scale porous samples and the loading-unloading response up to 30% strain is shown in Figures 6.10a and 6.10b, respectively. It was observed that the stiffness increased by raising the needle size used for the DIW. However, the specific modulus was very close between different needle sizes, as shown in Figure 10c, while 0.41 mm led to slightly greater values. As illustrated in Figure 6.10d, the flexibility of the porous CPNC was enhanced by 128% by increasing the needle size from 0.21 mm to 0.41 mm (strain at 100 kPa was13.8% in 0.21 mm sample compared with 31.6% in 0.41 mm). Multiple parameters could cause more compliance behavior of the structure printed with larger needles, such as lower density, less solid CPNC thin-film covered the free surfaces and fewer structural supports in the designed sample.

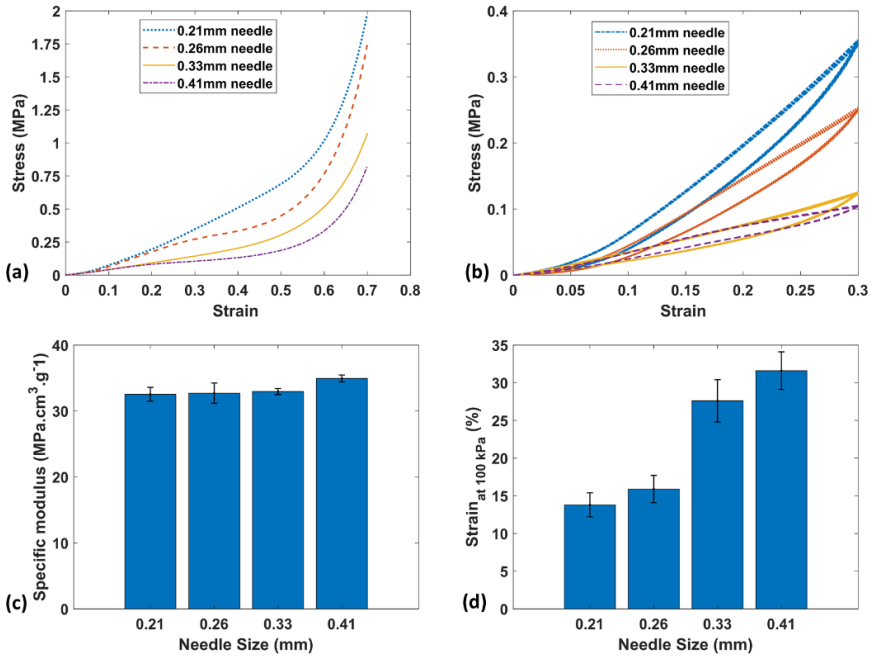

Figure 6. 10. (a) Stress-strain up to 70% strain load and (b) cyclic strain-strain up to 30% strain for the samples with different needle sizes. Comparison of (c) specific modulus (the errorbars show the standard deviation) and (d) strain at 100 kPa for the samples 3D printed using different needle sizes (the errorbars show the standard deviation).

6.4.5. Finite Element Analysis

Finite element analysis (FEA) was employed to understand which of the abovementioned parameters had the most effect on the compressive properties. Computational models with the same size and grid patterns were developed in the ABAQUS FEA package. The empirical data obtained from compressive testing of pure microscale porous samples (100%infill, 40% PDMS) were imported to define the material properties. A hyperelastic model is required to estimate the material behavior of the PDMS elastomers due to the large deformation of the polymer matrix in a small volume change. The hyperelastic materials are defined based on the strain energy potential. Multiple strain energy forms have been developed to estimate the mechanical behavior of the hyperplastic materials, including Arruda-Boyce form, Marlow form, and Mooney-Rivlin form.

Mooney-Rivlin model was utilized to describe the strain energy potential of the hyperelastic material. Generally, the strain energy (W) can be defined based on the deviatoric strain invariant ($\bar{I}_i$) and elastic volume ratio (J) , as [123]:

$$W = W(\bar{I}_1, \bar{I}_2, \bar{I}_3, J) \tag{6.5}$$

where $\bar{I}_1$, $\bar{I}_2$, $\bar{I}_3$ are the invariant of the deviatoric component of the left Cauchy-Green deformation tensor. The invariant of the deviatoric component can be calculated as:

$$\bar{I}_1 = \bar{\lambda}_1^2 + \bar{\lambda}_2^2 + \bar{\lambda}_3^2 \tag{6.6}$$

$$\bar{I}_2 = \frac{1}{\bar{\lambda}_1^2} + \frac{1}{\bar{\lambda}_2^2} + \frac{1}{\bar{\lambda}_3^2} \tag{6.7}$$

$$\bar{I}_3 = \bar{\lambda}_1^2 \bar{\lambda}_2^2 \bar{\lambda}_3^2 \tag{6.8}$$

where $\bar{\lambda}_1$, $\bar{\lambda}_2$, and $\bar{\lambda}_3$ are the deviatoric stretches. For the uniaxial test (tension or compression), the deviatoric stretches can be calculated as [124]:

$$\bar{\lambda}_1 = \lambda;\ \bar{\lambda}_2 = \bar{\lambda}_3 = \frac{1}{\sqrt{\lambda}} \tag{6.9}$$

where λ is the stretch in the loading direction and can be calculated from the nominal strain (ε) as $\lambda = 1 + \varepsilon$. The general form of the strain energy density function can be re-written in the polynomial form as:

$$W(\bar{I}_1, \bar{I}_2, \bar{I}_3, J) = \sum_{ijk=0}^{N} C_{ijk} (\bar{I}_1 - 3)^i (\bar{I}_2 - 3)^j (\bar{I}_3 - 1)^k + \sum_{i=1}^{N} \frac{1}{d} (J - 1)^{2i} \tag{6.10}$$

With the assumption of material incompressibility, $\overline{I_3} = 1$. Based on the five-term Mooney-Rivlin second order, the strain energy potential can be expressed as [125] :

$$W_{(5)} = C_{10}(\overline{I_1} - 3) + C_{01}(\overline{I_2} - 3) + C_{20}(\overline{I_1} - 3)^2 + C_{11}(\overline{I_1} - 3)(\overline{I_2} - 3) + C_{02}(\overline{I_2} - 3)^2 + \frac{1}{d}(J - 1)^2 \tag{6.11}$$

where C_{01}, C_{10}, C_{11}, C_{02}, and C_{20} are material constants and d is the material incompressible parameters that can be calculated from the experimental curve fitting. These parameters are calculated form the "evaluate" function of Abaqus software. The software determines these constants through a least-squares-fit procedure, which minimizes the relative error between the stress value from the test data and the nominal stress expressions. The experimental stress-strain data and estimation from the Mooney-Rivlin hyperelastic model with 5 terms are compared in Figure 6.11. Very good agreement between the experimental data and the hyperelastic model can be seen in this figure. The five material constant parameters required for modeling the Mooney-Rivlin model are calculated as shown in Table 6.2.

Table 6. 2. The hyperelastic material constants calculated using the Mooney-Rivlin model.

Parameter	C_{01} (kPa)	C_{10} (kPa)	C_{11} (kPa)	C_{02} (kPa)	C_{20} (kPa)	d
Value	-770	833	20012	-13921	-7411	1.65

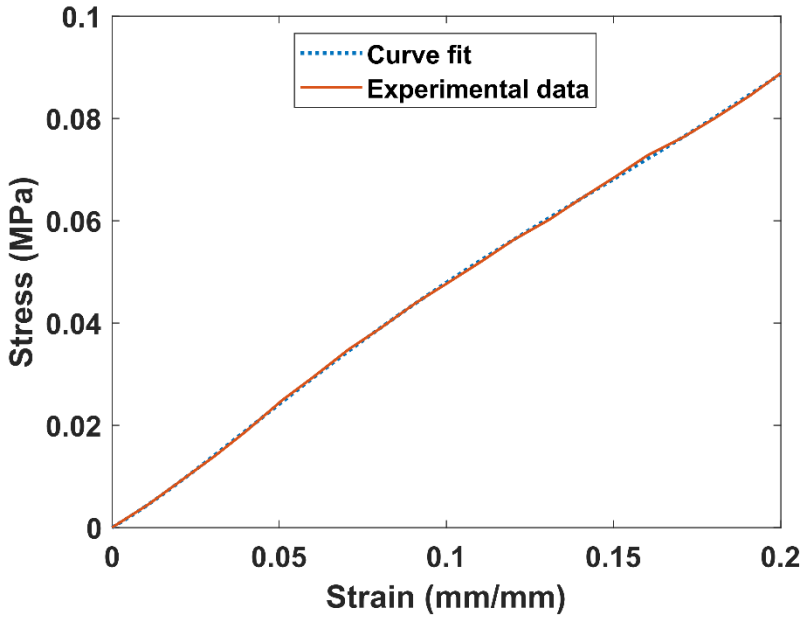

Figure 6. 11. Comparison of the experimental data and the 5-term Mooney-Rivlin hyperelastic model.

The 8-node linear brick element with improved surface stress visualization (C3D8S) was utilized in the FEA. To simulate the compressive mechanical test, a rigid block was modeled as the loading head applying the displacement load, and the lower surface of the structure was fixed. The reaction force and displacement of the loading head were obtained and used to calculate the stress and strain in the structure. The deformed models representing the 0.21 mm and 0.41 mm needle sizes are shown in Figures 6.12a and 6.12b, respectively. The stress-strain response during the compressive load was determined in the models. The effect of needle size on the mechanical properties obtained from FEA and experiments are shown in Figures 6.12c and 6.12d, respectively. Similar to experiments, stiffer behavior was observed as the needle size was reduced in the FEA. The numerical stress values at 0.2 strain for the structures fabricated using 0.41 mm, 0.33 mm, 0.26

mm, and 021 mm were 79 MPa and 91.4 MPa, 97 MPa, and 104 MPa, respectively. It is worth noting that the material properties of the filled area in all the models were the same, and the consistent infill density led to a fixed density in the FEA. Hence, it can be claimed that more structural support in the samples with smaller needles led to a stiffer mechanical behavior. In addition, the computational results in 0.41 mm and 0.33mm were close to the experimental results, as shown in (Figure 6.12c). However, the 0.21 mm and 0.26 mm samples had higher stiffness in the experiments than the FEA (Figure 6.12d). The difference could be associated with the samples' higher density (lower porosity) when smaller needle sizes were used in the experiments discussed before (Figure 6.7c). Accordingly, the higher solid polymer available in these structures led to stiffer behavior in the experiments than in the FEA, where all the structures have the same bulk density.

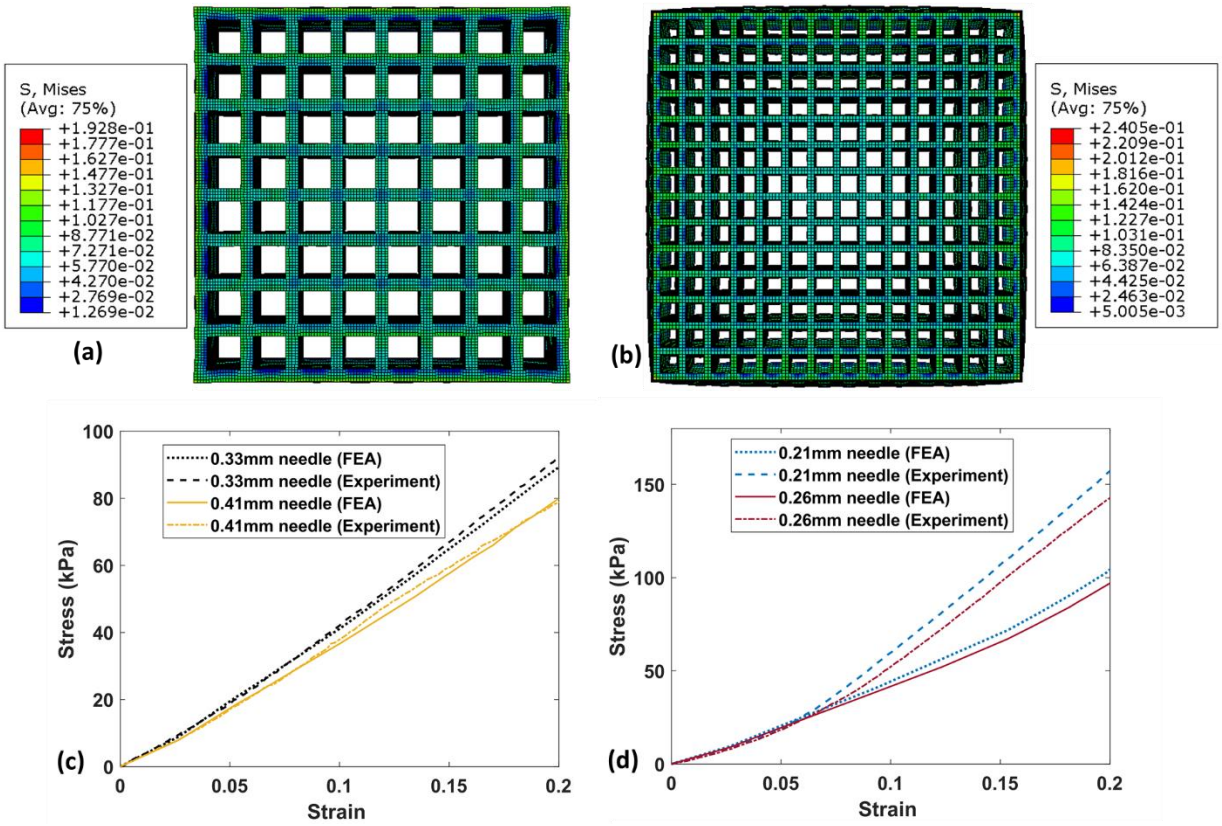

Figure 6. 12. Deformed FEA model with (a) 0.41 mm needle and (b) 0.21 mm needle size. Comparing experimental and FEA stress-strain curves for the samples with (c) 0.33 mm and 0.41 mm needle sizes, and (d) 0.26 mm and 0.21 mm needle sizes.

6.4.5. Piezoresistive Response

The piezoresistive strain sensing response of the porous CPNC with different formulations was characterized. As a representative, the electrical resistance changes in the five loading-unloading cycles with different maximum strains in the samples 3D printed using 40% infill and 40% PDMS ink are illustrated in Figure 6.13a. A highly repeatable piezoresistive response can be seen in this figure. The resistance of the porous CPNC was reduced by applying compressive load, as more conductive pathways were formed when the structure was compressed. The resistance change was enhanced by increasing the compressive deformation in the structures. The average value of GF in

18 applied loading-unloading cycles was calculated for all the samples. The variation of GF as a function of the applied strain in different categories of samples is shown in Figures 6.13b - 6.13d. It was observed that GF decreased as the applied strain was increased. This trend is associated with the weakening of the tunneling effect in the conductive network as the applied deformation increases. New electrical pathways form when the CNT networks become closer, leading to further electrical resistance changes. However, this effect wanes when the network gets very close or when physical contact becomes dominant in the conductive network. Thus, increasing the applied compressive deformation has less effect on the piezoresistive sensing response.

The effect of PDMS infill density on the sensitivity of the porous CNPC is shown in Figure 6.13b. Higher sensitivity was observed in the samples with lower PDMS content (higher porosity). At 1% strain, GF was 13.6 in the 100%PDMS sample, increased up to 19.9 in the sample made with 30% PDMS. This could be attributed to the higher microscale porosity in the samples with lower PDMS concentration, enhancing the changes in the electrically conductive network. The CNTs located on the cell walls can create new pathways when the pores are compressed during the compression load due to the tunneling effect or physical contact (if the cell collapse). The enhanced changes in the network of the samples with higher microscale porosity led to higher resistance change and sensitivity of the structure. Moreover, no obvious changes were observed in the second sample group when the infill density was changed between 30% to 100% during 3D printing, as depicted in Figure 6.13c. All the samples had a GF in the range of 16.2-16.6 at 1% applied strain. The similar microscale porous network in this group resulted in equivalent piezoresistive responses. Finally, the effect of needle size on the sensing response of the porous CPNC is illustrated in Figure 6.13d. A slight improvement in the piezoresistive response was observed by increasing the needle size, as shown in Figure 6.13d. As discussed before, a larger needle size

resulted in greater microscale porosity in the structure, enhancing the changes in the conductive network and sensitivity.

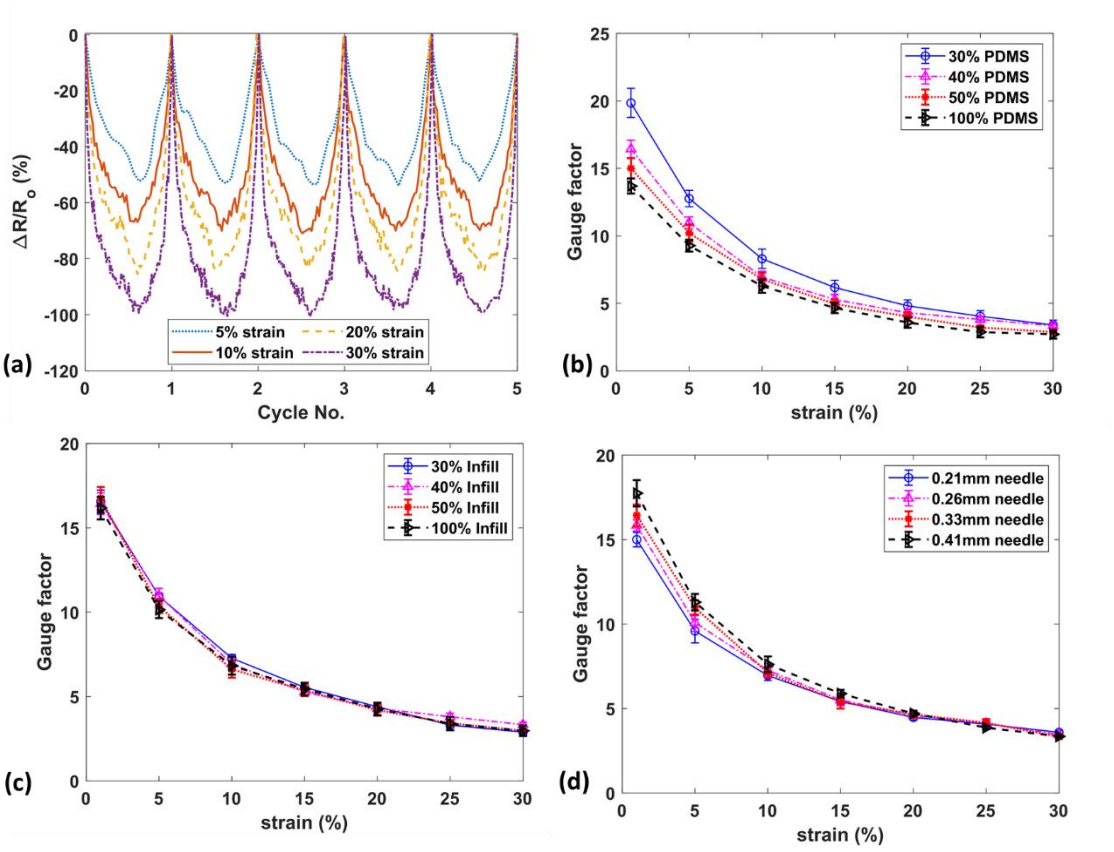

Figure 6. 13. (a) Electrical resistance changes in the five loading-unloading cycles with different maximum strains, (b) The GF at different strains for samples with various PDMS loadings, (c) The GF at different strains for samples with various infill densities, and (d) The GF at different strains for samples 3D printed with different needle sizes (the points show the average values, and the errorbars show the standard deviation).

The long-term piezoresistive response of the dual-scale porous CPNC was evaluated under the 700 cyclic compressive test with a maximum 15% strain load. The relative resistance changes in the sample made with 40% PDMS and 40% infill density is compared with the response of the full

solid sample in Figure 6.14a. A stable piezoresistive response was observed in the dual-scale porous sample, while there was a continuous downward drift in the electric response of the solid samples. The average resistance change (the difference between peak and valley in each cycle) was 87% in the dual-scale porous sample compared with 52% in the full solid structure. The drift was more severe in the initial cycles and slowed down as the number of cycles increased. The different long-term responses between the solid and porous samples could be attributed to the viscoelastic behavior of the PDMS elastomer. Mechanical and electrical relaxation have been reported for the PDMS polymer during the cyclic fatigue load. However, the dual-scale porous structure had up to 80% less polymer material than the solid sample, leading to a negligible viscoelastic effect and drifting in the piezoresistive response.

Additionally, as shown in Figure 6.14b, there was a small peak in the resistance change of the solid structure when the strain reached the maximum values in each cycle, which was not visible in the dual-scale porous sample. This hysteresis in the piezoresistive response of the solid sensors has been reported elsewhere, but it has not been understood well [6, 13]. Different reasons have been introduced for this behavior, including the breakdown of the conductive pathways and the electromechanical relaxation of the polymer matrix [111]. The hysteresis was negligible in the dual-scale porous structure since 80% less polymer was used in the composition, preventing the viscoelastic and relaxation behavior of the material and the conductive network. The results indicate the durability, trustworthiness, and consistent sensitivity of the 3D printed dual-scale porous CPNC in long-term strain sensing applications.

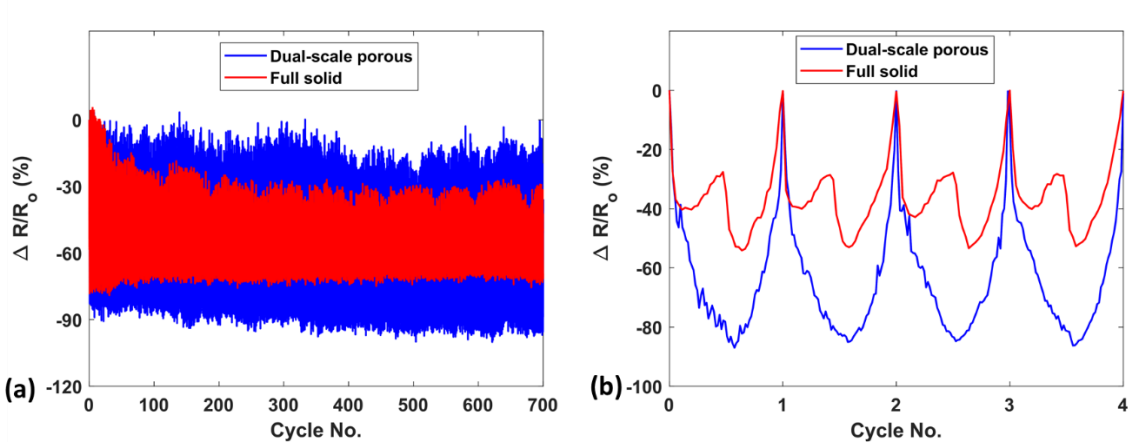

Figure 6. 14. Comparing the durability of the piezoresistive response in the dual-scale porous and full solid sample, and (b) Comparison of the cyclic sensing response between the full solid and dual-scale porous sample.

The ability of the fabricated dual-scale porous CPNC in detecting human body motion was evaluated. In the first test, the sensor was affixed on the thumb between two copper tapes connected to the resistance meter to detect the compressive deformation when a person grabs an object. The applied load and deformation on the sensor are directly related to the grabbed object's weight. Here, a coffee mug filled at different empty, half full, and full levels was grabbed and released. The sensor attached to the thumb was in contact with the cup when the mug was held. The electrical resistance change of the sensor at each level of filling was measured as depicted in Figure 6.15a. A higher piezoresistive response was observed as more coffee filled the mug. Moreover, the operator applied two types of pressure while the mug was held: continuous press/release and press/hold/release. The resistance change for these two tests was obtained. Figure 6.15b illustrates the piezoresistive response related to the continuous press/release with a repeatable cyclic response. The press/hold/release response is also shown in Figure 6.15c. The plateau area in this

figure indicates the hold time when the resistance was stable. The results prove that the developed sensor can detect body motion.

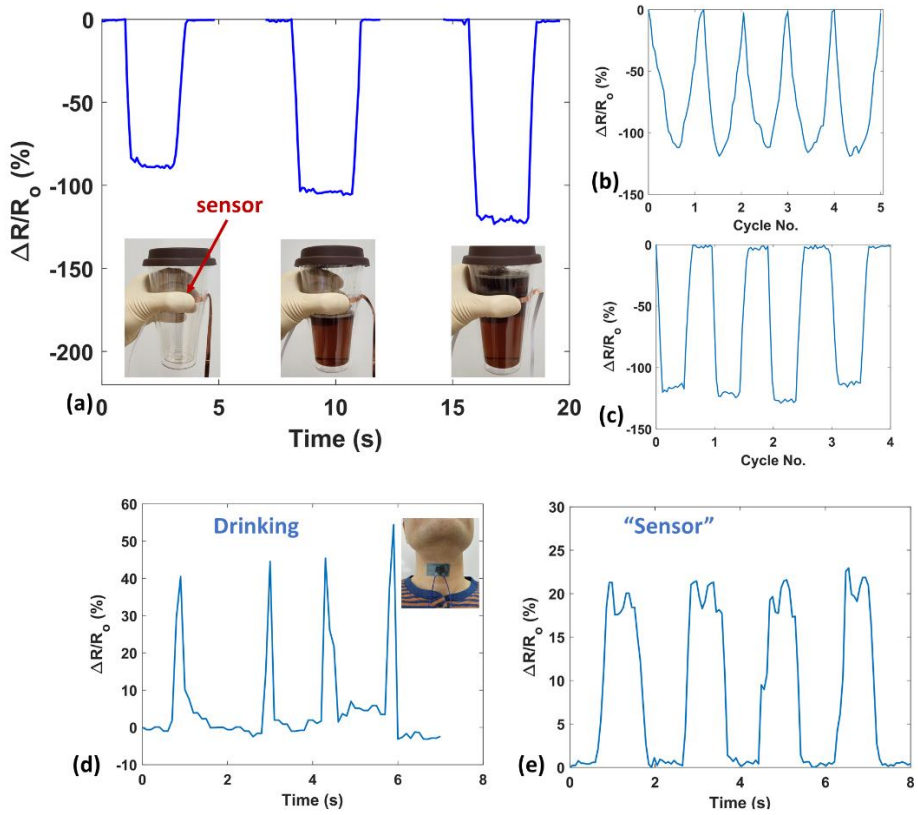

Figure 6. 15. Detection of human body motion: (a) Piezoresistive response related to grabbing a mug filled at different levels. (b) sensing response caused by a thumb related to (b) continuous press/release and (c) press/hold/release. Detection of throat muscle movement during (d) drinking and (e) pronouncing the word "sensor".

The capability of the porous CPNC in tactile sensing was also explored. A rectangle dual-scale porous specimen was fabricated affixed on a polyimide tape. Two electrical wires were glued to the sensor and connected to the resistance meter to detect the piezoresistive response. The sensor and wires were covered by another layer of tape and attached to the throat to detect muscle

movement during drinking and speaking. The piezoresistive response related to drinking is shown in Figure 6.15d. The resistance was stable in the relaxed muscle and showed a signal pattern during swallowing. A clear signal pattern was also detected when the operator pronounces the “sensor” word, as shown in Figure 6.15e. The muscle movement caused by opening the lower jaw during speaking led to deformation on the attached sensor and the related resistance change. The results demonstrate the ability of the developed dual-scale porous CPNC in soft robotics and health monitoring.

6.5. Chapter Conclusion

This study proposed dual-scale porosity in CPNC structure to achieve ultralightweight and highly flexible piezoresistive strain sensors. Adjustable macroscale porosity was established by designing the structural printing patterns with various infill densities during DIW. The microscale porous network was developed using the phase separation technique induced by solvent evaporation. The viscoelastic ink was prepared by mixing PDMS/CNT with water (nonsolvent) and Heptane (solvent) phases. The silica nanoparticle was employed and optimized to modify the rheological properties of the polymer solution. Free-standing, 3D cubic-shaped samples were 3D printed, followed by a stepping heat treatment to trigger the phase separation, water removal, and polymer curing. The mechanical and piezoresistive behavior of the developed sensor was investigated.

The effects of infill density and polymer density on the macro/micro-scale porosity were evaluated. It was observed that the combination of both types of densities could lead to ultralightweight with up to 84% porosity. In comparison, 70% was the maximum porosity achieved by the individual (macro/micro) cellular networks. The experimental results showed that the flexibility and sensitivity of the structure were enhanced up to 900% and 67% by the development of dual-scale

porosity. Increasing the microscale porosity had more effect on enhancing the piezoresistive sensitivity of the CPNC structure than the macroscale porosity. The CNTs on the cell walls create new conductive pathways when the pore is compressed, leading to higher resistance change. The effect of printing nozzle size on the porosity, mechanical properties, and electrical response of the porous CPNC was also explored. It was observed that the porosity, compliance behavior, and sensitivity were increased by raising the nozzle size. FEA was employed to verify that a smaller nozzle can lead to a stiffer structure. A stable and durable mechanical and piezoresistive response with negligible relaxation and hysteresis was observed in the long-term analysis. The ability of the developed porous CPNC to detect human body motion was also evaluated. The 3D printed dual-scale porous sample successfully detected the load on the thumb during the holding/releasing of a coffee mug filled at different levels. The developed sensor was also able to detect the throat's muscle movement during speaking and drinking.

Chapter 7: Conclusion and Future Work

7.1. Conclusion

In the first part of this dissertation, the application of solvent evaporation-induced phase separation as a promising technique to create porous polymer structures was investigated. The ternary polymer solution consisting of polymer/solvent/nonsolvent (PDMS/THF/water) was explored. The parameters required for constructing the phase diagram were calculated based on the numerical method and thermodynamics equilibrations. The ternary phase diagram showing the thermodynamic equilibrium state for a polymeric solution was constructed. The possible composition path during the heat treatment and phase separation procedure was obtained. The critical point was calculated as 8.4% PDMS weight. Because of the low polymer weight at the critical point, nucleation and growth (NG) would be the primary phase separation mechanism. The composition slowly passes a line from a homogeneous region to the metastable domain.

The fabrication and analysis of porous PDMS structures formed by solvent evaporation-induced phase separation were discussed in this study. Different formulations of polymer solutions with various PDMS concentrations and water/THF ratios were investigated. The analytical ternary phase diagram in the water/ THF/PDMS system was used to determine the stable, unstable, and metastable regions and the binodal, spinodal curves. The fabricated porous samples were analyzed to evaluate the pore size distribution, mechanical properties, and porosity microstructure. The main observation of this study can be listed as:

- The isolated pores with an average pore size ranging from 330 µm to 1900 µm were obtained from NG of the water enriched droplets in the PDMS-rich domain.

- In the formulations with the same PDMS concentration, the average pore size was decreased by raising the water/THF ratio. However, similar pore size was achieved by changing the PDMS concentrations from 30% to 60% and keeping the water/THF ratio fixed.
- The tensile tests revealed that the samples with larger pore sizes had more flexibility than the specimens with small pore sizes.
- A wide range of elastic modulus ranging between 0.49-1.05 MPa could be achieved in the samples with the same density by adjusting the non-solvent/solvent content in the solution. Higher polymer weight can increase stiffness and reduce porosity.
- The porosity of the samples was controlled by the polymer concentration, while a negligible effect was observed from changing the non-solvent/solvent ratio.

Additionally, A two-step phase separation technique was developed in this dissertation for inducing the porous structure with a wide range of properties. Toluene and THF with various mixing ratios were utilized as the solvent phase in the polymer/solvent/nonsolvent system, while the polymer and nonsolvent content were considered constant parameters. The pore distribution, mechanical properties, and porosity of porous PDMS structures with different formulations were examined.

- Two distinct pore size distribution was found in the porous network. The pores with an average size of 28 μm were related to the first step of phase separation (THF effect), while evaporation of Toluene resulted in the formation of the pores with an average size of 509 μm.
- The microstructure of the porous network changed with THF/Toluene ratio. The large pore concentration increased, and the small pores filling between the large pores decreased by raising the THF/solvent ratio.

- The porous PDMS density was directly related to the polymer concentration in the solution and independent from the solvent phase (microstructure).
- The mechanical tests showed that the hybrid-cell structure resulted in higher flexibility compared to the uniform cell structure. For hybrid-cell structure, the sample with THF/solvent=5:10 had the highest flexibility, which was 48% higher than the sample with THF/solvent=0:10. For uniform cell structure, the sample with smaller pores (100% Toluene) was stiffer than the sample with a larger pore size (100% THF).
- The empirical relationship was also developed based on the experimental data to estimate the elastic modulus and the pore size in the sample fabricated by the proposed formulations.

Moreover, A novel approach was developed in this dissertation for 3D printing of porous CPNCs by combining the DIW method and solvent evaporation induced phase separation technique. The ink was prepared by mixing CNT/PDMS nanocomposite with solvent and nonsolvent phases. Acceptable rheological properties of the ink, including shear thinning behavior, yield stress, and sufficient storage modulus, indicated the printability of the prepared mixtures. Free-standing piezoresistive sensors were fabricated by depositing the prepared ink with various formulations.

This study proposed dual-scale porosity in CPNC structure to achieve ultralightweight and highly flexible piezoresistive strain sensors. Adjustable macroscale porosity was established by designing the structural printing patterns with various infill densities during DIW. The microscale porous network was developed using the phase separation technique induced by solvent evaporation. The effect of CNT concentration, macro-scale porosity (infill density), micro-scale porosity (PDMS weight), and printing nozzle size on the mechanical and piezoresistive behavior of the porous CPNC was investigated.

- Adjustable micro-scale pores ranging from 5.4 μm to 9.9 μm were observed in the structures with different formulations. Increasing CNT content reduced the micro-scale pore sizes.
- The samples with 1% CNT showed the highest piezoresistive sensitivity, as high as GF=19.8 (191% higher than 2% CNT) and the highest flexibility (47.6% higher than 2% CNT).
- It was observed that the combination of both macro and micro scale porosity could lead to ultralightweight with up to 83% porosity. In comparison, 70% was the maximum porosity achieved by the individual (macro/micro) cellular networks.
- The experimental results showed that the flexibility and sensitivity of the structure were enhanced up to 900% and 67% by the development of dual-scale porosity.
- Increasing the microscale porosity had more effect on enhancing the piezoresistive sensitivity of the CPNC structure than the macroscale porosity. The CNTs on the cell walls create new conductive pathways when the pore is compressed, leading to higher resistance change.
- The effect of printing nozzle size on the porosity, mechanical properties, and electrical response of the porous CPNC was also explored. It was observed that the porosity, compliance behavior, and sensitivity were increased by raising the nozzle size. FEA was employed to verify that a smaller nozzle can lead to a stiffer structure.
- A stable and durable mechanical and piezoresistive response with negligible relaxation and hysteresis was observed in the long-term analysis.
- The ability of the developed porous CPNC to detect human body motion was also evaluated. The 3D printed dual-scale porous sample successfully detected the load on the thumb during the holding/releasing of a coffee mug filled at different levels. The developed sensor was also able to detect the throat's muscle movement during speaking and drinking.

7.2. Recommendations for Future Work

In this research, the solvent evaporation-induced phase separation technique was developed to synthesize porous PDMS polymer-based structures. This method was also combined with 3D printing to develop highly porous and flexible CPNC with dual-scale porosity and piezoresistive sensing functions. Some recommendations to extend this study are summarized as follows:

- The phase separation technique can be used for other polymers to develop porous structures with wearable electronics and soft robotics applications. For example, Ecoflex has been used to fabricate strain sensors due to its biocompatible, high flexibility, and stretchability [6]. The proposed formulation can be utilized to enhance the properties of the Ecoflex-based structures.
- MWNTs have been employed as conductive nanofiller to enhance the electrical conductivity of the PDMS nanocomposites. It is recommended that the effect of other fillers such as graphene and metal nanoparticle or hybrid network on the piezoresistive sensitivity be investigated.
- The dual-scale porous conductive nanocomposite developed in this research can be utilized as pressure sensor. Due to low elastic modulus and high flexibility, the highly porous structure can lead to great pressure sensitivity. The soft and compressible porous CPNC makes it an ideal structure for this application.
- The structural grid pattern was used to 3D print dual-scale porosity in this research. It was observed that the flexibility of the structure is affected by the structural support provided by the macro-scale design. The effect of other printing patterns such as rectilinear on the mechanical and piezoresistive behavior can be explored. Moreover, the dual-scale porous structure can be loaded in a direction normal to the macro-scale pores. It is expected that

compressing the pores so that new conductive pathways are formed can enhance the piezoresistive sensitivity.

- The applications of the dual-scale porosity proposed in this dissertation can be extended to piezoelectric sensors. High sensitivity is required in wearable electronics and tactile sensors. Generally, piezoelectric sensors are more sensitive than piezoresistive sensors since the changes in the current or voltage are measured in piezoelectric, while resistance change is measured in piezoresistive sensors. In addition, the piezoresistive sensors made with flexible polymer suffer from detectability at very small strains, while piezoelectric sensors can detect very small deformation. Accordingly, porous polymers with piezoelectric capabilities such as poly(vinylidene fluoride) PVDF, poly(vinylidene fluoride-co-trifluoroethylene) PVDF-TrFE, and poly(L-lactic acid) PLLA can be investigated. In addition, piezoelectric nanostructures such as Nanocellulose can be added to PDMS to enable piezoelectric function.

References

[1] Yang JC, Mun J, Kwon SY, Park S, Bao Z, Park S. Electronic skin: recent progress and future prospects for skin-attachable devices for health monitoring, robotics, and prosthetics. Advanced Materials. 2019;31(48):1904765.

[2] Bettucci O, Matrone GM, Santoro F. Conductive polymer-based bioelectronic platforms toward sustainable and biointegrated devices: A journey from skin to brain across human body interfaces. Advanced Materials Technologies. 2021:2100293.

[3] Yin F, Ye D, Zhu C, Qiu L, Huang Y. Stretchable, highly durable ternary nanocomposite strain sensor for structural health monitoring of flexible aircraft. Sensors. 2017;17(11):2677.

[4] Yi L, Jiao W, Wu K, Qian L, Yu X, Xia Q, *et al*. Nanoparticle monolayer-based flexible strain gauge with ultrafast dynamic response for acoustic vibration detection. Nano Research. 2015;8(9):2978-87.

[5] Liu H, Huang W, Gao J, Dai K, Zheng G, Liu C, *et al*. Piezoresistive behavior of porous carbon nanotube-thermoplastic polyurethane conductive nanocomposites with ultrahigh compressibility. Applied Physics Letters. 2016;108(1):011904.

[6] Herren B, Saha MC, Altan MC, Liu Y. Development of ultrastretchable and skin attachable nanocomposites for human motion monitoring via embedded 3D printing. Composites Part B: Engineering. 2020;200:108224.

[7] Hwang J, Kim Y, Yang H, Oh JH. Fabrication of hierarchically porous structured PDMS composites and their application as a flexible capacitive pressure sensor. Composites Part B: Engineering. 2021;211:108607.

[8] Zhu D, Handschuh-Wang S, Zhou X. Recent progress in fabrication and application of polydimethylsiloxane sponges. Journal of Materials Chemistry A. 2017;5(32):16467-97.

[9] Chen Y-F, Li J, Tan Y-J, Cai J-H, Tang X-H, Liu J-H, *et al*. Achieving highly electrical conductivity and piezoresistive sensitivity in polydimethylsiloxane/multi-walled carbon nanotube composites via the incorporation of silicon dioxide micro-particles. Composites Science and Technology. 2019;177:41-8.

[10] Lee S, Shin S, Lee S, Seo J, Lee J, Son S, *et al*. Ag nanowire reinforced highly stretchable conductive fibers for wearable electronics. Advanced Functional Materials. 2015;25(21):3114-21.

[11] Jiang D, Wang Y, Li B, Sun C, Wu Z, Yan H, *et al*. Flexible sandwich structural strain sensor based on silver nanowires decorated with self-healing substrate. Macromolecular Materials and Engineering. 2019;304(7):1900074.

[12] Chowdhury SA, Saha MC, Patterson S, Robison T, Liu Y. Highly conductive polydimethylsiloxane/carbon nanofiber composites for flexible sensor applications. Advanced Materials Technologies. 2019;4(1):1800398.

[13] Abshirini M, Charara M, Liu Y, Saha M, Altan MC. 3D printing of highly stretchable strain sensors based on carbon nanotube nanocomposites. Advanced Engineering Materials. 2018;20(10):1800425.

[14] Cao H, Thakar SK, Oseng ML, Nguyen CM, Jebali C, Kouki AB, *et al*. Development and characterization of a novel interdigitated capacitive strain sensor for structural health monitoring. IEEE Sensors Journal. 2015;15(11):6542-8.

[15] Luo W, Charara M, Saha MC, Liu Y. Fabrication and characterization of porous CNF/PDMS nanocomposites for sensing applications. Applied Nanoscience. 2018:1-9.

[16] Fallahi A, Bahramzadeh Y, Tabatabaie S, Shahinpoor M. A novel multifunctional soft robotic transducer made with poly (ethylene-co-methacrylic acid) ionomer metal nanocomposite. International Journal of Intelligent Robotics and Applications. 2017;1(2):143-56.

[17] Zheng WJ, An N, Yang JH, Zhou J, Chen YM. Tough Al-alginate/poly (N-isopropylacrylamide) hydrogel with tunable LCST for soft robotics. ACS Applied Materials & Interfaces. 2015;7(3):1758-64.

[18] Martinez RV, Branch JL, Fish CR, Jin L, Shepherd RF, Nunes RM, *et al*. Robotic tentacles with three-dimensional mobility based on flexible elastomers. Advanced Materials. 2013;25(2):205-12.

[19] Hong SY, Lee YH, Park H, Jin SW, Jeong YR, Yun J, *et al*. Stretchable active matrix temperature sensor array of polyaniline nanofibers for electronic skin. Advanced Materials. 2016;28(5):930-5.

[20] Ho DH, Sun Q, Kim SY, Han JT, Kim DH, Cho JH. Stretchable and multimodal all graphene electronic skin. Advanced Materials. 2016;28(13):2601-8.

[21] Choi DY, Kim MH, Oh YS, Jung S-H, Jung JH, Sung HJ, *et al*. Highly stretchable, hysteresis-free ionic liquid-based strain sensor for precise human motion monitoring. ACS Applied Materials & Interfaces. 2017;9(2):1770-80.

[22] Amjadi M, Pichitpajongkit A, Lee S, Ryu S, Park I. Highly stretchable and sensitive strain sensor based on silver nanowire–elastomer nanocomposite. ACS Nano. 2014;8(5):5154-63.

[23] Trung TQ, Ramasundaram S, Lee N-E. Transparent, stretchable, and rapid-response humidity sensor for body-attachable wearable electronics. Nano Research. 2017;10(6):2021-33.

[24] Zhang S, Cai L, Li W, Miao J, Wang T, Yeom J, *et al*. Fully printed silver-nanoparticle-based strain gauges with record high sensitivity. Advanced Electronic Materials. 2017;3(7):1700067.

[25] Luo W, Charara M, Saha MC, Liu Y. Fabrication and characterization of porous CNF/PDMS nanocomposites for sensing applications. Applied Nanoscience. 2019;9(6):1309-17.

[26] Hu N, Karube Y, Yan C, Masuda Z, Fukunaga H. Tunneling effect in a polymer/carbon nanotube nanocomposite strain sensor. Acta Materialia. 2008;56(13):2929-36.

[27] Lipomi DJ, Vosgueritchian M, Tee BC, Hellstrom SL, Lee JA, Fox CH, *et al*. Skin-like pressure and strain sensors based on transparent elastic films of carbon nanotubes. Nature Nanotechnology. 2011;6(12):788.

[28] Kang I, Schulz MJ, Kim JH, Shanov V, Shi D. A carbon nanotube strain sensor for structural health monitoring. Smart Materials and Structures. 2006;15(3):737.

[29] Obitayo W, Liu T. A review: Carbon nanotube-based piezoresistive strain sensors. Journal of Sensors. 2012;2012.

[30] Yamada T, Hayamizu Y, Yamamoto Y, Yomogida Y, Izadi-Najafabadi A, Futaba DN, *et al*. A stretchable carbon nanotube strain sensor for human-motion detection. Nature Nanotechnology. 2011;6(5):296.

[31] Cohen DJ, Mitra D, Peterson K, Maharbiz MM. A highly elastic, capacitive strain gauge based on percolating nanotube networks. Nano Letters. 2012;12(4):1821-5.

[32] Liu Z, Qi D, Guo P, Liu Y, Zhu B, Yang H, *et al*. Thickness-gradient films for high gauge factor stretchable strain sensors. Advanced Materials. 2015;27(40):6230-7.

[33] Abshirini M, Charara M, Marashizadeh P, Saha MC, Altan MC, Liu Y. Functional nanocomposites for 3D printing of stretchable and wearable sensors. Applied Nanoscience. 2019;9(8):2071-83.

[34] Dong D, Ma J, Ma Z, Chen Y, Zhang H, Shao L, *et al*. Flexible and lightweight microcellular RGO@ Pebax composites with synergistic 3D conductive channels and microcracks for piezoresistive sensors. Composites Part A: Applied Science and Manufacturing. 2019;123:222-31.

[35] Yamada T, Hayamizu Y, Yamamoto Y, Yomogida Y, Izadi-Najafabadi A, Futaba DN, *et al*. A stretchable carbon nanotube strain sensor for human-motion detection. Nature Nanotechnology. 2011;6(5):296-301.

[36] Wei Y, Chen S, Yuan X, Wang P, Liu L. Multiscale wrinkled microstructures for piezoresistive fibers. Advanced Functional Materials. 2016;26(28):5078-85.

[37] Ding Y, Xu T, Onyilagha O, Fong H, Zhu Z. Recent advances in flexible and wearable pressure sensors based on piezoresistive 3D monolithic conductive sponges. ACS Applied Materials & Interfaces. 2019;11(7):6685-704.

[38] Lee H, Yoo JK, Park JH, Kim JH, Kang K, Jung YS. A stretchable polymer–carbon nanotube composite electrode for flexible lithium-ion batteries: porosity engineering by controlled phase separation. Advanced Energy Materials. 2012;2(8):976-82.

[39] Wu D, Xu F, Sun B, Fu R, He H, Matyjaszewski K. Design and preparation of porous polymers. Chemical Reviews. 2012;112(7):3959-4015.

[40] Choi S-J, Kwon T-H, Im H, Moon D-I, Baek DJ, Seol M-L, *et al*. A polydimethylsiloxane (PDMS) sponge for the selective absorption of oil from water. ACS Applied Materials & Interfaces. 2011;3(12):4552-6.

[41] Zhao X, Li L, Li B, Zhang J, Wang A. Durable superhydrophobic/superoleophilic PDMS sponges and their applications in selective oil absorption and in plugging oil leakages. Journal of Materials Chemistry A. 2014;2(43):18281-7.

[42] Tebboth M, Jiang Q, Kogelbauer A, Bismarck A. Inflatable elastomeric macroporous polymers synthesized from medium internal phase emulsion templates. ACS Applied Materials & Interfaces. 2015;7(34):19243-50.

[43] Silverstein MS. PolyHIPEs: Recent advances in emulsion-templated porous polymers. Progress in Polymer Science. 2014;39(1):199-234.

[44] Zhang H, Cooper AI. Synthesis and applications of emulsion-templated porous materials. Soft Matter. 2005;1(2):107-13.

[45] Kimmins SD, Cameron NR. Functional porous polymers by emulsion templating: recent advances. Advanced Functional Materials. 2011;21(2):211-25.

[46] Yang X-Y, Chen L-H, Li Y, Rooke JC, Sanchez C, Su B-L. Hierarchically porous materials: synthesis strategies and structure design. Chemical Society Reviews. 2017;46(2):481-558.

[47] Abshirini M, Saha MC, Cummings L, Robison T. Synthesis and characterization of porous polydimethylsiloxane structures with adjustable porosity and pore morphology using emulsion templating technique. Polymer Engineering & Science. 2021;61(7):1943-55.

[48] Xue L, Zhang J, Han Y. Phase separation induced ordered patterns in thin polymer blend films. Progress in Polymer Science. 2012;37(4):564-94.

[49] Zhao J, Luo G, Wu J, Xia H. Preparation of microporous silicone rubber membrane with tunable pore size via solvent evaporation-induced phase separation. ACS Applied Materials & Interfaces. 2013;5(6):2040-6.

[50] Kim J-K, Taki K, Ohshima M. Preparation of a unique microporous structure via two step phase separation in the course of drying a ternary polymer solution. Langmuir. 2007;23(24):12397-405.

[51] Wu S, Zhang J, Ladani RB, Ravindran AR, Mouritz AP, Kinloch AJ, *et al*. Novel electrically conductive porous PDMS/carbon nanofiber composites for deformable strain sensors and conductors. ACS Applied Materials & Interfaces. 2017;9(16):14207-15.

[52] Chun S, Hong A, Choi Y, Ha C, Park W. A tactile sensor using a conductive graphene-sponge composite. Nanoscale. 2016;8(17):9185-92.

[53] Iglio R, Mariani S, Robbiano V, Strambini L, Barillaro G. Flexible polydimethylsiloxane foams decorated with multiwalled carbon nanotubes enable unprecedented detection of ultralow strain and pressure coupled with a large working range. ACS Applied Materials & Interfaces. 2018;10(16):13877-85.

[54] Yang L, Wang R, Song Q, Liu Y, Zhao Q, Shen Y. One-pot preparation of porous piezoresistive sensor with high strain sensitivity via emulsion-templated polymerization. Composites Part A: Applied Science and Manufacturing. 2017;101:195-8.

[55] Jung S, Kim JH, Kim J, Choi S, Lee J, Park I, *et al*. Reverse-micelle-induced porous pressure-sensitive rubber for wearable human–machine interfaces. Advanced Materials. 2014;26(28):4825-30.

[56] Jell G, Verdejo R, Safinia L, Shaffer MS, Stevens MM, Bismarck A. Carbon nanotube-enhanced polyurethane scaffolds fabricated by thermally induced phase separation. Journal of Materials Chemistry. 2008;18(16):1865-72.

[57] Gnanasekaran K, Heijmans T, Van Bennekom S, Woldhuis H, Wijnia S, De With G, *et al*. 3D printing of CNT-and graphene-based conductive polymer nanocomposites by fused deposition modeling. Applied Materials Today. 2017;9:21-8.

[58] Kwok SW, Goh KHH, Tan ZD, Tan STM, Tjiu WW, Soh JY, *et al*. Electrically conductive filament for 3D-printed circuits and sensors. Applied Materials Today. 2017;9:167-75.

[59] Goh GL, Agarwala S, Tan YJ, Yeong WY. A low cost and flexible carbon nanotube pH sensor fabricated using aerosol jet technology for live cell applications. Sensors and Actuators B: Chemical. 2018;260:227-35.

[60] Michelis F, Bodelot L, Bonnassieux Y, Lebental B. Highly reproducible, hysteresis-free, flexible strain sensors by inkjet printing of carbon nanotubes. Carbon. 2015;95:1020-6.

[61] Muth JT, Vogt DM, Truby RL, Mengüç Y, Kolesky DB, Wood RJ, *et al*. Embedded 3D printing of strain sensors within highly stretchable elastomers. Advanced Materials. 2014;26(36):6307-12.

[62] Lewis JA. Direct ink writing of 3D functional materials. Advanced Functional Materials. 2006;16(17):2193-204.

[63] Mannoor MS, Jiang Z, James T, Kong YL, Malatesta KA, Soboyejo WO, *et al*. 3D printed bionic ears. Nano Letters. 2013;13(6):2634-9.

[64] Hinton TJ, Hudson A, Pusch K, Lee A, Feinberg AW. 3D printing PDMS elastomer in a hydrophilic support bath via freeform reversible embedding. ACS Biomaterials Science & Engineering. 2016;2(10):1781-6.

[65] Tang Z, Jia S, Zhou C, Li B. 3D printing of highly sensitive and large-measurement-range flexible pressure sensors with a positive piezoresistive effect. ACS Applied Materials & Interfaces. 2020;12(25):28669-80.

[66] Yu R, Xia T, Wu B, Yuan J, Ma L, Cheng GJ, *et al*. Highly sensitive flexible piezoresistive sensor with 3D conductive network. ACS Applied Materials & Interfaces. 2020;12(31):35291-9.

[67] Barzin J, Sadatnia B. Theoretical phase diagram calculation and membrane morphology evaluation for water/solvent/polyethersulfone systems. Polymer. 2007;48(6):1620-31.

[68] Jansen J, Macchione M, Drioli E. High flux asymmetric gas separation membranes of modified poly (ether ether ketone) prepared by the dry phase inversion technique. Journal of Membrane Science. 2005;255(1-2):167-80.

[69] Barua B, Saha MC. Influence of humidity, temperature, and annealing on microstructure and tensile properties of electrospun polyacrylonitrile nanofibers. Polymer Engineering & Science. 2018;58(6):998-1009.

[70] Fashandi H, Karimi M. Pore formation in polystyrene fiber by superimposing temperature and relative humidity of electrospinning atmosphere. Polymer. 2012;53(25):5832-49.

[71] Cui L, Peng J, Ding Y, Li X, Han Y. Ordered porous polymer films via phase separation in humidity environment. Polymer. 2005;46(14):5334-40.

[72] Flory PJ. Principles of polymer chemistry: Cornell University Press; 1953.

[73] Tompa H. Phase relationships in polymer solutions. Transactions of the Faraday Society. 1949;45:1142-52.

[74] Tompa H. Polymer solutions: Butterworths Scientific Publications; 1956.

[75] Altena FW, Smolders C. Calculation of liquid-liquid phase separation in a ternary system of a polymer in a mixture of a solvent and a nonsolvent. Macromolecules. 1982;15(6):1491-7.

[76] Mark JE. Physical properties of polymers handbook: Springer; 2007.

[77] Zeman L, Tkacik G. Thermodynamic analysis of a membrane-forming system water/N-methyl-2-pyrrolidone/polyethersulfone. Journal of Membrane Science. 1988;36:119-40.

[78] Mulder M. Basic principles of membrane technology: Springer Science & Business Media; 2012.

[79] Tan L, Pan D, Pan N. Thermodynamic study of a water–dimethylformamide–polyacrylonitrile ternary system. Journal of Applied Polymer Science. 2008;110(6):3439-47.

[80] Bates FS. Polymer-polymer phase behavior. Science. 1991;251(4996):898-905.

[81] Dong C-H, He L, Xiao Y-F, Gaddam V, Ozdemir S, Han Z-F, *et al*. Fabrication of high-Q polydimethylsiloxane optical microspheres for thermal sensing. Applied Physics Letters. 2009;94(23):231119.

[82] Yabuta T, Bescher E, Mackenzie J, Tsuru K, Hayakawa S, Osaka A. Synthesis of PDMS-based porous materials for biomedical applications. Journal of Sol-gel Science and Technology. 2003;26(1-3):1219-22.

[83] Thurgood P, Baratchi S, Szydzik C, Mitchell A, Khoshmanesh K. Porous PDMS structures for the storage and release of aqueous solutions into fluidic environments. Lab on a Chip. 2017;17(14):2517-27.

[84] Cui L, Ding Y, Li X, Wang Z, Han Y. Solvent and polymer concentration effects on the surface morphology evolution of immiscible polystyrene/poly (methyl methacrylate) blends. Thin Solid Films. 2006;515(4):2038-48.

[85] Macchione M, Jansen JC, Drioli E. The dry phase inversion technique as a tool to produce highly efficient asymmetric gas separation membranes of modified PEEK. Influence of temperature and air circulation. Desalination. 2006;192(1-3):132-41.

[86] McKelvey SA, Koros WJ. Phase separation, vitrification, and the manifestation of macrovoids in polymeric asymmetric membranes. Journal of Membrane Science. 1996;112(1):29-39.

[87] Hayduk W, Laudie H, Smith OH. Viscosity, freezing point, vapor-liquid equilibriums, and other properties of aqueous-tetrahydrofuran solutions. Journal of Chemical and Engineering Data. 1973;18(4):373-6.

[88] Schneider CA, Rasband WS, Eliceiri KW. NIH Image to ImageJ: 25 years of image analysis. Nature methods. 2012;9(7):671-5.

[89] Standard A. Standard test methods for vulcanized rubber and thermoplastic elastomers—tension. ASTM International: West Conshohocken, PA, USA. 2013;10:1-14.

[90] Bormashenko E, Musin A, Bormashenko Y, Whyman G, Pogreb R, Gendelman O. Formation of films on water droplets floating on a polymer solution surface. Macromolecular Chemistry and Physics. 2007;208(7):702-9.

[91] Golub D, Krajnc P. Emulsion templated hydrophilic polymethacrylates. Morphological features, water and dye absorption. Reactive and Functional Polymers. 2020;149:104515.

[92] Hentze H-P, Antonietti M. Porous polymers and resins for biotechnological and biomedical applications. Reviews in Molecular Biotechnology. 2002;90(1):27-53.

[93] Lalia BS, Kochkodan V, Hashaikeh R, Hilal N. A review on membrane fabrication: Structure, properties and performance relationship. Desalination. 2013;326:77-95.

[94] Sai H, Tan KW, Hur K, Asenath-Smith E, Hovden R, Jiang Y, *et al*. Hierarchical porous polymer scaffolds from block copolymers. Science. 2013;341(6145):530-4.

[95] Matsuyama H, Nishiguchi M, Kitamura Y. Phase separation mechanism during membrane formation by dry-cast process. Journal of Applied Polymer Science. 2000;77(4):776-83.

[96] Kim Y, Yang H, Oh JH. Simple fabrication of highly sensitive capacitive pressure sensors using a porous dielectric layer with cone-shaped patterns. Materials & Design. 2021;197:109203.

[97] Alzoubi M, Tanbour E, Al-Waked R. Compression and hysteresis curves of nonlinear polyurethane foams under different densities, strain rates and different environmental conditions. ASME International Mechanical Engineering Congress and Exposition2011. p. 101-9.

[98] Gibson LJ, Ashby MF. Cellular solids: structure and properties: Cambridge university press; 1999.

[99] Saha M, Mahfuz H, Chakravarty U, Uddin M, Kabir ME, Jeelani S. Effect of density, microstructure, and strain rate on compression behavior of polymeric foams. Materials Science and Engineering: A. 2005;406(1-2):328-36.

[100] Kabir ME, Saha M, Jeelani S. Tensile and fracture behavior of polymer foams. Materials Science and Engineering: A. 2006;429(1-2):225-35.

[101] Abshirini M, Saha MC, Altan MC, Liu Y, Cummings L, Robison T. Investigation of porous polydimethylsiloxane structures with tunable properties induced by the phase separation technique. Journal of Applied Polymer Science. 2021;138(29):50688.

[102] Deng S, Wang Y, Zhuang G, Zhong X, Wei Z, Yao Z, *et al*. Micromechanical simulation of the pore size effect on the structural stability of brittle porous materials with bicontinuous morphology. Physical Chemistry Chemical Physics. 2019;21(24):12895-904.

[103] Chen Y, Das R, Battley M. Effects of cell size and cell wall thickness variations on the stiffness of closed-cell foams. International Journal of Solids and Structures. 2015;52:150-64.

[104] Choi S-W, Zhang Y, Xia Y. Three-dimensional scaffolds for tissue engineering: the importance of uniformity in pore size and structure. Langmuir. 2010;26(24):19001-6.

[105] Abshirini M, Altan MC, Liu Y, Saha MC, Cummings L, Robison T. Manufacturing of porous polydimethylsiloxane (PDMS) plates using solvent evaporation induced phase separation technique. ASME International Mechanical Engineering Congress and Exposition: American Society of Mechanical Engineers; 2020. p. V003T03A23.

[106] Teo N, Jana SC. Open cell aerogel foams via emulsion templating. Langmuir. 2017;33(44):12729-38.

[107] Abshirini M, Saha MC, Altan MC, Liu Y, Cummings L, Robison T. Investigation of porous polydimethylsiloxane structures with tunable properties induced by the phase separation technique. Journal of Applied Polymer Science.50688.

[108] Chen Q, Zhao J, Ren J, Rong L, Cao PF, Advincula RC. 3D printed multifunctional, hyperelastic silicone rubber foam. Advanced Functional Materials. 2019;29(23):1900469.

[109] Huang Q, Zhu Y. Printing conductive nanomaterials for flexible and stretchable electronics: A review of materials, processes, and applications. Advanced Materials Technologies. 2019;4(5):1800546.

[110] Fekiri C, Kim HC, Lee IH. 3D-printable carbon nanotubes-based composite for flexible piezoresistive sensors. Materials. 2020;13(23):5482.

[111] Charara M, Abshirini M, Saha MC, Altan MC, Liu Y. Highly sensitive compression sensors using three-dimensional printed polydimethylsiloxane/carbon nanotube nanocomposites. Journal of Intelligent Material Systems and Structures. 2019;30(8):1216-24.

[112] Woo R, Chen G, Zhao J, Bae J. Structure–mechanical property relationships of 3D-printed porous polydimethylsiloxane. ACS Applied Polymer Materials. 2021;3(7):3496-503.

[113] Abshirini M, Saha MC, Cengiz Altan M, Liu Y. Synthesis and characterization of hierarchical porous structure of polydimethylsiloxane (PDMS) sheets via two-step phase separation method. Materials & Design. 2021;212:110194.

[114] Sengupta D, Pei Y, Kottapalli AGP. Ultralightweight and 3D squeezable graphene-polydimethylsiloxane composite foams as piezoresistive sensors. ACS Applied Materials & Interfaces. 2019;11(38):35201-11.

[115] Zhai W, Xia Q, Zhou K, Yue X, Ren M, Zheng G, *et al*. Multifunctional flexible carbon black/polydimethylsiloxane piezoresistive sensor with ultrahigh linear range, excellent durability and oil/water separation capability. Chemical Engineering Journal. 2019;372:373-82.

[116] Charara M, Luo W, Saha MC, Liu Y. Investigation of lightweight and flexible carbon nanofiber/poly dimethylsiloxane nanocomposite sponge for piezoresistive sensor application. Advanced Engineering Materials. 2019;21(5):1801068.

[117] Song Y, Chen H, Su Z, Chen X, Miao L, Zhang J, *et al*. Highly compressible integrated supercapacitor–piezoresistance-sensor system with CNT–PDMS sponge for health monitoring. Small. 2017;13(39):1702091.

[118] Li C, Thostenson ET, Chou T-W. Dominant role of tunneling resistance in the electrical conductivity of carbon nanotube–based composites. Applied Physics Letters. 2007;91(22):223114.

[119] Duan L, D'hooge DR, Spoerk M, Cornillie P, Cardon L. Facile and low-cost route for sensitive stretchable sensors by controlling kinetic and thermodynamic conductive network regulating strategies. ACS Applied Materials & Interfaces. 2018;10(26):22678-91.

[120] Karipoth P, Pullanchiyodan A, Christou A, Dahiya R. Graphite-based bioinspired piezoresistive soft strain sensors with performance optimized for low strain values. ACS Applied Materials & Interfaces. 2021.

[121] Abshirini M, Saha MC, Altan MC, Liu Y. 3D printed flexible microscaled porous conductive polymer nanocomposites for piezoresistive sensing applications. Advanced Materials Technologies. 2022:2101555.

[122] Abshirini M, Altan MC, Liu Y, Saha MC. Investigation of pore size distribution and mechanical properties of porous polydimethylsiloxane (PDMS) Structures using solvent evaporation technique. ASME International Mechanical Engineering Congress and Exposition: American Society of Mechanical Engineers; 2021. p. V003T03A43.

[123] Rivlin RS. Large elastic deformations of isotropic materials IV. Further developments of the general theory. Philosophical Transactions of the Royal Society of London Series A, Mathematical and Physical Sciences. 1948;241(835):379-97.

[124] Kim B, Lee SB, Lee J, Cho S, Park H, Yeom S, *et al*. A comparison among Neo-Hookean model, Mooney-Rivlin model, and Ogden model for chloroprene rubber. International Journal of Precision Engineering and Manufacturing. 2012;13(5):759-64.

[125] Yang Z, Hayes J, Krishnamurty S, Grosse IR. 3D finite element modeling of pelvic organ prolapse. Computer Methods in Biomechanics and Biomedical Engineering. 2016;19(16):1772-84.